

MEDICAL ELECTRO-THERMAL
IMAGING

A THESIS SUBMITTED TO
THE GRADUATE SCHOOL OF NATURAL AND APPLIED SCIENCES
OF
MIDDLE EAST TECHNICAL UNIVERSITY

BY

HAMZA FEZA CARLAK

IN PARTIAL FULFILLMENT OF THE REQUIREMENTS
FOR
THE DEGREE OF DOCTOR OF PHILOSOPHY
IN
ELECTRICAL AND ELECTRONICS ENGINEERING

FEBRUARY 2012

Approval of the thesis:

**MEDICAL ELECTRO-THERMAL
IMAGING**

submitted by **HAMZA FEZA CARLAK** in partial fulfillment of the requirements for the degree of **Doctor of Philosophy in Electrical and Electronics Engineering Department, Middle East Technical University** by,

Prof. Dr. Canan Özgen
Dean, Graduate School of **Natural and Applied Sciences**

Prof. Dr. İsmet Erkmen
Head of Department, **Electrical and Electronics Eng.**

Prof. Dr. Nevzat G. Gençer
Supervisor, **Electrical and Electronics Eng. Dept., METU**

Examining Committee Members:

Prof. Dr. Osman Eroğul
Biomedical Engineering Dept., GATA

Prof. Dr. Nevzat G. Gençer
Electrical and Electronics Engineering Dept., METU

Prof. Dr. Cengiz Beşikçi
Electrical and Electronics Engineering Dept., METU

Prof. Dr. Tuna Balkan
Mechanical Engineering Dept., METU

Assist. Prof. Dr. Yeşim Doğrusöz Serinağaoğlu
Electrical and Electronics Engineering Dept., METU

Date:

_____ 10.02.2012

I hereby declare that all information in this document has been obtained and presented in accordance with academic rules and ethical conduct. I also declare that, as required by these rules and conduct, I have fully cited and referenced all material and results that are not original to this work.

Name, Last name: Hamza Feza Carlak

Signature :

ABSTRACT

MEDICAL ELECTRO-THERMAL IMAGING

Carlak, Hamza Feza
Ph. D., Department of Electrical and Electronics Engineering
Supervisor: Prof. Dr. Nevzat G. Gençer

February 2012, 144 pages

Breast cancer is the most crucial cancer type among all other cancer types. There are many imaging techniques used to screen breast carcinoma. These are mammography, ultrasound, computed tomography, magnetic resonance imaging, infrared imaging, positron emission tomography and electrical impedance tomography. However, there is no gold standard in breast carcinoma diagnosis. The object of this study is to create a hybrid system that uses thermal and electrical imaging methods together for breast cancer diagnosis. Body tissues have different electrical conductivity values depending on their state of health and types. Consequently, one can get information about the anatomy of the human body and tissue's health by imaging tissue conductivity distribution. Due to metabolic heat generation values and thermal characteristics that differ from tissue to tissue, thermal imaging has started to play an important role in medical diagnosis. To increase the temperature contrast in thermal images, the characteristics of the two imaging modalities can be combined. This is achieved by implementing thermal imaging applying electrical currents from the body surface within safety limits (i.e., thermal imaging in active mode). Electrical conductivity of tissues changes with frequency, so it is possible to obtain more than one thermal

image for the same body. Combining these images, more detailed information about the tumor tissue can be acquired. This may increase the accuracy in diagnosis while tumor can be detected at deeper locations. Feasibility of the proposed technique is investigated with analytical and numerical simulations and experimental studies. 2-D and 3-D numerical models of the female breast are developed and feasibility work is implemented in the frequency range of 10 kHz and 800 MHz. Temporal and spatial temperature distributions are obtained at desired depths. Thermal body-phantoms are developed to simulate the healthy breast and tumor tissues in experimental studies. Thermograms of these phantoms are obtained using two different infrared cameras (microbolometer uncooled and cooled Quantum Well Infrared Photodetectors). Single and dual tumor tissues are determined using the ratio of uniform (healthy) and inhomogeneous (tumor) images. Single tumor (1 cm away from boundary) causes 55 °mC temperature increase and dual tumor (2 cm away from boundary) leads to 50 °mC temperature contrast. With multi-frequency current application (in the range of 10 kHz-800 MHz), the temperature contrast generated by 3.4 mm³ tumor at 9 mm depth can be detected with the state-of-the-art thermal imagers.

Keywords: Medical imaging, thermal infrared imaging, electrical impedance tomography, breast cancer detection

ÖZ

TIBBİ ELEKTRO-TERMAL GÖRÜNTÜLEME

Carlak, Hamza Feza
Doktora, Elektrik ve Elektronik Mühendisliği Bölümü
Tez Yöneticisi: Prof. Dr. Nevzat G. Gençer

Şubat 2012, 144 sayfa

Meme kanseri, bütün kanser türleri arasında en önemli kanser türüdür. Meme kanseri taramasında kullanılan çok sayıda görüntüleme tekniği bulunmaktadır. Bunlar; mamografi, yansılınım, bilgisayarlı tomografi, manyetik rezonans görüntüleme, kızılötesi görüntüleme, pozitron emisyon tomografisi ve elektriksel iletkenlik görüntülemesidir. Ancak, meme kanseri tanısında herhangi bir altın standart bulunmamaktadır. Bu çalışmanın amacı göğüs kanseri teşhisinde kızılötesi ve elektriksel iletkenlik görüntüleme yöntemlerini bir arada kullanarak performansı daha yüksek melez (hibrit) bir sistemin oluşturulmasıdır. Vücut dokuları sağlık durumlarına ve türlerine bağlı olarak farklı elektriksel iletkenlik değerlerine sahiptirler. Bu nedenle, doku iletkenlik dağılımının görüntülenmesi ile vücudun anatomik yapısı ve dokuların sağlık durumları ile ilgili bilgi sağlanabilir. Metabolik ısı artış değerinin ve termal özelliğin farklı dokularda değişkenlik göstermeleri nedeniyle, termal kızılötesi görüntüleme meme kanseri teşhisinde önemli bir rol oynamaya başlamıştır. Termal görüntülerdeki sıcaklık farklarını (kontrastları) artırmak için iki görüntüleme yönteminin özellikleri birleştirilebilir. Bu da, termal görüntülemeyi vücut yüzeyinden güvenlik sınırlarında elektrik akımları uygulayarak gerçekleştirmek suretiyle mümkün olabilir (etken modda termal görüntüleme).

Dokuların elektriksel iletkenlikleri frekansla deęişmektedir, dolayısıyla aynı cisim için birden fazla termal görüntü almak mümkündür. Bu görüntüleri bir araya getirerek, tümör dokusu hakkında daha detaylı bilgi elde edinilebilir. Bu, tanı doğruluęunu artırırken, tümör dokusu da daha derinlerde görüntülenebilecektir. Önerilen teknięin fizibilitesi; analitik ve sayısal benzetim ve deneysel yöntemler kullanılarak incelenmiştir. Göęüs dokusunun 2 ve 3 boyutlu sayısal modeli geliřtirmiş ve yapılabirlik çalıřmaları 10 kHz ile 800 MHz frekans aralıęında gerçekleştirilmiştir. Zamansal ve uzaysal sıcaklık daęılımı görüntüleri istenilen derinliklerde elde edilmiştir. Deneysel çalıřmalarda, saęlıklı ve tümör dokularını modellemek için termal (ısı) doku fantomları geliřtirilmiştir. Fantomların sıcaklık daęılımı görüntüleri iki farklı kızılötesi kamera kullanılarak elde edilmiştir (soęutmasız Mikrobolometre ve soęutmalı Kuantum Kuyulu Kızılötesi Fotodetektör). Tek ve çift tümör dokuları, homojen (saęlıklı) ve homojen olmayan (tümörlü) dokuların oran görüntüsü kullanılarak tespit edilmiştir. Tek tümör (kenardan 1 cm uzaklıkta) 55 °mC ve çift tümör (kenardan 2 cm uzaklıkta) 50 °mC sıcaklık farkı meydana getirmiştir. Çoklu frekanslı akım uygulayarak (10 kHz–800 MHz aralıęında), günümüz teknolojisi kızıl ötesi termal kameraları ile 9 mm derinlikteki 3.4 mm³'lük tümörün yarattıęı sıcaklık farkını tespit edebilmek mümkündür.

Anahtar kelimeler: Tıbbi görüntüleme, Termal kızılötesi görüntüleme, Elektriksel iletkenlik tomografisi, Meme kanseri tanısı

To My Family

ACKNOWLEDGEMENTS

This study was arisen under the supervision of Prof. Dr. Nevzat G. Gençer. I would like to express my deepest gratitude for his endless guidance, criticism and support throughout this study. It has been great privilege and experience working with Prof. Dr. N. Gençer.

I would also express my sincere appreciation to my Ph.D. thesis monitoring members who are Prof. Dr. Tuna Balkan and Prof. Dr. Cengiz Beşikçi for their valuable and great guidance throughout the study. Prof. Dr. Cengiz Beşikçi let me use his research laboratory and infrared camera and his assistant Yetkin Arslan helped me in the use of infrared camera and spent his valuable time. I would like to thank both of them for their valuable helps. I would like to thank Prof. Dr. Osman Eroğul, Prof. Dr. Murat Eyüpoğlu, Assist. Prof. Dr. Yeşim Serinağaoğlu, Prof. Dr. Arif Ertaş, Prof. Dr. Mirzahan Hızal and Prof. Dr. Ahmet Rumeli for their valuable supports and helps. I would also like to express my admiration to Assoc. Prof. Dr. Şükrü Özen from Akdeniz University for his precious supports and encouragements.

Prof. Dr. Murat Özgören gave me an opportunity to use their infrared camera and laboratory at at 9 Eylül University, Medical Faculty, Biophysics Department, İzmir. I would like to express my thankfulness to him and his colleagues Dr. Onur Bayazıt, Mustafa Şakar and Uğraş Erdoğan.

I would also like to thank all of the Biomedical Research Group members, Koray Özkan, Reyhan Zengin, Evren Değirmenci, Berna Akıncı, Tankut Topal, Evrim Çolak, Ceren Bora, Soner Keçeli, Ersin Karcı, Ali Reza Mazloumi, Kerim Kara, Ümit

Aydın, Ali Ersöz, Azadeh Kamali Tafreshi especially Volkan Emre Arpınar, Galip Özdemir, Balkar Erdoğan and Şebnem Demirci for their friendship, assistance and valuable supports. I also acknowledge to my dear cousin Murat Aşçı and his wife Sema Aşçı for their precious helps in drawings.

Finally, I would like to express my special appreciations and gratitude to my family for their great support that was always with me. I am definitely sure that I am not able to complete this study without their endless support.

The author was financially supported by the State Planning Organization (DPT) Grant No: BAP-08-11-DPT.2002K120510-BIL-7 project.

TABLE OF CONTENTS

ABSTRACT	iv
ÖZ	vi
ACKNOWLEDGEMENTS.....	ix
TABLE OF CONTENTS	xi
LIST OF TABLES	xv
LIST OF FIGURES.....	xvii
CHAPTERS	
1. INTRODUCTION.....	1
1.1 Electrical Conductivity Imaging.....	3
1.1.1 Development of the Electrical Impedance Technique in Breast Cancer Diagnosis	7
1.2 Infrared Thermal Imaging	13
1.2.1 Theory of Thermal Imaging.....	13
1.2.2 Thermographic Measurement	17

1.2.3 Development of the Medical Infrared Imaging and Infrared Breast Imaging.....	19
1.2.3.1 Thermal Imaging of Breast	22
1.3 Motivation of the Thesis Study.....	28
1.4 Objectives of the Study.....	32
1.5 Outline of the Study.....	33
2. ELECTRO-THERMAL IMAGING.....	34
2.1 Introduction.....	34
2.2 Theory.....	36
2.3 Analytical Feasibility Studies.....	40
2.3.1 Evaluating the Time Constants of Different Tissues.....	40
2.3.2 Temperature Rise due to an Applied Electrical Current: Transient Behaviour.....	43
2.3.3 Total Rate of Heat Transfer from the Breast Surface due to Convection and Radiation.....	44
2.4 Summary and Discussions.....	45
3. SIMULATION STUDY.....	46
3.1 Introduction.....	46
3.2 Modeling.....	46

3.3 Numerical Analysis	49
3.4 Results	50
3.4.1 Tumor at Different Locations.....	50
3.4.2 Responses at Different Operation Frequencies.....	54
3.4.3 Transient Response.....	56
3.4.4 Temperature Increase due to Malignant Tissue at Different Depths: 3D Studies	58
3.4.5 Tumor Temperature Changes for Different Current Density Values..	62
3.4.6 Temperature Increases for Different Dimensions of Tumor.....	62
3.4.7 Temperature changes on the breast surface due to different operation frequencies.....	64
3.4.8 Temperature Increases of Poly Cancerous Tissues on the Breast Surface.....	68
3.4 Summary and Discussions.....	71
4. EXPERIMENTAL STUDY.....	76
4.1 Current Generator	76
4.1.1 Operation of the Current Driver Circuit.....	78
4.1.2 Frequency Characteristics of the Output Resistance.....	80
4.2 Experimental Setup.....	83

4.2.1 Model Preparation	87
4.2.2 Experimental Process.....	90
4.2.3 Calibration of the Infrared Camera	91
4.3 Experimental Results.....	92
4.3.1 Homogeneous Phantom in Active Mode of Operation.....	93
4.3.2 Inhomogeneous Phantom in Active Mode of Operation.....	94
4.3.3 Inhomogeneous Phantom in Active Mode (DC).....	96
4.3.4 Dual Malignant Tissues in Active Mode (DC).....	98
4.4 Summary and Discussions.....	101
5. CONCLUSIONS.....	105
REFERENCES.....	110
APPENDIX	
A. THEORY OF ELECTROMAGNETIC AND HEAT PROBLEMS.....	129
VITA.....	142

LIST OF TABLES

TABLES

Table 1.1	Electrical conductivities of different breast tissues at different frequencies [33].....	4
Table 1.2	In vitro impedance measurement studies of woman breast tissue.....	9
Table 2.1	Healthy and Cancerous Tissue Characteristics and Calculated Time Constant Values [22], [23], [24], [25].....	42
Table 2.2	Model parameters employed for the calculation of the convection and radiation heat transfer using the realistic breast model [141].....	45
Table 3.1	Healthy and Malignant Tissue Electrical and Thermal Characteristics. Table is reproduced from [22], [23], [24], [30].....	48
Table 3.2	Tumor Temperatures for different tumor locations and performance improvements due to active mode of operation.....	61
Table 3.3	Top surface temperatures for different tumor depths and contrast differences due to active mode of operation.....	61
Table 4.1	Output Resistance Values at Different Frequencies.....	82
Table 4.2	Characteristics of the Infrared Camera used in Experiments.....	85

Table 4.3 Phantom Ingredients and Corresponding Conductivity Values.....89

LIST OF FIGURES

FIGURES

- Figure 1.1 Electromagnetic Spectrum (Region 1 belongs to X-ray band, 2 is ultra violet band, 3 is visible light band, 4 is infrared region (region a shows near infrared, b shows middle infrared, c shows far infrared and d is extreme infrared region), 5 is microwave (radar) band and 6 is radio frequency band)..... 14
- Figure 1.2 Subsections of Infrared Region.....14
- Figure 1.3 Schematic of a Thermographic Measurement, 3 different radiations contribute the measurements of a thermal camera. Direct radiation from the object, radiations reflected from surroundings and radiations from the atmosphere.....17
- Figure 1.4 Schematic of an Electro-Thermal Imaging System. Current is applied to the female breast with a pair of electrodes inserted on two fingers. Since fingers are mobile, current can be injected into the desired location. Thermograms of the breast are obtained with an infrared camera.....31
- Figure 2.1 Block diagram of Electro-Thermal Imaging System. Current is applied from the surface of the breast with a voltage controlled current source and necessary instrumentation, and temperature distribution of the breast is imaged using an infrared camera..... 35

Figure 2.2 Schematic of the Electromagnetic Problem. A and B are entry and exit points of the current. \vec{E} is the electric field, ϕ is the scalar potential, σ is the electrical conductivity, ϵ is the permittivity and μ is the permeability..... 36

Figure 2.3 Schematic of the Bio-Heat problem when electrical currents are included as heat sources. C is the is specific heat, ρ is mass density, k is thermal conductivity, ρ_b is blood mass density, C_b is the blood specific heat rate, W_b is the blood perfusion rate, Q_{met} is the metabolic heat generation, Q_{ext} is the heat source due to current application and T is the absolute temperature.....39

Figure 3.1 Two – dimensional simulation geometry. Larger square represents the healthy and smaller square represents the cancerous tissue. 5 mA/cm^2 current at 10 kHz is applied with current electrodes..... 47

Figure 3.2 Three-dimensional simulation geometries. The inhomogeneity represents a cubic (dxdxd) tumor inside the breast. (a) Current electrodes are at the center of the side surfaces. (b) Current electrodes are shifted 2.4 cm (center of the electrode is located 2.6 cm away from the top surface) to the upper surface (camera site).....48

Figure 3.3 Flowchart of the Electro–Thermal Imaging System. Electrical currents results in resistive heating. In-plane electric currents module calculates the resistive heating and Bio-Heat Equation module calculates the temperature distribution in the body..... 49

Figure 3.4 Temperature distribution for the centric tumor case in passive mode. $T_{max} = 37.537 \text{ }^\circ\text{C}$, $T_b = 37.096 \text{ }^\circ\text{C}$ and $\Delta T = 441 \text{ }^\circ\text{mC}$ 52

Figure 3.5 Temperature distribution for the centric tumor case in active mode.
 $T_{\max} = 37.716\text{ }^{\circ}\text{C}$, $T_b = 37.158\text{ }^{\circ}\text{C}$ and $\Delta T = 558\text{ }^{\circ}\text{mC}$ 53

Figure 3.6 Temperature distribution for the eccentric tumor case in passive mode.
 $T_{\max} = 37.537\text{ }^{\circ}\text{C}$, $T_b = 37.085\text{ }^{\circ}\text{C}$ and $\Delta T = 452\text{ }^{\circ}\text{mC}$ 53

Figure 3.7 Temperature distribution for the eccentric tumor case in active mode.
 $T_{\max} = 38.144\text{ }^{\circ}\text{C}$, $T_b = 37.308\text{ }^{\circ}\text{C}$ and $\Delta T = 836\text{ }^{\circ}\text{mC}$ 54

Figure 3.8 Difference of the two active mode images at 10 kHz, $\Delta T_{\max} = 520^{\circ}\text{mC}$
.....55

Figure 3.9 Difference of the two active mode images at 80 MHz, $\Delta T_{\max} = 550^{\circ}\text{mC}$
.....55

Figure 3.10 Transient analysis. 2D model (Fig. 3.1) is used in active mode ($i = 5\text{mA}$ at 10 kHz). Transient response of the temperature at the malignant tissue is shown.....57

Figure 3.11 Transient analysis. 2D model is used in active mode ($i = 5\text{mA}$ at 10 kHz). The malignant tissue is located 1 cm from the left electrode. Transient response of the temperature at the malignant tissue is shown.....57

Figure 3.12 Transient analysis. 3D model (Fig. 3.2(a)) is used in active mode ($5\text{mA}/\text{cm}^2$ at 10 kHz). Transient response of the temperature at the malignant tissue is shown.....58

Figure 3.13 Tumor temperature versus tumor depth in active mode (5 mA/cm^2 at 10 kHz). 3D Model (Fig 3.2(b)).....60

Figure 3.14 The temperature contrast on the top surface of the breast model for different tumor locations (5mA/cm^2 at 10 kHz). 3D Model (Fig 3.2 (b)).....60

Figure 3.15 Tumor temperature versus current density plot.....62

Figure 3.16 Tumor temperature versus tumor volume. 3D Model (Fig. 3.2(a))....63

Figure 3.17 Performance increase versus tumor dimension. Current injection improves the contrast between the healthy and the cancerous tissue. 3D Model (Fig. 3.2(a)).....63

Figure 3.18 Temperature distribution on the top surface of the breast model in passive mode. The malignant tissue (42 mm^3) is at 1.5 cm depth from the surface. Color bar indicates the temperature difference ($^{\circ}\text{C}$).....65

Figure 3.19 Temperature distribution on the top surface of the breast model in active mode (5 mA/cm^2 at 10 kHz). The malignant tissue (42 mm^3) is at 1.5 cm depth from the surface. Color bar indicates the temperature difference ($^{\circ}\text{C}$).....65

Figure 3.20 Temperature distribution on the top surface of the breast model in active mode (5 mA/cm^2 at 100 kHz). The malignant tissue (42 mm^3) is at 1.5 cm depth from the surface. Color bar indicates the temperature difference ($^{\circ}\text{C}$).....66

Figure 3.21 Temperature distribution on the top surface of the breast model in active mode (5 mA/cm^2 at 10 MHz). The malignant tissue (42 mm^3) is at 1.5 cm depth from the surface. Color bar indicates the temperature difference ($^{\circ}\text{C}$).....66

Figure 3.22 Temperature distribution on the top surface of the breast model in active mode (5 mA/cm² at 800 MHz). The malignant tissue (42 mm³) is at 1.5 cm depth from the surface. Color bar indicates the temperature difference (°C).....67

Figure 3.23 Temperature distribution on the top surface of the breast model in active mode (5 mA/cm² at 800 MHz). (1.5 x 1.5 x 1.5 mm = 3.4 mm³) tumor is detected from 9 mm depth). Color bar indicates the temperature difference (°C).....67

Figure 3.24 Difference image of the Tumor Tissues (3.4 mm³) and healthy breast tissue on the breast surface in passive mode (Temperature increases occur just due to the metabolic heat generation and blood perfusion of the tissue). Color bar indicates the temperature difference (°C).....69

Figure 3.25 Difference image on the top surface of the breast model in active mode (5 mA/cm² at 100 kHz). Dual 3.4 mm³ tumors are detected from 9 mm depth. Color bar indicates the temperature difference (°C).....70

Figure 3.26 Difference image on the top surface of the breast model in active mode (5 mA/cm² at 800 MHz). Dual 3.4 mm³ tumors are detected from 9 mm depth. Color bar indicates the temperature difference (°C).....70

Figure 3.27 Difference image on the Tumor Tissues and healthy breast tissue on the breast surface when there is a 5 mA current stimulation at 800 MHz (4 identical tumors which have 3.4 mm³ dimensions are detected from 9 mm depth. Color bar indicates the temperature difference (°C).....71

Figure 4.1 Voltage to Current Converter (V/I) Circuit. AB Class amplifier stage is used to amplify current and remove crossover distortion. R= 10 kΩ, R1= 680 Ω, R2= 10 Ω, Rpot1= 2 kΩ, Rpot2= 500 Ω.....79

Figure 4.2	Circuit for calculating the output resistance of the VCCS. High value resistors (Rins) are connected in parallel to the output of the circuit and voltage (Vout) values are recorded for each frequency.....	81
Figure 4.3	Experimental setup established at 9 Eylül University, Faculty of Medicine, Biophysics Department, İzmir	84
Figure 4.4	Experimental setup at METU, Electric-Electronic Department, Quantum Devices & Nanophotonics Research Lab.....	85
Figure 4.5	Block diagram of Quantum Well Infrared Photon (QWIP) Detector Infrared Camera developed at METU, Electric-Electronics Department, Quantum Devices & Nanophotonics Research Lab.....	86
Figure 4.6	Phantom geometry. Electrodes are inserted to the right and left side boundaries. Background phantom simulates the healthy breast tissue and inner tissue (its location can be moved) mimics the tumor tissue.....	87
Figure 4.7	Agar phantom sample picture. Copper electrodes are inserted to the boundary of the model and tumor tissue is located 1 cm away from the left side boundary.....	89
Figure 4.8	Thermal-body phantoms used in experiments performed at Quantum Devices & Nanophotonics Research Lab. (Homogeneous and inhomogeneous phantoms including single or poly tumor tissues)	90
Figure 4.9	Homogeneous agar phantom. Current is applied with copper electrodes located at right and left side of the phantom.....	93

Figure 4.10 Difference of images (taken in active and passive mode) (Using micro bolometer uncooled thermal infrared camera (spatial resolution is 320 x 240 pixels) at 9 Eylül University, Faculty of Medicine, Biophysics Department, İzmir). Color bar indicates the temperature difference (°mC).....94

Figure 4.11 Agar phantom including an inhomogeneity representing the tumor tissue. Electrodes are attached at the boundary of the phantom.....95

Figure 4.12 Differences of healthy and tumor tissue images (Using micro bolometer uncooled thermal infrared camera (spatial resolution is 320 x 240 pixels) at 9 Eylül University, Faculty of Medicine, Biophysics Department, İzmir), Color bar indicates the temperature difference (°C).....95

Figure 4.13 Ratio of healthy and tumor tissue images (Using microbolometer uncooled thermal infrared camera (spatial resolution is 320 x 240 pixels) at 9 Eylül University, Faculty of Medicine, Biophysics Department, İzmir), Color bar indicates the temperature difference (°C).....96

Figure 4.14 Thermal image of the phantom in passive mode (Using QWIP cooled thermal infrared camera at METU, Electric-Electronics Department, Quantum Devices & Nanophotonics Research Lab.).....97

Figure 4.15 Thermal image of the phantom in active mode (10 mA current (DC) stimulation for 600 sec), (Using QWIP cooled thermal infrared camera at METU, Electric-Electronics Department, Quantum Devices & Nanophotonics Research Lab).....97

Figure 4.16 Ratio of thermal images (taken in active and passive mode) (Using QWIP cooled thermal infrared camera at METU, Electric-Electronics Department, Quantum Devices & Nanophotonics Research Lab.).....98

Figure 4.17 (a) Agar phantom including the dual tumor tissue, (b) Ratio of thermal images (taken in active and passive mode) (Using QWIP cooled thermal infrared camera at METU, Electric-Electronics Department, Quantum Devices & Nanophotonics Research Lab).....99

Figure 4.18 Ratio of healthy and tumor tissue images in active mode of operation (Using QWIP cooled thermal infrared camera at METU, Electric-Electronics Department, Quantum Devices & Nanophotonics Research Lab)..... 100

CHAPTER 1

INTRODUCTION

Breast cancer is the most common cancer type among women [16], [95]. Imaging techniques used in the determination of the masses in the breast are mammography, ultrasound, computed tomography, magnetic resonance imaging, positron emission tomography and electrical impedance tomography. However, there is no gold standard in breast cancer diagnosis. Consequently, complementary imaging modalities are used.

Mammography is the standard test for breast screening, however, it has accuracy problems especially for smaller tumours and it is not comfortable for patients. It is more accurate to find cancerous tissue in a dense breast. If the dimension of a tumour is lower than 1.6 cm, it cannot be reliably sensed (since X-rays that pass through the tumour is less affected). Statistical studies show that there is 10-25 % false negative (tumor is undiagnosed following a mammogram) ratio in mammography [34]. When the patients are imaged by mammography, they are exposed to an ionizing radiation which may be harmful for the human tissue.

Ultrasound is also one of the most important imaging modalities used to evaluate breast. However, it cannot show micro calcifications and cannot monitor deep areas of a breast [16]. Magnetic resonance imaging (MRI) is another imaging modality used in breast imaging. However, it is not recommended as a screening tool by itself; it is used as a complementary tool. Although it is more sensitive than mammograms,

it has a higher false-positive rate which results in unnecessary biopsies. Since it requires a longer time for data acquisition it is not preferred by the patients.

Electrical impedance tomography and thermal infrared imaging are also used in breast cancer diagnosis. However, they are not individually sufficient to diagnose cancerous tissue in early stages. It is not easy to separate malign tissue from benign tissue with electrical impedance tomography; it needs further improvements [30]. The accuracy of tumor detection should be improved in infrared imaging, especially when the tumor is located at deeper locations and at early stages [31]. Due to these reasons, none of these imaging modalities is adopted as a gold standard in detecting a cancerous tissue in the breast. They have been used as an adjunct to conventional medical imaging techniques.

The motivation of the thesis work is to develop a hybrid imaging modality that improves the detection performance of cancerous tissue. In this *bimodal* system, thermal imaging is implemented in *active mode*, i.e., thermal images are displayed while electrical currents are applied. This approach is a better complement to standard techniques as it takes the advantages of both thermal and electrical impedance imaging techniques. It also has a potential to be used as a sole imaging modality for accurate, faster, comfortable and cheaper screening technique in breast cancer detection.

In the rest of this chapter, both imaging modalities electrical impedance imaging and thermal infrared imaging will be introduced.

1.1 Electrical Conductivity Imaging

Information about the anatomy of the human body and tissue's health can be obtained by imaging the tissue electrical conductivity distribution. Since tissues have different electrical properties (Table 1.1.), these images can be used to identify organs and evaluate the function in the thorax, the head, and other sites [2].

Imaging electrical conductivity of tissues has been a popular research area [1]. Different methodologies have been proposed to image the spatio-temporal evolution of conductivity changes in the human body [3, 4]. However, in most of these techniques, electrodes are the inevitable means to obtain data from the body conductivity. They are used either to introduce energy by current injection or to measure voltages from the body surface, or for both purposes. In applied-current electrical impedance tomography (ACEIT), current injection and voltage measurements are both performed by the surface electrodes [5, 6, 7, and 8]. Electrical current is injected to the object with a pair of electrodes, and the resultant boundary voltages are measured for each current drive. After applying all possible current drives a voltage data set is generated, and the conductivity distribution is reconstructed using an image reconstruction algorithm. In induced-current electrical impedance tomography (ICEIT), currents are introduced by magnetic induction and voltages are measured using the surface electrodes [9, 10, 11, and 12].

Electrical conductivity and permittivity of tissues change with frequency [32]. Consequently, different images can be reconstructed for each operation frequency yielding more than one image for the same body.

Table 1.1

Electrical conductivities of different breast tissues at different frequencies [33]

Breast Tissue Conductivity (ms/cm)	10 kHz	100 kHz	10 MHz
Tumor (center)	3.98	4.28	7.24
Tumor (surrounding tissue)	1.62	1.70	2.70
Fatty with tumor cells	0.65	0.67	1.08
Tissue far from tumor center	0.28	0.31	0.37
Healthy breast tissue	0.22	0.22	0.25

The beginning of electrical conductivity imaging withstands in the last quarter of 1800s by Stewart's studies on vascular system [35]. However, the first application of ACEIT was implemented in geological studies which were approximately 70 years ago [36]. Clinical applications have been started in 1983 to measure regional changes in lung volumes for monitoring respiratory functions. Barber and Brown from Sheffield University group invented a method to obtain images of electrical resistivity [37, 38]. Human forearm image is reconstructed using a simple backprojection algorithm.

Lionel Tarasenko had studied the sensitivity of surface measurements to internal changes using a finite element mesh [39]. T. Murai and Y. Kavaga implemented a simulation study using the finite element method [45]. This study used the sensitivity matrix approach to reconstruct the conductivity distribution. Sensitivity matrix gives the relationship between the changes in voltage measurements and conductivity perturbation. Studies on the application of sensitivity matrix approach in ICEIT were presented by N. Gençer, Z. İder and M. Kuzuoğlu [46], [47]. K. Paulson, W Lionheart and M Pidcock created the Pompus algorithm which can rapidly calculate

conductivity distributions close to the required image. Therefore, computational time dramatically decreases compared to other standard Newton based reconstruction algorithms [43]. This development renders the 3-D EIT systems feasible.

Due to limitations in designing high-accuracy current sources at high frequencies, use of voltage sources were desired to inject current. To be able to apply current in desired magnitude, the transfer admittance matrix is measured and then voltage level is adjusted to produce appropriate amount of current. Next critical development was adopting digital signal demodulation [48]. As long as high speed analogue-to-digital converters were produced, studies were concentrated on digital signals.

First EIT applications were implemented using single frequency alternating current sources. Many groups used the single-frequency EIT devices in animal experiments (Hahn et al [124], Newell et al [125], Adler et al [126], Frerichs [127], [128]), patients (Campbell [129], Frerichs et al [130] and Kunst et al [131]), and healthy body (Harris et al [132], Holder and Temple [133], Leathard et al [134], Eyüboğlu et al [135], Frerichs et al [136], Hahn et al [137] and Kunst et al [138], [131]). Then, multi-frequency systems were also introduced operating between kHz and 1 MHz [55]. Since tissues have different electrical impedance values at different frequencies, multiple frequencies lead to obtain different conductivity images for the same body.

There are two techniques in multi-frequency EIT imaging. In the first technique, image is obtained by taking the difference of local impedance measurements taken at different frequencies. M. Osypka had obtained such images which were called as quasi-static images [54]. In the second model, biological tissue was modeled as the extracellular fluid, the intracellular fluid and the cell membrane with R, C, S (R resistor is parallel with series resistor S and a capacitor C) elements and conductivity data was obtained directly from multi-frequency measurements. This model and study was developed from Cole and Cole [56].

S. Paulson, K. Pidcock, N. Mcleod have experienced to obtain impedance data with impedance spectroscopy technique from live human tissue by using a small probe [51], [52].

Parametric images of lungs had been studied by different groups in adult patients [57], infants [55], and in normal subjects [58]. Although some preliminary works and feasibility studies of multi-frequency EIT imaging are presented, it is still in progress stage for the physiological interpretation from the multi-frequency measurements.

A 3D Electrical Impedance Imaging system was improved by Oxford Brookes University EIT group [50]. The system was produced for static imaging and capable of producing 3D images.

E. J. Woo, S. Lee and C. W. Mun proposed an approach that uses a Magnetic Resonance Imaging (MRI) system while injecting current to the body. In this approach, internal current density value can be measured using MRI, and hence high resolution images of the conductivity distributions can be reconstructed [53].

In an alternative measurement technique, electrical current is induced inside the body using a time-varying (usually sinusoidal) magnetic field. Induced currents generate a secondary magnetic field which is measured by a receiver coil and associated electronics. This approach has been used for decades for different purposes, however, it was firstly used by McFee and Tarjan [59] for medical applications to measure average head conductivity and to follow conductivity changes of the thorax. Gençer and Tek proposed a new medical imaging modality based on the same measurement technique using miniaturized coils [139]. The authors reconstructed the conductivity of biological tissues using magnetic excitation by inducing electrical currents inside the body. In that study, numerical models were generated by analyzing mathematical aspects of the methodology. They also implemented an impressive study on forward

problem solution for electrical conductivity imaging [1]. Time-varying magnetic fields were used to induce currents inside the body, and measurements were obtained via contactless measurements. Scalar potential distribution was figured out using the finite element method. In-vivo experimental study was implemented by K. Özkan and N. Gençer [63]. Electrical conductivity imaging of live animal (leech) was achieved successfully via contactless measurements.

Korzhenin and Cherepenin had also developed an important theoretical study [60]. Two coils were used to measure the phase angle to define the eddy currents in the body. Filtered backprojection algorithm was applied to reconstruct the conductivity images. The development of magnetic impedance tomography was surveyed in Griffith's study [61].

Medical applications of EIT have been performed by almost 20 groups and they have been mainly concentrated on pulmonary ventilation, perfusion, hyperthermia and gastric function topics [78].

1.1.1 Development of the Electrical Impedance Technique in Breast Cancer Diagnosis

One of every 8 women has got breast cancer during her life time in the USA. Consequently, development of safer, accurate, faster, cheaper and comfortable methods for breast imaging is invaluable. Efforts to develop electrical impedance imaging methods are based on the fact that electrical conductivity value changes depending on the state of health of the tissue. Cancerous tissue has higher conductivity compared to the healthy tissue [65]. Thus conductivity differences can be used as a good indicator to diagnose the malignant tissue.

Many in vitro impedance measurement studies have been proposed since 1920's. Remarkable difference of capacitance between cancerous tissue and healthy tissue was determined by Frick and Morse in the 1920's [66]. However, recent researches are concentrated on electrical impedance measurements instead of capacitance differences. More details can be obtained with conductivity measurements. These studies have shown that, the electrical property of the tissue depends on its state of health. Malignant tissue has lower impedivity [67, 68] and higher permeability (higher conductivity) [66, 69, 70, 71] compared to the normal tissue. Electrical properties of cancerous tissue and healthy tissue differ due to salt and cellular water amount, changes of the membrane permeability and orientation of cells [72].

Frequency range is also an important factor that affects the electrical conductivity and permittivity of the tissue. Different electrical conductivity distributions and measurements can be obtained for the same body by applying electrical currents at different frequency values. There were many in vitro impedance measurement studies of woman breast tissue implemented at various frequencies.

Studies (Table 1.2) have shown that, in the breast cancer diagnosis, the optimal frequency range for electrical impedance measurement is in between 100 Hz to 100 MHz. This interval corresponds to α and β regions [71].

Table 1.2

In vitro impedance measurement studies of woman breast tissue

Frequency Ranges	Results
500 Hz – 1 MHz	Cancerous tissues have lower impedances (400 Ω cm at 1 kHz) compared to fatty tissue (2000 Ω cm at 1 kHz). Moving from the center of the tumor, the impedance value increases [67].
1 kHz – 10 MHz	The admittivity is the highest for cancerous tissue and the lowest for the healthy tissue. Complex conductivity value of the transitory tissue is in between them [68].
20 kHz	Breast tumor tissue of 58 patients was examined. Malignant tumors have much higher capacitance values compared to benign tumors [66].
20 kHz – 100 MHz	Conductivity and permittivity comparisons of tumor and peripheral tissue. Sample tissue results showed that cancerous tissue has higher permittivity and conductivity values [69]. (σ is in between 2-8 ms/cm at the center of the tumor and 0.3-0.4 ms/cm for the healthy tissue)
3 MHz - 3 GHz	Malignant tissues have higher conductivity and a permittivity value compared to healthy tissues especially frequencies below 100 MHz. Conductivity is 1.5-3 mS/cm for healthy tissue and 7.5-12 mS/cm for malignant tissues and permittivity is 10 for healthy tissue and 50-400 for malignant tissues [70].
3.2 GHz	There was no significant difference observed in between the conductivity and permittivity of the benign and malignant tumor tissues. This might have occurred due to overshadowing effect of polar water [73].

In breast cancer detection, either invasive or non-invasive measurement methods can be considered. In the invasive method, current electrodes are inserted into the body and generally four-electrode configuration is used. Current is penetrated into the tissue by the help of two electrodes. Another pair of electrodes is used to record the voltage responses [74]. In the non-invasive technique, there is no electrode penetration into the tissue. As explained in the previous sections, current electrodes are located on the tissue (or current is carried out via electromagnetic coils). In both cases, applied AC Current should be within safety limits for in vivo studies.

Moritimo and his colleagues implemented in vivo invasive impedance measurements of breast tissue in the frequency range of 0-200 kHz [75]. 5 μ A current was applied with current electrodes which were inserted within a coaxial needle. Equivalent circuit model was used in this study. The authors report that impedance imaging method can be used to separate malignant breast tumor from benign breast tumor. Singh *et. al.* employed the electrical impedance measurement approach and evaluated the female breast over the frequency range of 100 Hz-100 kHz (in vivo non-invasive measurements) [76]. They concluded that, healthy breast tissue has lower permittivity and higher impedance compared to malignant tumor tissue. Another important non-invasive impedance measurement study was performed by Ohmine [77]. Breast impedance measurements of 24 patients were recorded with a four electrode configuration system. It is concluded that breast tumors can be separated using non-invasive electrical impedance measurement techniques.

Literature survey shows two important points: 1) the electrical impedance of malignant breast tumors and benign tumors are different. This can be used as an important indicator in the diagnosis of the cancerous tissue and may decrease the number of benign biopsies. 2) Cancerous breast tissue has significantly higher electrical conductivity (lower impedivity) compared to the surrounding healthy breast

tissue. Therefore, electrical impedance technique can be used to diagnose the cancerous tissue in the breast.

Recent studies on EIT imaging have been entirely focused on data acquisition and image reconstruction. Dartmouth College Group developed the EIT system for breast examinations. System was firstly designed by Hartov and his colleagues [79]. It was 32-channel, multi-frequency 2D EIT imaging system. Newton's method was used for image reconstruction. Forward and inverse problem were figured out with a finite element method using a dual mesh approach. Voltage was calculated in the forward problem and permittivity and conductivity were figured out in the inverse problem. Then, feasibility studies of breast imaging were implemented by Osterman [80]. AC Voltage is applied over the frequency range of 10 kHz-1 MHz with an electrode array (16 electrodes) on breasts. Test was applied on 13 woman breasts. Results showed that, although the sensitivity of the system is good, it cannot accurately detect the tumors. The primary problem had arisen from the nature of the 2D impedance measurements

An experimental 3D electrical impedance mammographic system for breast cancer diagnosis was developed by Wtorek and his friends [81]. The system is composed of a sensing cap, a digital signal processor and a computer. 64 electrodes are located inside and outside of the hemisphere chamber. Outer electrodes are used to apply current or voltage and inner electrodes are used to measure the current or voltage obtained from the breast tissue. The image is reconstructed according to the 3D electrical impedance distributions obtained from the measured potential differences. The disadvantage of this system is limitation of the electrode numbers. Only 64 electrodes can be used and this leads to decrease in the system resolution.

A 3D electric mammogram system was developed by Cherepenin and his colleagues and it was patented by Technology Commercialization International Inc., USA [82,

83]. In this system, there is an electrode plane consisting of 256 electrodes. In addition, 2 more electrodes were used as an AC current source and a reference point. 1 mA current was applied at 10 kHz and 3D images were reconstructed with a modified back projection.

Rensselaer Polytechnic Institute research group has also important studies on EIT for breast cancer detection [84]. They implemented numerical and experimental phantom study. In the experimental setup, agar phantoms were inserted in a saline filled rectangular tank in different locations. A malignant tissue was modeled with an agar phantom and healthy tissue was modeled with a saline solution. Conductivity of the saline water was 300 ms/m and the agar was 900 ms/m. Current was applied by copper electrodes and 4 x 4 electrode array was used to measure voltage data. Inhomogeneity's position could be observed in the reconstructed images. However, depth resolution was low in the experimental results.

Electrical Impedance Mapping (EIM) Technique has also been used to detect breast tumors. In this method, electrode configuration is planar and electrodes are mounted on the breast. Current or voltage is applied to the body with an electrode array located on the breast tissue and a reference electrode usually held in the patient's hand. Local impedances are sensed by the electrodes in the array and 2D images are mapped by these projected data using image reconstruction methods. Although two different versions of EIM system exist, only one of them is commercially available. First system was developed in Russia by the Yaroslavl research group [85], and the other one which is TS2000 was designed in Israel [83]. Siemens reproduced and marketed the TS2000 system, which is the only commercial electrical impedance imaging system used in breast cancer diagnosis. This system got also FDA's (US Food and Drug Administration) approval as an adjunctive tool to X-ray mammography [86].

For the clinical use of breast cancer detection a multi-frequency EIT system was proposed by Halter et al. [87]. The system has fast data acquisition rate and developed signal processing architecture that minimizes the imaging duration. The frequency range of the system is in between 10 kHz to 10 MHz. Innovations of this system are wide operating range, speed and accuracy. It has 80 dB signal to noise ratio (previous systems had 60-70 dB SNR value) at high frequency operations.

1.2. Infrared Thermal Imaging

1.2.1. Theory of Thermal Imaging

An infrared thermal camera measures and images the emitted radiation (called as thermograms) from an object in the infrared region of the electromagnetic spectrum. The radiation is a function of object's surface temperature and emissivity. Absorption of the atmosphere also affects the incoming radiation from the object.

The electromagnetic spectrum is divided into different wavelength regions (bands) as shown in Fig 1.1.

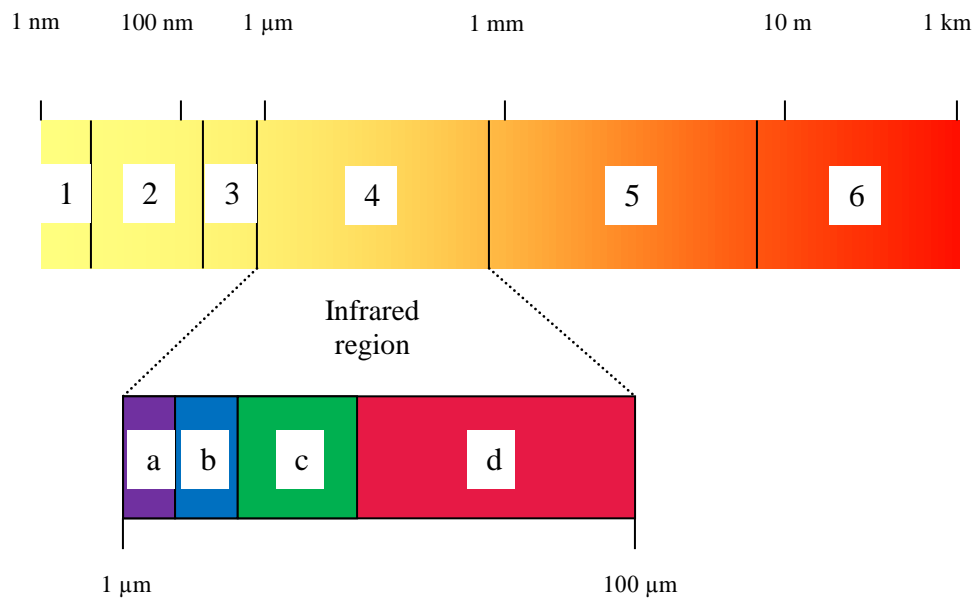


Fig. 1.1 Electromagnetic Spectrum (Region 1 belongs to X- ray band, 2 is ultra violet band, 3 is visible light band, 4 is infrared region (region a shows near infrared, b shows middle infrared, c shows far infrared and d is extreme infrared region), 5 is microwave (radar) band and 6 is radio frequency band)

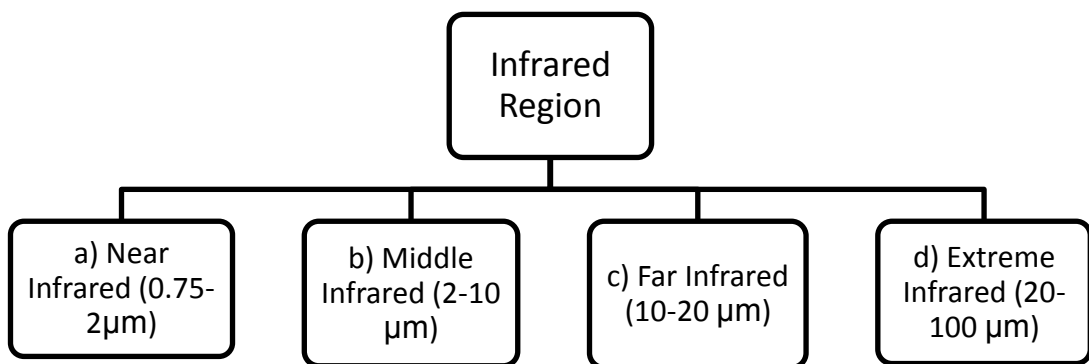


Fig. 1.2 Subsections of Infrared Region

All objects emit radiation above absolute zero. The relationship between the temperature and amount of the radiated energy is determined by the Stefan-Boltzmann Law. It can be obtained by integrating Planck's formula from $\lambda=0$ to $\lambda=\infty$.

$$W = \sigma T^4 \text{ (Watt/m}^2\text{)} \quad (1.1)$$

where, W is the total emitted radiation, σ is the Stefan-Boltzmann constant ($5.67 \times 10^{-8} \text{ W/m}^2\text{K}^4$), and T is the absolute temperature.

A blackbody is an object that can absorb all incoming radiation at all wavelengths. It can also be assumed as a perfect emitter. Blackbody radiation law states that infrared radiation is emitted by all objects above absolute zero. Max Planck proposed the blackbody law to describe the spectral distribution of the radiation from a blackbody as a function of wavelength. Following formula explains the blackbody spectral emittance at wavelength λ .

$$W_\lambda = \frac{2\pi hc^2}{\lambda^5 (e^{\frac{hc}{\lambda kT}} - 1)} \quad (1.2)$$

where,

c: Velocity of light ($3 \times 10^8 \text{ m/s}$)

k: Boltzmann's constant ($1.4 \times 10^{-23} \text{ Joule/K}$)

h: Planck's constant ($6.6 \times 10^{-34} \text{ Joule sec}$)

T: Absolute temperature (K) of a blackbody

λ : Wavelength (μm).

The peak of the spectral shape shifts to shorter wavelengths when the temperature of the object increases. Wien's displacement law describes the peak wavelength.

$$\lambda_{max} = \frac{2898}{T} \text{ (\mu m)} \quad (1.3)$$

In thermal imaging, thermograms are directly proportional to the amount of energy which is emitted, reflected and transmitted by the object. This process can be explained by the energy conservation formula.

$$\text{Incident energy} = \text{Emitted Energy} + \text{Transmitted Energy} + \text{Reflected Energy}$$

Where, the incident energy is the energy profile viewed by the thermal camera, emitted energy is the one that is tried to be measured, transmitted energy refers to the energy passing through the object and reflected energy shows the reflected energy from the surface of the object due to a remote thermal source. Radiation emission takes place from a warm object to a cold object. Power transfer occurs according to the Second Law of Thermodynamics from a warm material to a cold material. The measure of the ability to emit or absorb the radiation is called an emissivity [91]. Emissivity is the measurement of how much radiation is emitted from the object compared to a perfect blackbody of the same temperature. Theoretically, objects emissivity values range from 0 to 1. However, this is not possible in practice. Only a perfect black body has an emissivity of 1. Human skin exhibits emissivity ranging from approximately 0.972 to 0.998 [92]. In the wavelength of 3 μm to 14 μm , human skin behaves as almost a perfect absorber.

Total amount of emitted radiation from an object is proportional with emissivity, the object's area and the fourth power of its absolute temperature. Considering that the

human skin emissivity is within 1 % of a blackbody, surface temperatures of the body can be evaluated by measuring the infrared radiation emissions of the skin.

1.2.2. Thermographic Measurement

Since sun light scattering in the atmosphere and stray radiation from intense radiation sources are small enough to be neglected, they can be assumed as negligible in thermographic measurements [93]. To express the measurements due to a nearby body, however, reflections from the surroundings and attenuation in the atmosphere must be taken into account. Fig. 1.3 shows the schematic of a thermographic measurement system.

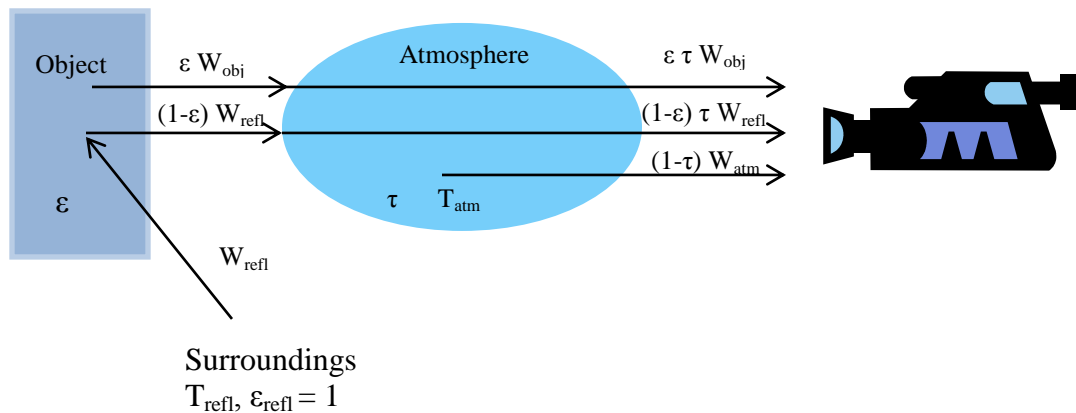


Fig. 1.3 Schematic of a Thermographic Measurement. 3 different radiations contribute the measurements of a thermal camera. Direct radiation from the object, radiations reflected from surroundings and radiations from the atmosphere.

Let us assume an object of temperature T_{obj} (K) which has an emission W_{obj} (Watt/m²). Assuming a proportionality constant as C , the radiation generates a camera output signal V_{obj} (V) where

$$V_{obj} = C W_{obj} \quad (1.4)$$

The total received radiation power is composed of three collected radiation powers which are emission from the object, reflected emission from ambient sources and emission from the atmosphere.

Due to the emission from the object, the received radiation is $\varepsilon \tau W_{obj}$, where ε is the emissivity of the object and τ is the transmittance of the atmosphere.

Due to reflections of the ambient sources (at temperature T_{ref}) from the same object, an interfering radiation of $(1-\varepsilon) \tau W_{refl}$ is also detected.

In this formulation, some simplifications and assumptions are made. For example, T_{refl} is assumed same for all emitting surfaces seen from the object surface. Most of the case, it is the real situation. Secondly, the emissivity of the surroundings is assumed to be 1 in accordance with Kirchoff's law (all radiation interfering with the surrounding surfaces will ultimately absorbed by the same surfaces) [94].

If $(1-\tau)$ is the atmosphere emittance and T_{atm} is the atmosphere temperature then the third interfering term is $(1-\tau) W_{atm}$.

Consequently, the total collected radiation can be calculated as:

$$W_T = \varepsilon \tau W_{obj} + (1-\varepsilon) \tau W_{refl} + (1-\tau) W_{atm} \quad (1.5)$$

When we multiply each term with a constant C, the camera output is obtained,

$$U_{\text{tot}} = \varepsilon \tau U_{\text{obj}} + (1-\varepsilon) \tau U_{\text{refl}} + (1-\tau) U_{\text{atm}} \quad (1.6)$$

Here,

U_{obj} : Calculated camera output voltage.

U_{tot} : Measured total camera output voltage.

U_{refl} : Camera output voltage of the reflected ambient sources.

U_{atm} : Camera output voltage due to atmospheric effects.

Then, the output voltage due to sole object radiation is

$$U_{\text{obj}} = \frac{1}{\varepsilon \tau} U_{\text{tot}} - \frac{1-\varepsilon}{\varepsilon} U_{\text{refl}} - \frac{1-\tau}{\varepsilon \tau} U_{\text{atm}} \quad (1.7)$$

Object temperature can be found by converting this voltage into the temperature by using equation (1.5).

1.2.3 Development of the Medical Infrared Imaging and Infrared Breast Imaging

The discovery of infrared portion of the electromagnetic spectrum was made accidentally during the search for a new optical material by Sir William Herschel in 1800. In the meantime, the first detectors for invisible radiation were invented in 1830's. The temperature dependent electrical resistors (bolometers) were developed in 1880 [94]. The quantum detectors (photodiodes) were proposed in between 1870 and 1920. They interact directly with the impacting photons and cause generation of

electron pairs. Then, lead sulfide detectors (PbS) which operate in 1.3 to 3 μm band were invented in 1930's. Mid wave band (3-5 μm) operations became possible by the invention of indium antimonide (InSb) detectors in 1940's. Mercury cadmium telluride detectors (HgTeCd) were developed to work in the far infrared region in 1960's. The most developed and cooling system required quantum detectors made the detection of infrared radiation emission possible in the range of 2 to 15 μm . They have higher sensitivities and faster integration times.

Infrared thermal imaging had initially started to be used for military research in airborne applications [16]. It was firstly used for clinical approaches in the year of 1970's. There were two alternative methods in those days: Liquid crystal contact thermography and noncontact blackbody infrared imaging.

Since the liquid crystal contact thermography has poor specifications as low thermal resolution ($\pm 0.5^\circ\text{C}$), low spatial resolution ($\pm 5\text{mm}$) and slow response time (>60 sec), the usage of those systems were not broad. Although the emissivity of the skin is $>98\%$ and blackbody emission at 30 to 34 $^\circ\text{C}$ approaches its maximum in the region of 8 to 12 μm wavelength, the performance of the cameras could not be sufficient at that temperature levels. Limitations of the digital infrared cameras were:

- The spatial resolution was poor (resolution of 128 x 128 pixels).
- The thermal resolution was limited (approximately $\pm 0.1^\circ\text{C}$).
- The single detector scanning infrared cameras were so slow (need more than four seconds to get a single thermal image). The process of that much slow data acquisition yields temperature and spatial resolution decrease, and hence,

this slow thermal imaging leads to a physiological noise of the order $\pm 0.2^{\circ}\text{C}$ in average temperatures [14].

Until 1980's infrared cameras had less corrected optical aberration performance when the imaged surface was oblique to the focal plane of the camera. This was leading to lower efficiency on temperature measurements in the image surface and limitations were causing errors up to 1°C .

Infrared cameras that have InSb detectors are sensitive to infrared radiation in the range of 3 to 5 μm . In that range, it is known that the human skin has 10 to 15 % reflectivity. However, at earlier times, most of the clinicians had not enough information about artifacts due to skin reflectivity.

After approaching the 90's, very fast focal plane array cameras in the $>8\ \mu\text{m}$ region (>100 frames/sec, 256×256 pixels or more per frame) and high resolution fast scanning cameras (>10 frames/sec, 512×512 pixels) were developed. Next, third generation Focal Plane Arrays (FPAs) were being designed. They provide larger number of pixels (1024×1024 pixels), better thermal resolution, and image and signal processing properties are added, so-called on chip signal processing. Since it does not include mirrors, the image quality improves and mechanical noise reduces (less moving part in the camera). The third generation FPA detectors can capture wavelength from 3-5 μm (mid-wave band) to 8-12 μm (long-wave band). A level of $20\ \text{mC}$ differences in temperature can be reliably sensed with the state of the art thermal infrared cameras [15].

Literature reviews in recent years show that image processing techniques (i.e., computer aided diagnosis) are required due to several reasons (most importantly the limitation of human visual system in early breast cancer detection). Image processing for thermal imaging can be grouped as image enhancement, asymmetry analysis, and

classification. The drawback of thermal imaging is its lack of resolution due to blur produced by rather high level of noise. By using image enhancement algorithms the effective resolution of infrared thermal images can be improved removing the noise and preserving the edges of image. This kind of algorithms such as Synder et. Algorithm which uses minimization strategy (mean field annealing) can make an optimal estimate of the missing pixels. If images are relatively symmetrical, small asymmetries may denote a suspicious region. This is the idea of asymmetry analysis for mass detection in breast cancer area. Asymmetric abnormalities can be observed by the help of pattern classification techniques [15].

1.2.3.1 Thermal Imaging of Breast

Breast cancer is the most frequent cancer type in women (30 % of all cancer kinds). In 2002, approximately 213500 women got this cancer in the USA and 40500 of them died from this sickness [16]. In our country, every year approximately 10000 women gets breast cancer and unfortunately 2600 of them die [95]. However, if it can be diagnosed earlier, the patient has an 85% chance of getting over.

Thermal imaging is a valuable tool that may decrease the death rates due to breast cancer. It can also give complementary information about the future development of cancerous tissue. Abnormal breast thermogram shows a significant risk indicator for the breast cancer. Many studies were reported that infrared imaging can be used as an important risk marker [103], [107-110]. Thermal imaging gives information about metabolic activity and functional tumor induced angiogenesis instead of structural knowledge such as size of the tumor and micro calcifications [99]. Infrared imaging can show indications almost 10 years before the development of breast cancer unlike other imaging modalities. When this important ability combines with its proven

specificity and sensitivity, thermal infrared imaging becomes irrevocable in the breast cancer diagnosis.

The first clinical usage of infrared imaging was implemented by Lawson in the year of 1956 [96-98]. This study was performed after the discovery that cancerous breast tissue causes more temperature increase than healthy breast. Many medical centers have used thermal imaging for diagnostic aims until 1970's. Thermographic imaging had an approval from the Food and Drug Administration as an adjunctive diagnostic imaging for the breast cancer detection in 1982 [99] and infrared imaging has been used up to now in the breast cancer screening.

In US, infrared imaging has been started by Gerson-Cohen in 1965. He was working as a radiologist in the Albert Einstein Medical Center. In his study, 4000 cases were carried out with a sensitivity of 94 % and a 6 % false-positive rate using Barnes thermograph method [100]. Then, thermal imaging was used in a gynecology by Hoffman. In this study, 23 malignancies were detected in 1924 patients with 91.6 % sensitivity and 92.6 % specificity rate [101]. Clinical prospective studies on breast cancer have been implemented by many groups and similar false-negative and false positive rates were acquired.

Isard had studied on thermography and mammography together for 3 years period with 10000 patients. He has experienced that combining imaging modalities (thermography and mammography) improves the cancer detection rate. When, mammographic scanning used individually, the detection rate is 7 per 1000. On the other hand, this rate increases to 24.1 per 1000, when combined imaging modalities are used. According to his contention, combining mammography with infrared imaging improves the sensitivity rate of detection by 10 % [102]. Spitalier imaged 61000 women breast in a 10-year period with an infrared camera. He was able to detect 91 % of the grade T0 tumors (tumors smaller than 1 cm) with a 89 %

sensitivity and a specificity [103]. His conclusion is; thermographic measurement is an indicator in 60 % of the cases for the cancer patients.

Parisky and colleagues implemented a 4-year clinical infrared imaging study to examine suspicious lesions which were detected by mammography. 769 women with 875 biopsied lesions were imaged; and 688 benign and 187 malignant evidences were detected [104]. 97 % sensitivity was obtained in the diagnosis of breast cancers for the suspicious lesions. Nyirjesy and associates implemented a study which compares the accuracy of clinical examination, thermography and mammography in the breast cancer detection. 16778 patients were participated the study. There were 8757 asymptomatic patient, 4715 confirmed carcinoma patients and 3305 histologically diagnosed benign breast cancerous patients. The comparison of other imaging modalities which were approved by National Cancer Institute (NCI) was also given in this paper. X-ray mammography was able to detect all tumors with an average of 73 % specificity and 80 % sensitivity. This rate was 85 % specificity and 88 % sensitivity in the thermography. On the other hand, the sensitivity of a clinical examination was 75 %. The point that the author reached was none of the imaging modality by itself was sufficiently accurate to diagnose the breast carcinoma. More accurate results can be obtained using imaging modalities in combined with each other [105]. In Thomassin and et al. study, 130 malignant tumors ranging in diameter 3-5 mm were detected out of 4000 confirmed breast cancers. 10 % of them were diagnosed by mammography, 50 % of the patients by thermography and rest of them which could not be detected either mammography or thermography were diagnosed (40 %) by multi modal imaging (mammography and thermography) [106].

Antiangiogenesis therapy is one of the important new breast cancer treatments. In this treatment, the location of antiogenic process depending on the tumor's location should be detected. In the future, antiangiogenesis therapy with the use of thermal

imaging is considered together in the biological assessment and breast cancer treatment [111].

A. W. Guy implemented a thermographic study with tissue equivalent phantom models. He applied electromagnetic fields at different frequencies by various microwave sources as plane wave, aperture, slot and dipole sources and observed the heating pattern due to the electric field [112]. Fat, bone and muscle tissue were modeled with saline solution, powdered polyethylene and aluminum powder. Similar study was developed by R. P. Zimmer and et al. on live animal tissue (rat, mouse and dog). Tumor tissue was stimulated by microwave energy (RF power source) to obtain differential hypothermia and almost 25 °C temperature differences were acquired between the tumor and surrounding tissue. The aim of the study was, while increasing the sensitivity of cancerous tissue to chemotherapeutic drugs, decreasing the bad effects of anticancer drugs to other parts of the body by increasing the temperature difference of cancerous and surrounding tissue [113]. P. Bernardi and associates have a study which is related with the temperature increase and SAR distribution in the phantom by microwave cardiac ablation. In this simulation study, bio-heat equation is solved with a two dimensional finite difference time domain method. Phantom was designed as a two-layer heart model and a catheter antenna was placed in it. The muscle equivalent phantom was composed of 75.45 % water, 15.2 % polyethylene powder, 8.45 % TX-150 and 0.9 % NaCl. Electromagnetic power was absorbed from the cardiac tissue and it led to a temperature increase in the corresponding tissue. As a result, the lesion is detected from 5 mm depth in the heart with low blood perfusion [116]. RF current with 16 W of radiated power was applied by catheter electrodes over the cardiac tissue for 60 second.

The feasibility study on using electrical impedance imaging for hyperthermia monitoring was performed by J. Conway. Experiments were implemented both in vivo and in vitro. In in vivo experiment, the scapula of a volunteer was heated using a

microwave diathermy applicator. An agar phantom (conductivity 2 S/m) was used for in vitro experiments. Current was applied with a pair of electrodes at 50 kHz and measured with a 16-electrode system. Image artifacts were formed in in vivo experiments due to a body movement, electrode contact problem and blood flow effects [114-115]. Sensitivity (1 °C) and spatial resolution (1.5 cm) of the system should be improved and further developments are necessary to present this imaging system for monitoring the hyperthermia treatment in clinic.

M. Mital and E. P. Scott have studied on diagnosis of the embedded tumors with an infrared camera. They placed a heat source in a cylindrical biological phantom and imaged the temperature distribution on the phantom surface. The heater (resistance 32 Ω) was embedded in the agar to simulate the tumor tissue's temperature increase. Power dissipation of the heat source was adjusted by changing the voltage of the heater. Infrared camera had 80 mK thermal resolution and the emissivity of the agar phantom (1 % solution of agar) was 0.97. Genetic algorithm was implemented to be able to determine the heat generation rate and location of the source from temperature distributions [117]. Blood perfusion, convective and radiative boundary conditions were not taken into account in this study.

The first study comparing the performance of infrared cameras used for the diagnosis of breast cancer was implemented by R. Joro and et al. in 2008. The ability of detecting the cancerous tissue of quantum well infrared photodetector (QWIP), micro bolometer (MB), and photo voltaic (PV) detectors were tested on 15 patients with confirmed breast cancer tissue (size 6-100 mm). Image processing algorithms (pixel based analysis and windowed regional frequency analysis) were applied to the dynamic IR image data for image enhancement. Results showed that InSb PV camera has the best performance in distinguishing the vasomotor and cardiogenic frequency differences of cancerous and healthy breast tissue. GaAs QWIP camera has also satisfactory imaging performance. The camera sensitivities of both cameras are pretty

close to each other. However, QWIP cameras have a long integration time compared to PV cameras, so they cannot collect data as fast as PV cameras. Since, PV camera have higher Quantum Efficiency (QE), it can detect signals with a small amount of photon energy. Although, image processing algorithms were applied to the image data, the performance of MB camera was not sufficient for the detection of cancerous tissue [15], [119].

F. J. Gonzalez presented a thermal simulation study of breast tumors. Woman breast was modeled with a 9 cm radius hemisphere and the tumor tissue was embedded in it as a sphere. In this study, it was investigated at which depths the smallest size of cancerous tissue can be detected by modern state-of-the-art thermal infrared cameras. Pennes Bio-Heat equation is figured out with a finite element method using COMSOL Multiphysics computer software. The noise equivalent temperature difference of thermal camera was 20 mK. The point that the study reached was, 3 cm tumors can be detected from 7 cm depths and smaller tumors can be diagnosed if they are located closer to the skin surface [24]. L. Jiang and associates developed a paper on modeling the thermography of the woman breast under elastic deformation. They modeled the woman breast by taking the gravity-induced elastic deformation into account. This is the first study adding this parameter beside the metabolic heat generation, blood perfusion, thermal and electrical boundary conditions, and thermal and electrical conductivities of breast tissue. Numerical breast models were figured out using 3D finite element method by including the thermal and elastic properties of breast tissue. Temperature differences due to tumor tissue were obtained numerically on the surface both for static and dynamic thermal states. The developed modeling technique establishes a connection between breast thermography and pathological and physiological factors due to cancerous tissue [118].

The most important problem with thermal imaging is the lack of skilled technicians and clinicians. Most of the clinicians and radiologists are familiar with the structural

anatomy and medical teaching but they don't know much about the thermodynamics, thermo kinetics and physical and biological basis of infrared imaging. However, technological developments in digital processing, image acquisition and user friendly software facilitate the use of infrared imaging. Multispectral images could be obtained with the improvements in narrow-band filtering. With dual band thermal cameras, two different images for the same object could be acquired at different wavelengths. Software advances in smart processing (artificial intelligence) make the postimage processing of raw data possible. Most important and commonly used ones are artificial neural networks, automated target recognition and threshold algorithms [99]. Data summation is used in artificial neural network algorithm to obtain pattern recognition. On the other hand, threshold and automated target recognitions algorithms use a normative data base. These improvements have raised the accuracy of the system and have reduced the need for skillful operators.

1.3 Motivation of the Thesis Study

Breast cancer is the most mortal illness among women. Literature survey shows that there is no gold standard methodology for breast screening. On the other hand, X-ray mammography is the most common imaging modality approved by FDA. There are also many complementary imaging methods like ultrasound, PET and MRI. However, they all have some several drawbacks. For instance, the most preferred one; mammography has lower sensitivity and specificity values. Due to the morphologic similarity, it cannot separate malignant and benign tumors. Biopsy is needed for definitive diagnosis. It also ionizes radiation and is not comfortable for patients. Ultrasound cannot detect tumors at deeper locations and cannot show microcalcifications. Exam duration restricted imaging area, interpretation problems,

difficulty of intravenous access are also disadvantages of other imaging modalities. These drawbacks urged us to develop a new powerful imaging modality.

Electrical impedance imaging and infrared imaging are emerging imaging modalities for breast screening. Although they have lower spatial resolutions and poor signal to noise ratios, EIT systems can produce high contrast images and they are inexpensive and safe. Examination process is very short and its sensitivity and specificity are improving with developing technology. Multi-frequency operation ability gives an opportunity of getting more than one image for the same object and raises the detection accuracy.

On the other hand, abnormal thermography is the highest risk indicator for the future development of the breast carcinoma. Infrared imaging is the only imaging modality which can image the metabolic aspect of the breast [99]. Thermal image is an indicator of abnormal pathophysiology and physiology [120]. Studies has also showed that with higher sensitivity and specificity, distinguishing ability of malignant tissue from benign tissue, thermal infrared imaging is an important candidate to be the major complementary imaging modality for breast cancer screening. In the meantime, thermal imaging is risk free, non-ionizing, patient – friendly, painless and has better price to performance ratio compared to other imaging systems. However, it has also some problems that leave it still a candidate to be a major front-line imaging method.

Smaller tumours cannot be detected from deeper locations. Temperature increases on the skin surface occur due to blood perfusion and metabolic heat generation of the tumor tissue. However, the temperature contrast on the breast surface due to metabolic heat generation of the cancerous tissue is not sufficient to be sensed when the tumor is located at deeper regions of the breast. It cannot produce adequate amount of temperature difference on the skin surface. The noise equivalent

temperature difference of modern state-of-the-art thermal infrared cameras is approximately 20 mK, so tumor tissue should create at least this amount of temperature contrast to be detected. This is not possible especially for smaller tumours located at deeper regions.

Our motivation starts at this point. We developed a new method that increases the temperature contrasts of tumor and healthy tissue. By applying electrical currents within medical safety limits, an extra electromagnetic energy is induced inside the tissue. Creating an extra energy source, the new active mode is formed beside the existing passive mode. This new energy source generates extra temperature rises in the breast tissue. Since the electrical conductivity of cancerous tissue is more than (5-10 times) the healthy tissue, the temperature increase of the tumor will be higher compared to normal breast tissue. Thus, temperature contrast is actively increased and imaging performance will be improved, and hence, cancerous tissue can be detected at deeper locations. The new imaging modality named as “Medical Electro-Thermal Imaging” is shown in Figure 1.4.

Another crucial innovation is the frequency study. Since electrical conductivity of tissues changes with frequency, it is possible to obtain more than one thermal image for the same body. By applying electrical stimulation at different frequencies, numerous temperature distribution images can be obtained for the same patient. Temperature distributions alter with respect to the frequency of the applied current. This will increase the diagnosis accuracy.

Combining electrical impedance imaging with thermal infrared imaging, a hybrid modality, which we name Electro-Thermal Imaging, is proposed. This new functional imaging modality utilizes both techniques and minimizes drawbacks of these two imaging systems. Based on the two innovations mentioned above, imaging performance is expected to be improved by increasing the sensitivity and specificity

of EIT and Infrared Imaging Systems. Preliminary works on Electro-thermal imaging show the potential of the technique to be a major front-line imaging method for breast screening.

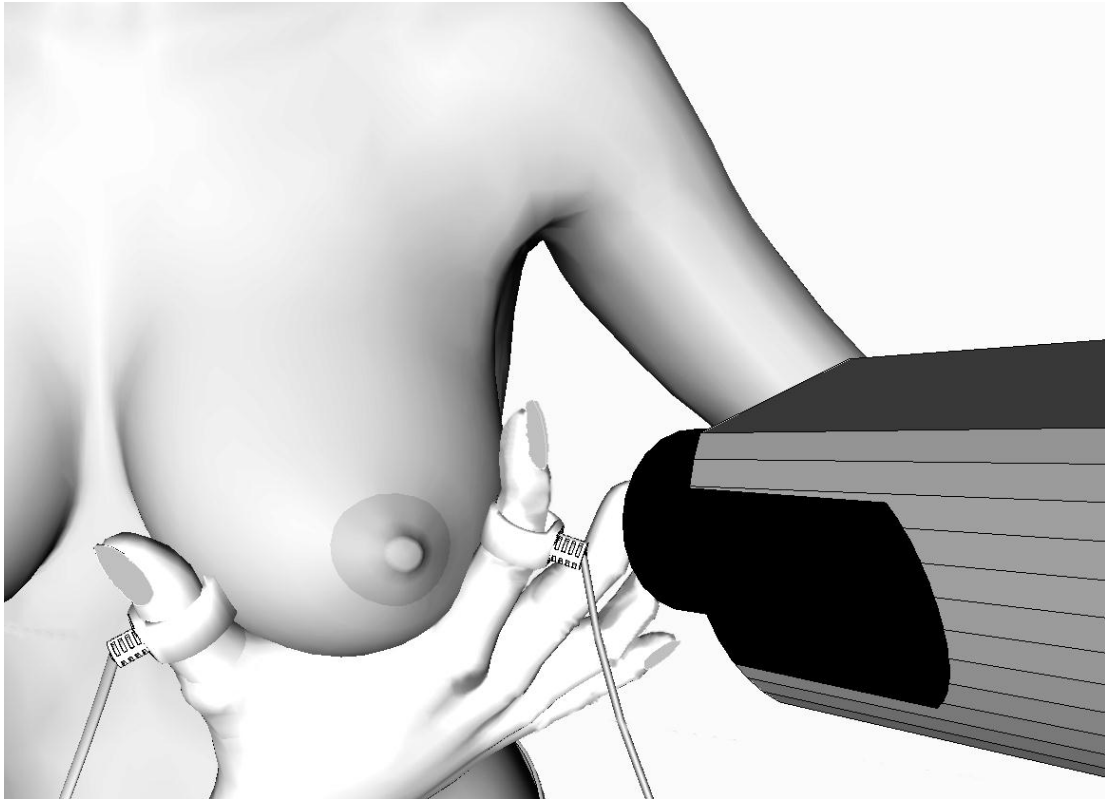


Fig. 1.4 Schematic of an Electro-Thermal Imaging System. Current is applied to the female breast with a pair of electrodes inserted on two fingers. Since fingers are mobile, current can be injected into the desired location. Thermograms of the breast are obtained with an infrared camera.

1.4 Objectives of the Thesis Study

The objectives of this thesis study are as follows:

- To identify the governing partial differential equation for the temperature distribution inside the body due to internal (metabolic heat generation, blood perfusion) and external (possible external heat source, electrical currents applied from the body surface) sources.
- To identify the governing partial differential equation for the solution of the current density inside the conductive body due to electrical currents injected from the body surface.
- To identify the simplifying assumptions in the partial differential equations and investigate the feasibility of the proposed technique using analytical techniques.
- To investigate the feasibility of the proposed technique using simulations by developing two- and three-dimensional numerical models.
- To develop a thermal body phantom (simulating a tumour in the breast) and make experimental studies using an infrared camera.

1.5 Outline of the Thesis Study

The thesis has the following parts:

- Chapter 2 presents the theory of the Electro-thermal imaging. By explaining electromagnetic and heat problems, method and schematic of a modified form of Pennes Bio Heat Equation is presented. A detailed explanation of the electromagnetic theory, heat theory and problem solution is given in the Appendix part.
- Chapter 3 presents the simulation studies. In this chapter, first the numerical model is explained. Next, two and three dimensional results (temperature images due to breast carcinoma) are presented.
- Hardware work and experimental studies are covered in the fourth chapter. The explanation of the current generator and frequency characteristics of current driver's output resistance are presented in this chapter. Images from a breast phantom simulating breast carcinoma are shown that support the simulation studies.

CHAPTER 2

ELECTRO-THERMAL IMAGING

2.1 Introduction

The block diagram of Electro-Thermal imaging system is shown in Fig. 2.1. The system, apart from external current sources, is a standard medical infrared imaging system. An infrared camera standing at a distance from the body records the emitted radiation. The camera, in this *passive mode*, i.e., no external sources are applied, displays the surface radiance distribution due to the internal sources (metabolic heat generation and blood perfusion). In this mode, a *static* image of the body is recorded as long as the internal sources remain constant.

Dynamic images of the body can be recorded if external heat sources (usually cold) are applied. In such a case, a series of images reflecting the transient behaviour of the tissues (changes in the temperature distribution) are displayed.

The system can be used in *active mode* by applying different energy sources (possibly electromagnetic energy in microwave or radio frequency range). In this thesis, an active mode of operation is proposed that uses electrical current sources applied on the body surface. The rationale behind the use of electrical currents in thermal imaging stems from the fact that tumour angiogenesis increases the electrical conductivity of tissues. This may yield differences in current pathways and produce noticeable changes in the temperature distribution with respect to the distribution

obtained in the passive mode. Furthermore, several thermal images can be obtained by changing the electrode positions and/or the operation frequency.

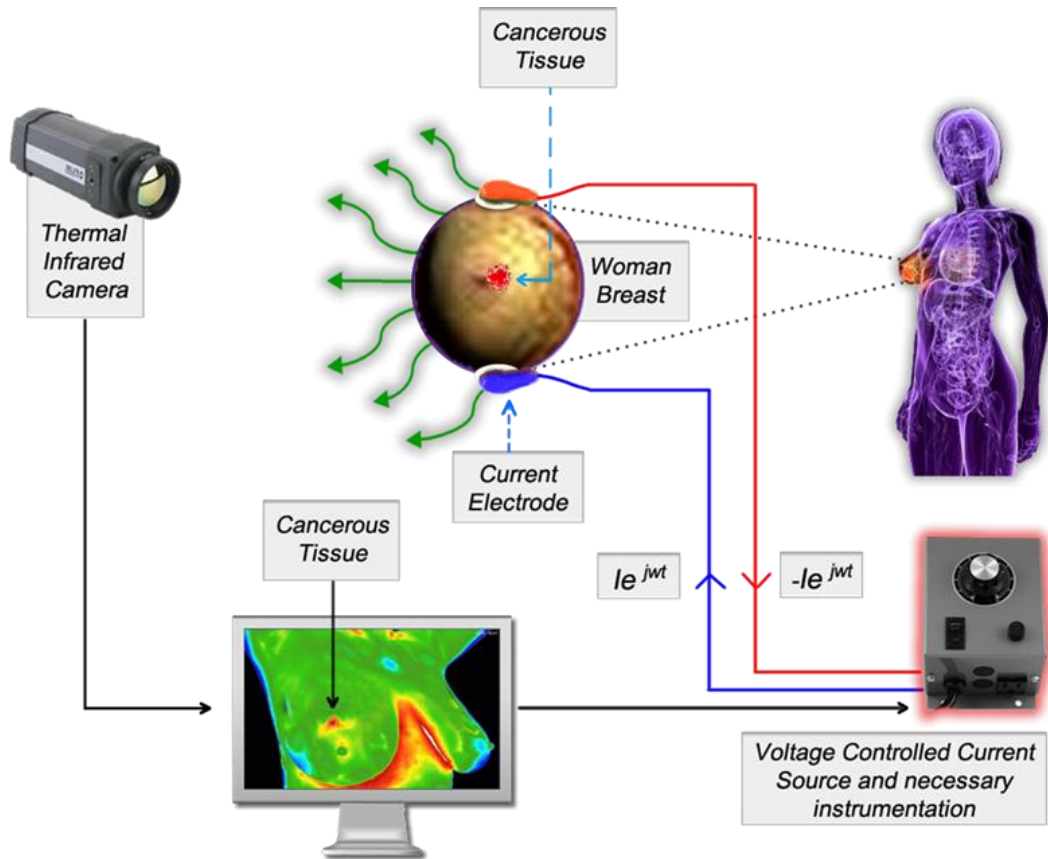


Fig. 2.1 Block diagram of Electro-Thermal Imaging System. Current is applied from the surface of the breast with a voltage controlled current source and necessary instrumentation, and temperature distribution of the breast is imaged using an infrared camera.

2.2 Theory

Fig. 2.2 shows the schematic of the electromagnetic problem. The electrical model of the body is represented using permeability $\mu = \mu_0$, electrical conductivity σ and permittivity ϵ . Sinusoidal currents (assuming $e^{j\omega t}$ time dependence) are applied using the two electrodes attached on the body surface at points A and B. Applied currents generate an electric field in the conductive body.

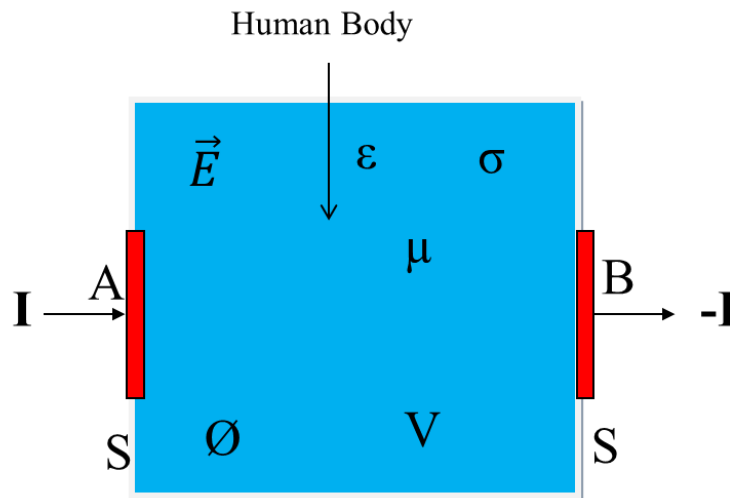


Fig. 2.2 Schematic of the Electromagnetic Problem. A and B are entry and exit points of the current. \vec{E} is the electric field, ϕ is the scalar potential, σ is the electrical conductivity, ϵ is the permittivity and μ is the permeability.

Starting from the fundamental electromagnetic field equations, the steady-state electric field $\vec{E} = -j\omega\vec{A} - \nabla\phi$ can be calculated using the following coupled partial differential equations,

$$\begin{aligned}\nabla^2\vec{A} - j\omega\mu(\sigma + j\omega\varepsilon)\vec{A} - \mu(\sigma + j\omega\varepsilon)\nabla\phi &= 0 \\ \nabla \cdot [(\sigma + j\omega\varepsilon)\nabla\phi] + \nabla(\sigma + j\omega\varepsilon) \cdot j\omega\vec{A} &= 0\end{aligned}\quad (2.1)$$

and boundary conditions

$$\sigma \frac{\partial\phi}{\partial n} = \begin{cases} I & \text{on } A \\ -I & \text{on } B \\ 0 & \text{otherwise} \end{cases}\quad (2.2)$$

where, \vec{A} is the magnetic vector potential, ϕ is the scalar potential, and I is the current applied from the surface.

To obtain the temperature distribution of the tissue, Pennes proposed a method which describes the effects of metabolic generation and blood perfusion over the energy balance. The most common approximation method for the heat problems in biological tissues is the Pennes Bio Heat Equation [23]. It explains the thermal interaction between tissues and perfused blood in detail.

$$\rho C \frac{\partial T}{\partial t} + \nabla \cdot (-k\nabla T) = Q_b + Q_{met}\quad (2.3)$$

where, ρ is the density (kg/m^3), C is the specific heat (J/kgK), T is the absolute temperature (K), k is thermal conductivity (W/mK), Q_b is the heat source due to blood perfusion and Q_{met} is the metabolic heat generation (W/m^3).

The first term on the right hand side of equation (2.3) is the source due to blood perfusion which can be expressed as

$$Q_b = \rho_b C_b W_b (T_b - T) \quad (2.4)$$

where, ρ_b is blood mass density (kg/m^3), C_b is the blood specific heat rate (J/kgK), W_b is the blood perfusion rate ($1/\text{s}$), and T_b is the blood temperature (K) which is approximated to the core temperature of the body, and the temperature of the venous blood is approximated to T which is the unknown temperature value (local tissue temperature (K)).

Law of conservation of energy states that the heat lost from the skin surface is in a constant equilibrium with the heat supplied by the vascular flow to the skin in the steady state. Thus, heat transfer from the front skin surface (by both convection and radiation to the surrounding air and surfaces at specified temperatures) should be considered as the boundary conditions:

$$Q_{conv} = hA_s(T_s - T_\infty) \quad (2.5)$$

$$Q_{rad} = \varepsilon\sigma A_s(T_s^4 - T_{sur}^4) \quad (2.6)$$

where, h is the convection heat transfer coefficient ($\text{W/m}^2\cdot\text{K}$), A_s is the surface area through which the convection heat transfer takes place, T_s is the surface temperature,

T_∞ is the temperature of the air, ε is the emissivity of a skin (0.95), σ is the Stefan-Boltzmann constant ($\text{W/m}^2 \cdot \text{K}^4$), and T_{sur} is the temperature of the walls, ceiling and floor. In this study, T_{sur} is assumed to be equal to the air temperature ($T_{sur} = T_\infty$).

Note that, the boundary condition at the front skin surface can also be written as [141]:

$$-k\nabla T = h(T - T_\infty) \quad (2.7)$$

Here, h ($\text{W/m}^2\text{K}$) represents the overall heat transfer coefficient due to the combined effect of radiation and convection, as given by equations (2.5) and (2.6), respectively.

To set the boundary condition at the rear surface of the breast, the temperature of the thoracic wall can be assumed to be the core temperature of the body (i.e., 310 K).

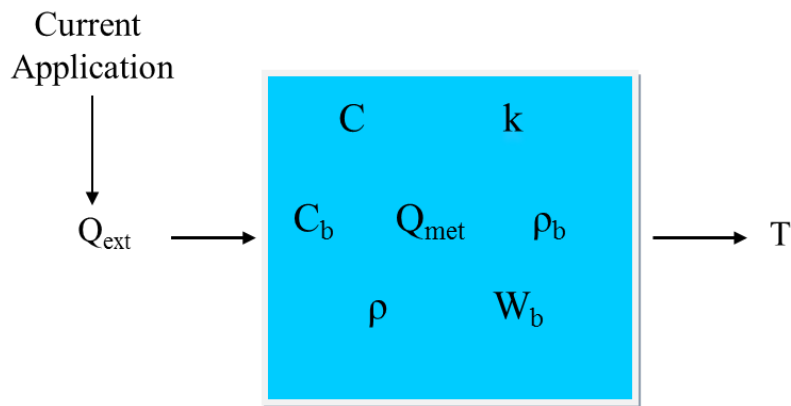


Fig. 2.3 Schematic of the Bio-Heat problem when electrical currents are included as heat sources. C is the is specific heat, ρ is mass density, k is thermal conductivity, ρ_b is blood mass density, C_b is the blood specific heat rate, W_b is the blood perfusion rate, Q_{met} is the metabolic heat generation, Q_{ext} is the heat source due to current application and T is the absolute temperature.

Due to the applied external current sources, a new term should be added to the right-hand side of the Pennes Bio Heat equation:

$$\rho C \frac{\partial T}{\partial t} + \nabla \cdot (-k \nabla T) = Q_b + Q_{met} + Q_{ext} \quad (2.8)$$

The external heat term Q_{ext} is calculated using the following Joule Heat Equation:

$$Q_{ext} = \frac{1}{\sigma} |J|^2 \quad (2.9)$$

where J is the electrical current density and σ is the electrical conductivity of the tissue.

2.3 Analytical Feasibility Studies

2.3.1 Evaluating the Time Constants of Different Tissues

The transient behavior of the heating process for different tissue types can be studied by using the homogeneous form of the Bio-Heat equation. Assuming a uniformly heated tissue of uniform material properties,

$$\rho C \frac{\partial T}{\partial t} + \nabla \cdot (-k \nabla T) = \rho_b C_b W_b (T_b - T) \quad (2.10)$$

$$\frac{\rho C}{k} \frac{\partial T}{\partial t} = \nabla \cdot (\nabla T) + \frac{\rho_b C_b W_b}{k} (T_b - T) \quad (2.11)$$

Due to uniformity, $\nabla \cdot (\nabla T)$ term drops and after multiplying each term of Equation (2.10) by $k/\rho C$ we obtain

$$\frac{\partial T}{\partial t} + T \frac{\rho_b C_b W_b}{\rho C} = \frac{\rho_b C_b W_b}{\rho C} T_b \quad (2.12)$$

Thus, the tissue temperature T rises exponentially to the blood temperature T_b . The time constant T_c of this exponential behavior is expressed as:

$$T_c = \frac{\rho C}{\rho_b C_b W_b} \quad (2.13)$$

According to the above formula, the time constants of different tissue types can be explored to investigate the speed of the heating processes in biological tissues. Table 2.1 presents the calculated values for different tissues.

Table 2.1

Healthy and Cancerous Tissue Characteristics and Calculated Time Constant Values
[22], [23], [24], [25]

	Healthy breast tissue	Cancerous breast tissue	Bone Marrow
Density of tissue (kg/m ³)	1020	1041	1810
Specific heat (J/kg°K)	3000	4440	1256
Density of blood (kg/m ³)	1000	1000	1000
Specific heat of blood (J/kg°K)	4200	4200	4200
Blood perfusion rate (1/s)	0.0018	0.009	0.00125
Time constant (sec)	404	123	433
	Dermis	Subcutaneous tissue	Muscle
Density of tissue (kg/m ³)	1000	1000	1040
Specific heat (J/kg°K)	3300	2675	3639
Density of blood (kg/m ³)	1000	1000	1000
Specific heat of blood (J/kg°K)	4200	4200	4200
Blood perfusion rate (1/s)	0.00125	0.00125	0.00125
Time constant (sec)	628	509	720

2.3.2 Temperature Rise due to an Applied Electrical Current: Transient Behaviour

Assuming a uniform tissue and uniform current excitation, all space derivatives in the Bio-Heat equation drops, yielding

$$\frac{\rho C}{k} \frac{\partial T}{\partial t} = \frac{\rho_b C_b W_b}{k} (T_b - T) + \frac{Q_{met} + Q_{ext}}{k} \quad (2.14)$$

or

$$\rho C \frac{\partial T}{\partial t} + \rho_b C_b W_b T = \rho_b C_b W_b T_b + Q_{met} + Q_{ext} \quad (2.15)$$

To obtain temperature changes with respect to the thermal equilibrium value, the first and second terms on the right hand side can be ignored. Thus, an exponential behavior can be observed as

$$\delta T(t) = \Delta T (1 - e^{-t/T_c}) \quad (2.16)$$

where, $\delta T(t)$ represents the differential change in temperature as a function of time and ΔT is the steady-state value of the temperature change

$$\Delta T = \frac{Q_{ext}}{\rho C} \quad (2.17)$$

To investigate the temperature rise in a cancerous tissue for a stimulation current of 1 mA/cm² (safety limit is 1 mA at 10 kHz [20]) the temperature rise ΔT is calculated. The electrical conductivity of cancerous breast tissue is taken as 1 S/m. For the given stimulation current, Q_{ext} is calculated as 25000 W/m³ which is very close to the metabolic heat source 29000 W/m³. Thus, one may conclude that current injection creates a new heat source and total heat generation is almost doubled by the current application. The temperature increase in a cancerous tissue is calculated as 659 mK that can easily be measured by the modern medical thermal imaging systems.

2.3.3 Total Rate of Heat Transfer from the Breast Surface due to Convection and Radiation

To estimate the heat transfer from the breast surface due to convection and radiation, one can assume a breast model and calculate those terms analytically using equations (2.5) and (2.6). In a previous study, the female breast was simulated with a half sphere which has a 14.4 cm diameter [141]. Assuming the parameters given in Table 2.2, the convection and radiation heat transfer were calculated as 4.68W and 4.73W, respectively [141]. Note that assuming a simpler breast model (a cube of 10x10x10 cm) yields comparable values 4.32 W and 4.36 W, respectively. Using either of these models, one may conclude that the total rate of heat transfer from the breast surface is about 9 W. Since the surface area of the breast is very small, the total heat transfer can be assumed to be very low compared to the metabolic heat generation rate (29000 W/m³), and the additional heat source due to current application (25000 W/m³).

Table 2.2

Model parameters employed for the calculation of the convection and radiation heat transfer using the realistic breast model [141].

Model parameters	Corresponding values
h	6 W/m ² K [140]
A_s	0.0651 m ²
T_s	310 K (Core temperature of the body)
T_∞	298 K (Room (air) temperature)
σ	5.67 x 10 ⁻⁸ W/m ² K ⁴
ε	0.95

2.4 Summary and Discussions

The theory of the thesis study is given in this chapter. The electromagnetic and heat problems are explained in detail. To investigate the effects of heat transfer from the skin surface, the convection and radiation heat transfer is calculated as boundary conditions for both realistic breast model [141] and our 3-D breast model (a cube of 10x10x10 cm). Total heat transfer is obtained as approximately 9W for both models. Due to the small surface area of the female breast, the amount of convection and radiation heat transfer is negligible compared to the external heat source created by the current application (25000 W/m³) and metabolic heat generation of cancerous tissue (29000 W/m³). Then, the feasibility of the electro-thermal problem is implemented analytically by calculating the temperature rise due to the electrical current application. Transient behaviour of the uniform breast tissue is obtained for a uniform current excitation. 659 mK temperature increase which can easily be sensed by modern thermal imagers is acquired in a uniform cancerous tissue. Next, to be able to define the current excitation duration, time constants of different tissues are calculated analytically and optimal current application time is found as approximately 500 sec for the breast tissue.

CHAPTER 3

SIMULATION STUDY

3.1 Introduction

The purpose of this chapter is to assess the feasibility of electro-thermal imaging via two- and three-dimensional numerical simulations. To solve the related electromagnetic and thermodynamic problems the COMSOL Multiphysics engineering simulation software environment is employed [21]. COMSOL is a software package that allows the solution of the corresponding two-dimensional (2-D) and three-dimensional (3-D) problems using the Finite Element Method. In this thesis study, COMSOL is used to model the woman breast with a single and multi-inhomogeneity (the malignant tissue).

3.2 Modeling

A two-dimensional (2D) model of the woman breast is developed using two square regions (Fig. 3.1). The larger square is 100 cm^2 and represents the healthy breast tissue. The area of the smaller square is 1 cm^2 and it represents the malignant tissue. The material properties are assigned as given in Table 3.1. Current is applied to the object by pair of electrodes (20 cm^2) from left and right side boundaries.

For three-dimensional modeling, the woman breast is modeled by two cubes. The larger cube (10 cm x 10 cm x 10 cm) represents the healthy tissue. The malignant tissue is modeled by the smaller cube (0.35 cm x 0.35 cm x 0.35 cm). Current is applied from the right and left side surfaces with circular electrodes (20 cm²) placed at the center of the sides. Excitation currents are kept within the medical safety limits [20].

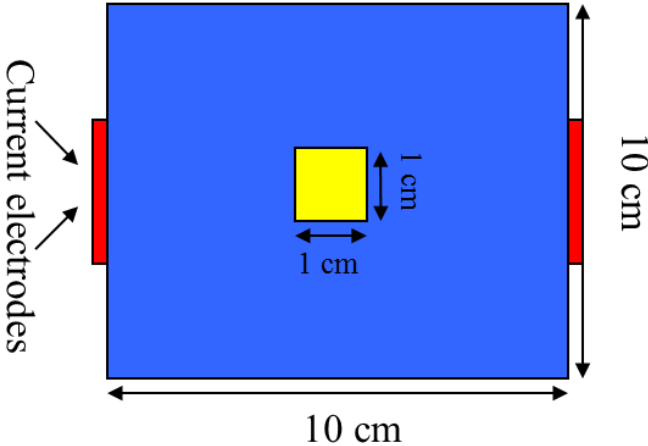


Fig. 3.1 Two-dimensional simulation geometry. Larger square represents the healthy and smaller square represents the cancerous tissue. 5 mA/cm² current at 10 kHz is applied with current electrodes.

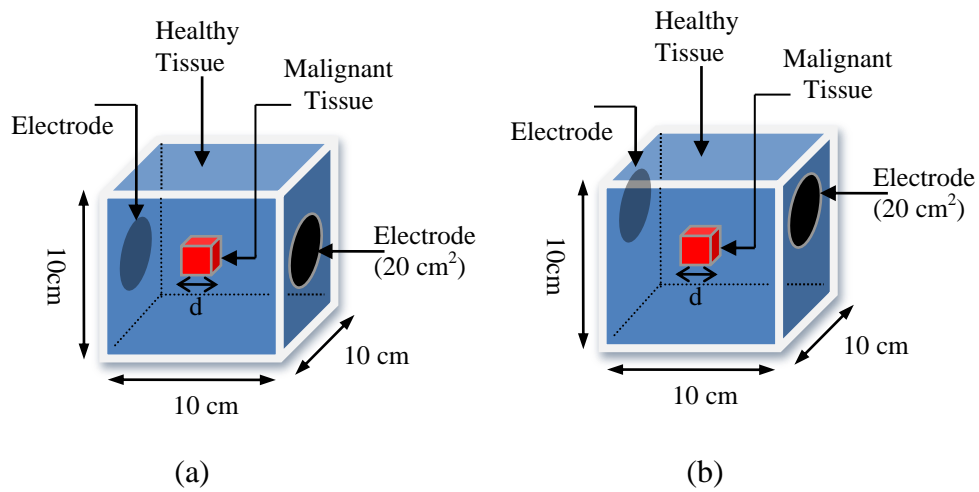


Fig. 3.2 Three-dimensional simulation geometries. The inhomogeneity represents a cubic ($d \times d \times d$) tumor inside the breast. (a) Current electrodes are at the center of the side surfaces. (b) Current electrodes are shifted 2.4 cm (center of the electrode is located 2.6 cm away from the top surface) to the upper surface (camera site).

Table 3.1
Healthy and Malignant Tissue Electrical and Thermal
Characteristics [22], [23], [24], [30]

	Healthy Tissue	Malignant Tissue
ρ (kg/m ³)	920	920
ρ_B (kg/m ³)	1000	1000
C_B (J/kg ^o K)	4200	4200
W_B (1/s)	0.0018	0.009
T_B (°K)	310.15	310.15
Q_{met} (W/m ³)	450	29000
k (W/m ^o K)	0.42	0.42
σ (S/m)	0.0283	0.2804

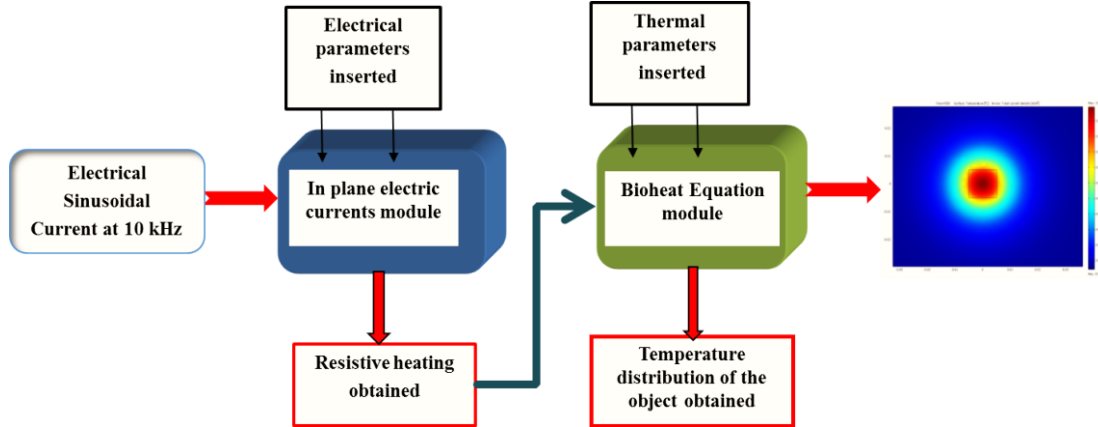


Fig. 3.3 Flowchart of the Electro-Thermal Imaging System. Electrical currents results in resistive heating. In-plane electric currents module calculates this resistive heating and Bio-Heat Equation module calculates the temperature distribution in the body.

3.3 Numerical Analysis

Before the computation stage, all electrical and thermal boundary conditions of the problem (as discussed in chapter 2) are properly assigned. Thereafter, a numerical mesh is generated for the desired model. COMSOL software adjusts the optimal mesh number and size by taking the computation time and the result accuracy into account. To check the accuracy of the results, the number of elements for the same geometry is increased several times and the results with different meshes are compared. The differences in temperatures are observed and the optimal number of elements is obtained. Mesh size is important especially at high frequency studies. Results are obtained by using much denser meshes for higher operation frequencies.

The resistive heat source distribution (as defined by equation (2.9)) that occurs due to applied electrical currents is calculated with the “in plane electric currents module”. This module uses the coupled partial differential equations (equation (2.1)) and boundary conditions (equation (2.2)) to solve the corresponding electromagnetic problem. Next, this distribution is assigned as an input to the “bio- heat equation module” to solve the corresponding thermodynamic problem. Natural convection and radiation heat transfer from the skin surface are also taken into account as the boundary conditions. The rate of convection heat transfer is found in COMSOL as a default heat flux boundary source. Whereas the rate of radiation heat transfer is added in this study. The heat transfer coefficient value for the skin is taken as $6 \text{ W/m}^2\text{K}$ [140]. The spatio-temporal behavior of the temperature distribution is then observed. Figure 3.3 explains the numerical procedure schematically.

3.4 Results

3.4.1 Tumor at different locations

Fig. 3.1 shows the 2D problem geometry used in this part of the study. To reveal the depth dependency (in 2D studies, the term “depth” represents the distance from a selected electrode), the malignant tissue is moved horizontally and simulations are implemented for each position. The temperature distribution is solved twice: 1) in passive mode (no electrical current is applied from the boundary, temperature distribution is determined by the metabolic sources and the blood perfusion), 2) in active mode (in addition to existing metabolic source distribution electrical currents are applied from the boundary). In active mode, 5 mA sinusoidal (10 kHz) current is applied for 400 sec. For both cases, the contrast $\Delta T = T_{\max} - T_b$ between the maximum

temperature T_{\max} (at the tumor location) and average background temperature T_b are calculated.

Fig. 3.4 shows the temperature distribution in the passive mode when the tumor is at the center. A temperature contrast of $0.441\text{ }^{\circ}\text{C}$ is obtained at the tumor location relative to background temperature due to the metabolic heat generation and blood perfusion. In active mode (Fig. 3.5), the temperature at the same point is increased up to $179\text{ }^{\circ}\text{mC}$ and a contrast of $558\text{ }^{\circ}\text{mC}$ is obtained. It is observed that, the temperature contrast is improved by $117\text{ }^{\circ}\text{mC}$ (26.5 %) in the active mode. Note that, this is the improvement when the malignant tissue is at the distant point from the current electrodes. The performance of the technique should also be investigated when the malignant tissue is closer to the electrodes. To observe this behavior a second simulation is performed with an eccentric tumor.

The malignant tissue of the same size is located 1 cm away from the left side electrode. Fig. 3.6 shows the temperature distribution in the passive mode. In the active mode (Fig. 3.7), the temperature at the tumor location increases by $607\text{ }^{\circ}\text{mC}$ compared to the passive mode. In this case, the temperature contrast is increased by $384\text{ }^{\circ}\text{mC}$ (85 %) relative to the passive mode.

It is observed that active mode increases the temperature contrast at the tumor site in the thermal images. However, it also causes noticeable artifacts nearby the electrodes due to higher electrical current density (and higher resistive heating). To eliminate these artifacts (*electrode artifacts*) the additional heat source due to applied currents can be analyzed for the same body geometry and thermal images in the active mode can be weighted accordingly. One way to implement this approach is to divide each active mode image with a *reference* active mode image obtained for a uniform body (i.e., uniform electrical properties, uniform metabolic sources). Since in both images the artifacts are almost same, those artifacts can be eliminated in a large extent in the

resultant image. Another approach would be to apply *difference operation* between those active mode images. In the following sections of this study, the results obtained with the latter technique are presented.

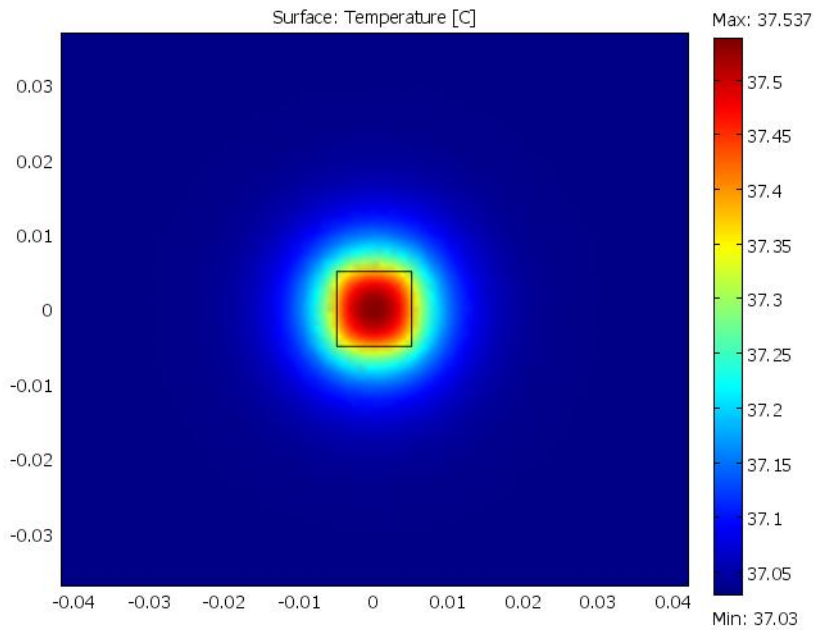


Fig. 3.4 Temperature distribution for the centric tumor case in passive mode.

$T_{\max} = 37.537 \text{ }^{\circ}\text{C}$, $T_b = 37.096 \text{ }^{\circ}\text{C}$ and $\Delta T = 441 \text{ }^{\circ}\text{mC}$.

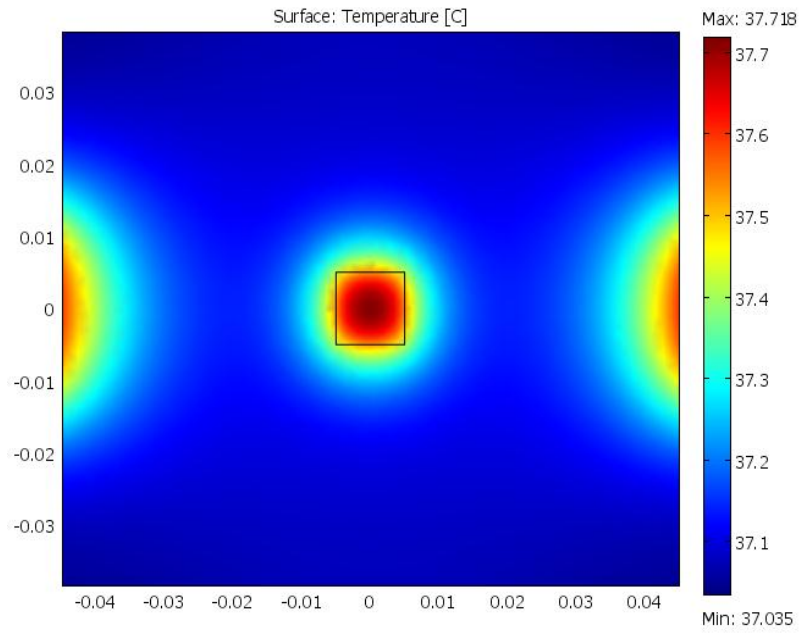


Fig. 3.5 Temperature distribution for the centric tumor case in active mode.
 $T_{\max}=37.716\text{ }^{\circ}\text{C}$, $T_b = 37.158\text{ }^{\circ}\text{C}$ and $\Delta T = 558\text{ mC}$.

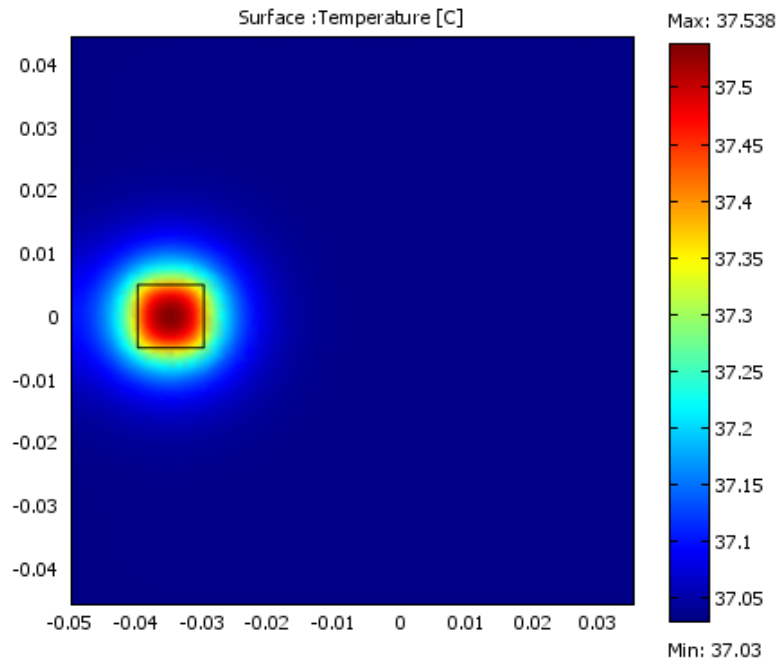


Fig. 3.6 Temperature distribution for the eccentric tumor case in passive mode. $T_{\max}= 37.537\text{ }^{\circ}\text{C}$, $T_b = 37.085\text{ }^{\circ}\text{C}$ and $\Delta T = 452\text{ mC}$.

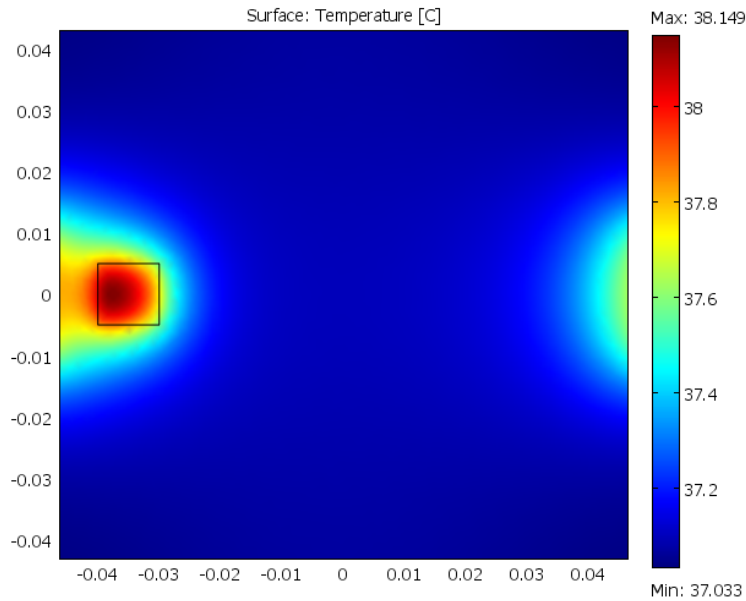


Fig. 3.7 Temperature distribution for the eccentric tumor case in active mode. $T_{\max} = 38.144 \text{ }^{\circ}\text{C}$, $T_b = 37.308 \text{ }^{\circ}\text{C}$, $\Delta T = 836 \text{ }^{\circ}\text{mC}$.

3.4.2 Responses at Different Operation Frequencies:

To investigate the effects of the operation frequency, the temperature distributions in active mode are calculated for different frequencies. For each operation frequency, a centric tumor is assumed (as given in Fig. 3.1) and a reference active mode image is obtained for a uniform body. Difference images are calculated to remove the electrode artifacts. Fig. 3.8 shows the difference image at the operation frequency of 10 kHz. The electrodes artifacts (as shown in Fig. 3.5) are not totally removed but decreases to a large extent. Fig. 3.9 and Fig 3.10 show the difference image at 80 MHz. It is observed that increasing the operation frequency reduces the electrode artifacts. However, the main reason of this reduction in artifacts (and other possible effects on the images) must be studied separately.

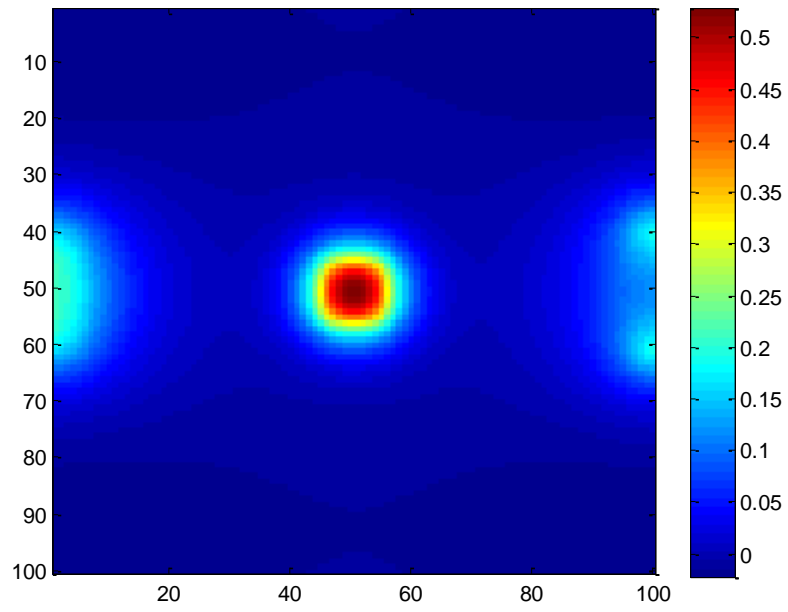


Fig. 3.8 Difference of the two active mode images at 10 kHz, $\Delta T_{\max} = 520 \text{ }^\circ\text{mC}$.

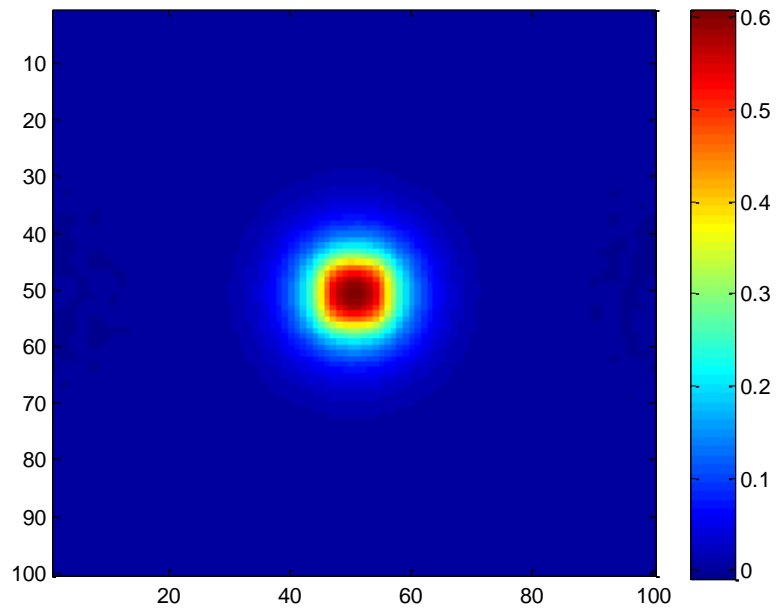


Fig. 3.9 Difference of the two active mode images at 80 MHz, $\Delta T_{\max} = 550 \text{ }^\circ\text{mC}$.

Note that, to improve the accuracy in results, the number of elements in the numerical model is increased at high frequency studies. The optimal mesh is determined when the difference in solutions becomes insignificant (1-3 mK). For 2D studies, the number element is 994 at 10 kHz and 3976 at 80 MHz.

3.4.3 Transient Response:

To determine the appropriate excitation duration in active mode two simulations are performed using the Transient Mode of COMSOL. The temporal behavior of the temperature distributions is observed. In the first simulation, the body geometry is as given in Fig. 3.1 and 5 mA (10 kHz) current is applied. The temperature of the malignant tissue as a function of time is shown in Fig. 3.10. In the second simulation, the malignant tissue is at 0.1 cm from the left electrode. Fig. 3.11 shows the transient behavior of the temperature at the malignant tissue.

Since the tumor size is small, one may assume a uniform current density on the malignant tissue and expect an exponential rise in temperature as studied in Chapter 2. Fig. 3.10 and 3.11 show the expected behavior. Note that the time constant ($T_c = 123$ sec) given in Table 2.1 can be used to estimate this behavior. In approximately $4T_c$ the temperature at the malignant tissue saturates.

In a third simulation, the transient behavior is studied using a 3D model (3.2(a)). Sinusoidal current ($5\text{mA}/\text{cm}^2$) is applied at 10 kHz. The malignant tissue is $3.5 \times 3.5 \times 3.5$ mm and it is located in the center of the breast. The exponential rise in the temperature of the malignant tissue is shown in Fig. 3.12.

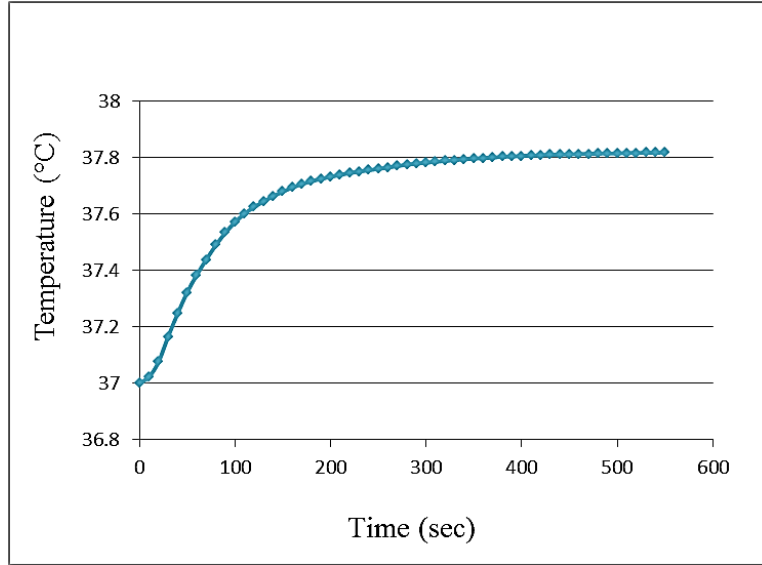


Fig. 3.10 Transient analysis. 2D model (Fig. 3.1) is used in active mode ($i=5\text{mA}$ at 10 kHz). Transient response of the temperature at the malignant tissue is shown.

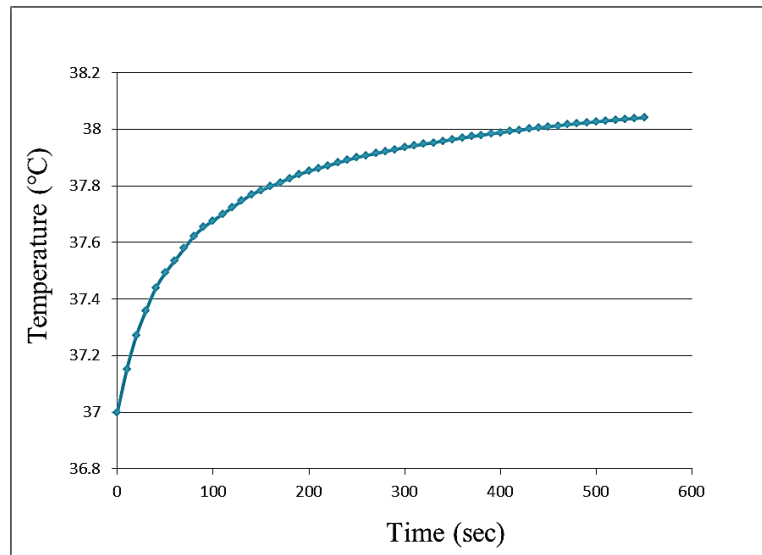


Fig. 3.11 Transient analysis. 2D model is used in active mode ($i =5\text{mA}$ at 10 kHz). The malignant tissue is located 1 cm from the left electrode. Transient response of the temperature at the malignant tissue is shown.

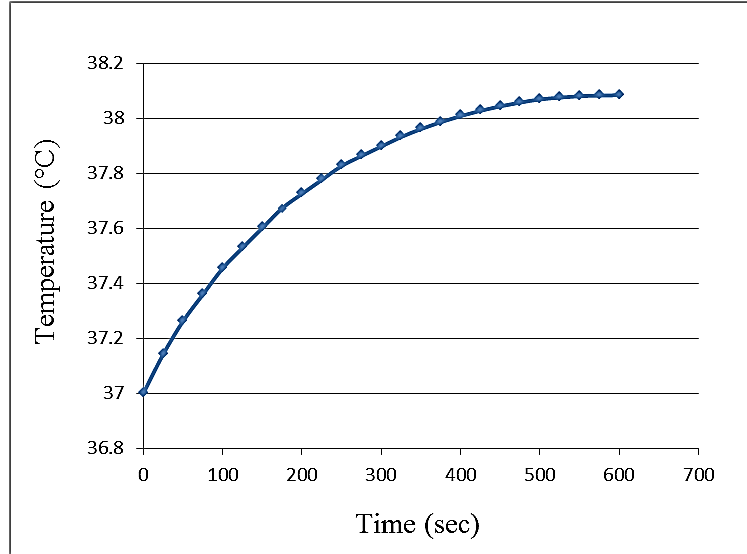


Fig. 3.12 Transient analysis. 3D model (Fig. 3.2(a)) is used in active mode ($5\text{mA}/\text{cm}^2$ at 10 kHz). Transient response of the temperature at the malignant tissue is shown.

3.4.4 Temperature Increases due to Malignant Tissue at Different Depths: 3D studies

Fig. 3.2(b) shows the 3D problem geometry used in this part. Since the thermal camera is assumed to be over the top surface of the body the current electrodes are shifted upwards. To reveal the depth dependency, the malignant tissue (42.8 mm^3 , $d=3.5\text{ mm}$ side length) is moved vertically between 1 cm and 9 cm, and simulations are implemented for each position. The temperature distribution is again solved twice, i.e., in passive and active modes. In active mode, 5 mA sinusoidal (10 kHz) current is applied for 400 sec. For both cases, the contrast $\Delta T=T_{\text{max}}-T_b$ between the maximum temperature T_{max} (at the tumor location) and average background temperature T_b are calculated.

Figure 3.13 shows the temperature of the malignant tissue for various depths in active mode. The temperature of the malignant tissue increases more than 20 °mC due to resistive heating even if it is located at 8 cm depth. The temperature increases as the malignant tissue gets closer to the top surface (and current electrodes). Similar behavior is also observed when the contrast difference is calculated between active and passive modes (Table 3.2). When the image contrast is considered on the tumor plane, up to 19.9 % improvement can be obtained relative to the passive mode when the tumor is located 1 cm from the top surface.

Note that only the temperature on the breast surface (the top surface of the cube) can be measured using thermal imagers. Consequently, as long as temperature contrast increases with current application, the effects of different tumor locations on the top surface temperature distribution should be investigated in active mode. The surface temperature values obtained for the preceding simulations show that tumors located more than 1 cm depth do not result in measurable temperature changes on the top surface. To determine the specific depth that generates measurable changes (i.e., more than 20 °mC) simulations are implemented using tumor location changes in millimeter scale (i.e., the tumor is moved vertically between 1 mm and 10 mm). Fig. 3.14 shows the temperature contrast obtained on the top surface of the breast model. It is observed that, a 3.4 mm³ tumor located at 9 mm depth can be sensed by modern imagers in active mode. Note that this is not possible if the same imagers are used in passive mode. If electrical currents are not applied, a tumor of that size can only be sensed when the tumor is at 3 mm. The contrast differences between the active and passive modes on the top surface due to different tumor locations are presented in Table 3.3.

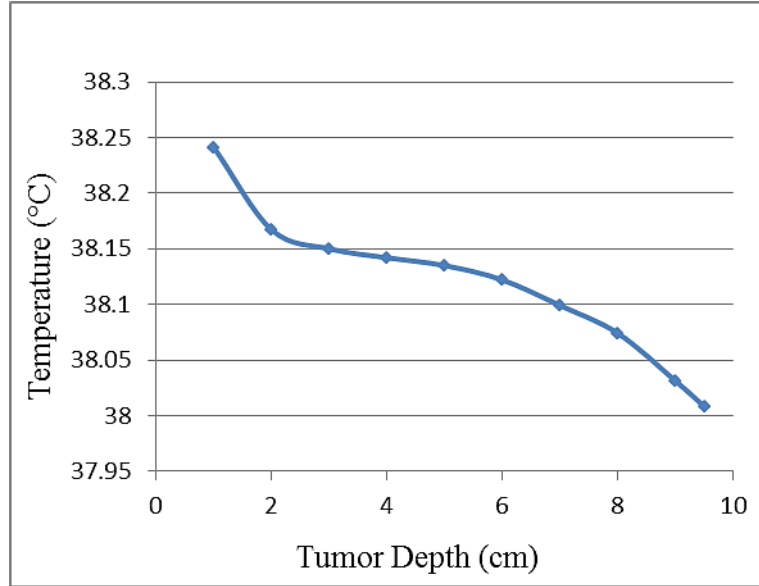


Fig. 3.13 Tumor temperature versus tumor depth in active mode (5 mA/cm² at 10 kHz). 3D Model (Fig 3.2(b)).

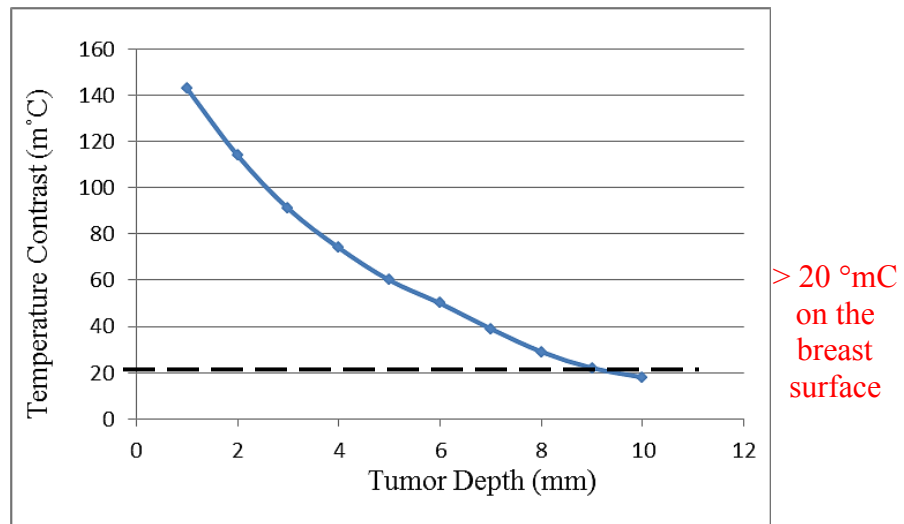


Fig. 3.14 The temperature contrast on the top surface of the breast model for different tumor locations (5 mA/cm² at 10 kHz). 3D Model (Fig 3.2(b)).

Table 3.2

Tumor Temperatures for different tumor locations and performance improvements due to active mode of operation

Tumor Depth (cm)	Temperature (°C)	Contrast Difference (°mC)	Performance improvement (%)
1	38.241	174	19.9
2	38.167	136	16.2
3	38.150	115	12.9
4	38.142	91	9.9
5	38.135	63	7.1
6	38.122	40	4.5
7	38.086	27	3
8	38.074	20	2.2
9	38.031	13	1.6

Table 3.3

Top surface temperatures for different tumor depths and contrast differences due to active mode of operation

Tumor Depth (mm)	Temperature (°C)	Contrast Difference (°mC)
1	37.196	103
2	37.178	84
3	37.166	71
4	37.151	60
5	37.140	50
6	37.128	41
7	37.112	32
8	37.091	25
9	37.078	20
10	37.071	17

3.4.5 Tumor Temperature Changes for Different Current Density Values

Fig. 3.2(a) shows the 3D problem geometry used in this part. The tumor (3.375 mm^3 , $d=1.5 \text{ mm}$ side length) is located halfway between the two electrodes at 5 cm depth. The current density is altered between 0 to 15 mA/cm^2 at 10 kHz. For each case, the temperature of the tumor is recorded after 400 sec. The behavior of the malignant tissue temperature due to changes in applied current density is as shown in Fig. 3.15.

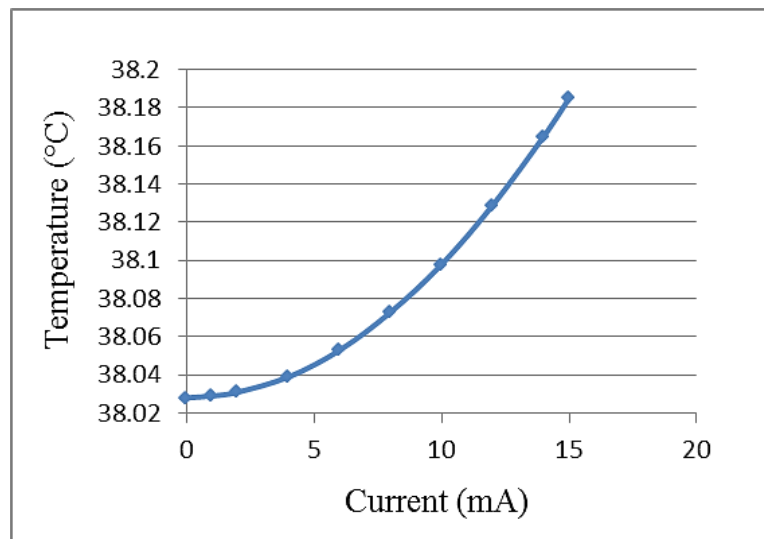


Fig. 3.15 Tumor temperature versus current density plot.

3.4.6 Temperature Increases for Different Dimensions of Tumor

Fig. 3.2(a) shows the 3D problem geometry used in this study. Simulations are implemented in active and passive mode by changing the volume of the malignant tissue. Simulation results show that larger tumors exhibit higher temperatures (Fig.

3.16). When the dimension of the tumor increases, the performance increases and higher temperature contrasts are achieved to detect the breast carcinoma.

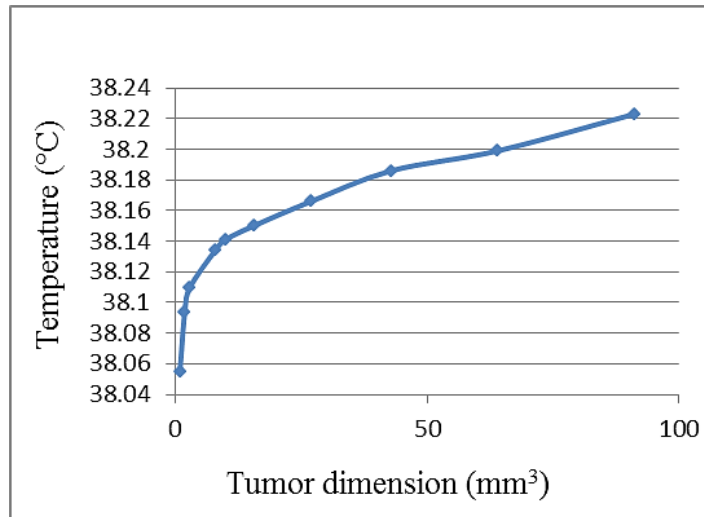


Fig. 3.16 Tumor temperature versus tumor volume. 3D Model (Fig. 3.2(a)).

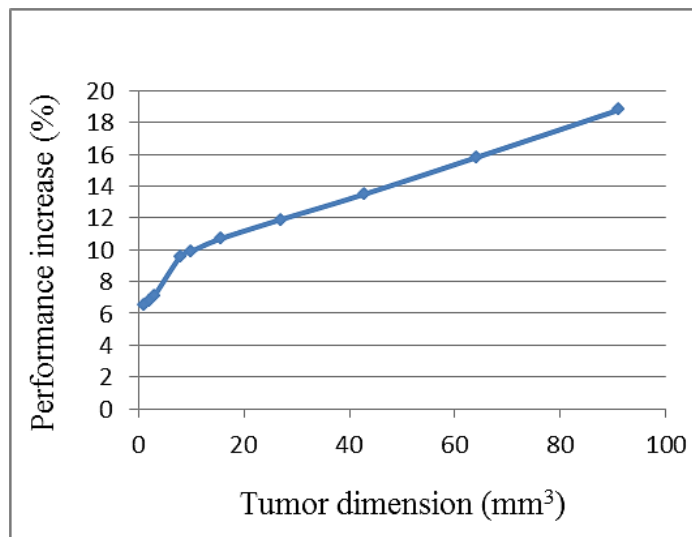


Fig. 3.17 Performance increase versus tumor dimension. Current injection improves the contrast between the healthy and the cancerous tissue. 3D Model (Fig. 3.2(a)).

3.4.7 Temperature Changes on the Breast Surface due to Different Operation Frequencies

Fig. 3.2(b) shows the problem geometry of this simulation study. The tumor is 42.8 mm^3 and located at 1.5 cm depth in the healthy breast tissue. Figure 3.19 shows the temperature distribution on the breast surface in passive mode. Although the tumor is distinguished numerically, it cannot be sensed using today's thermal infrared imagers since the temperature contrast is approximately $2 \text{ }^\circ\text{mC}$.

In active mode of operation, however, the temperature contrast can be improved by increasing the operation frequency. Since, electrical conductivity and permittivity changes with frequency, different temperature distributions and correspondingly different temperature contrasts can be obtained for the same object by changing the operation frequency.

In this study, 5 mA/cm^2 current is applied at various frequencies. The temperature distribution of the breast tissue is obtained on the top surface of the breast model. Firstly, temperature distribution of homogeneous breast tissue is calculated. Then, the temperature distribution is obtained when there is also tumor. The difference of the two temperature distributions is calculated and shown for each operation frequency. Fig. 3.20 shows the temperature distribution when the operation frequency is 10 kHz. In this image, the cancerous tissue starts to appear when it is compared with the passive mode (Fig. 3.19). The temperature difference generated by the tumor is approximately $20 \text{ }^\circ\text{mC}$. When the operation frequency is increased, the best contrast is obtained at 800 MHz. Almost $60 \text{ }^\circ\text{mC}$ temperature difference (contrast) occurred at the center due to the malignant tissue at 800 MHz frequency.

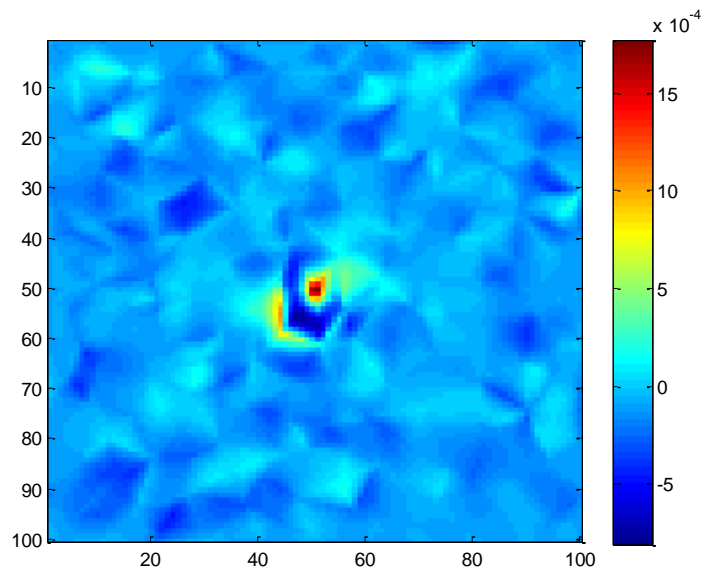


Fig. 3.18 Temperature distribution on the top surface of the breast model in passive mode. The malignant tissue (42.8 mm^3) is at 1.5 cm depth from the surface. Color bar indicates the temperature difference ($^{\circ}\text{C}$).

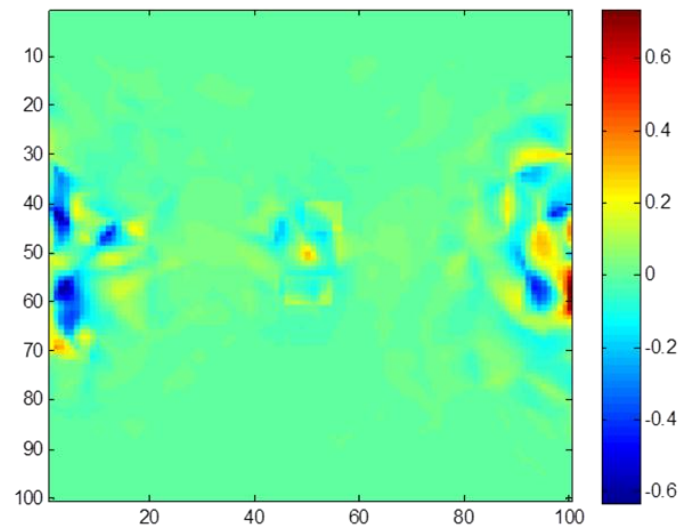


Fig. 3.19 Temperature distribution on the top surface of the breast model in active mode (5 mA/cm^2 at 10 kHz). The malignant tissue (42.8 mm^3) is at 1.5 cm depth from the surface. Color bar indicates the temperature difference ($^{\circ}\text{C}$).

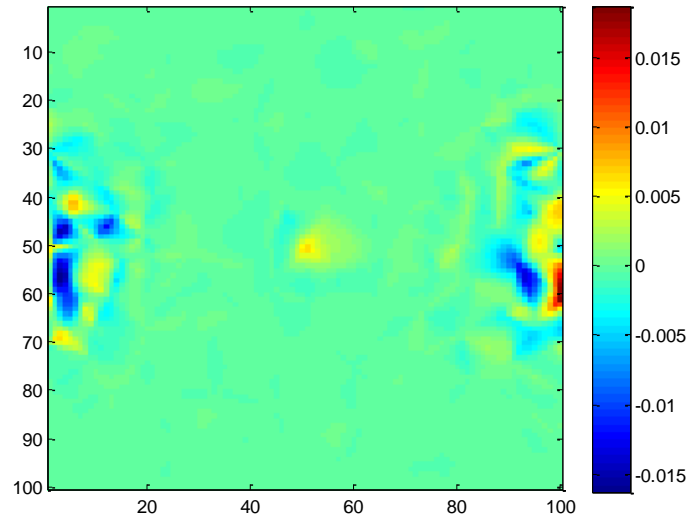


Fig. 3.20 Temperature distribution on the top surface of the breast model in active mode (5 mA/cm^2 at 100 kHz). The malignant tissue (42.8 mm^3) is at 1.5 cm depth from the surface. Color bar indicates the temperature difference ($^{\circ}\text{C}$).

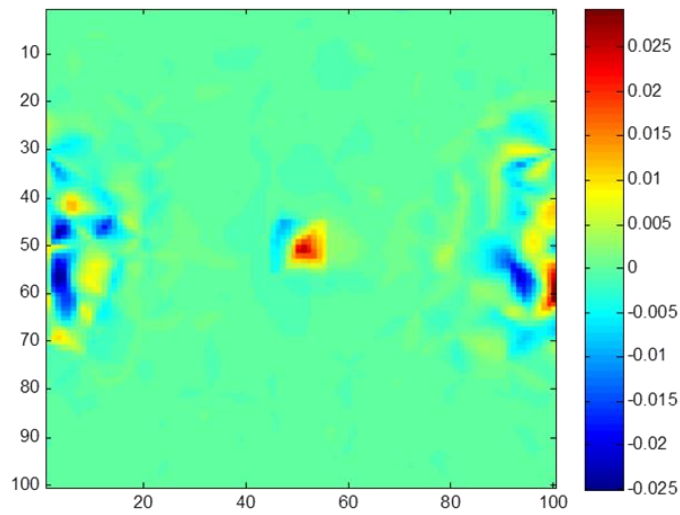


Fig. 3.21 Temperature distribution on the top surface of the breast model in active mode (5 mA/cm^2 at 10 MHz). The malignant tissue (42.8 mm^3) is at 1.5 cm depth from the surface. Color bar indicates the temperature difference ($^{\circ}\text{C}$).

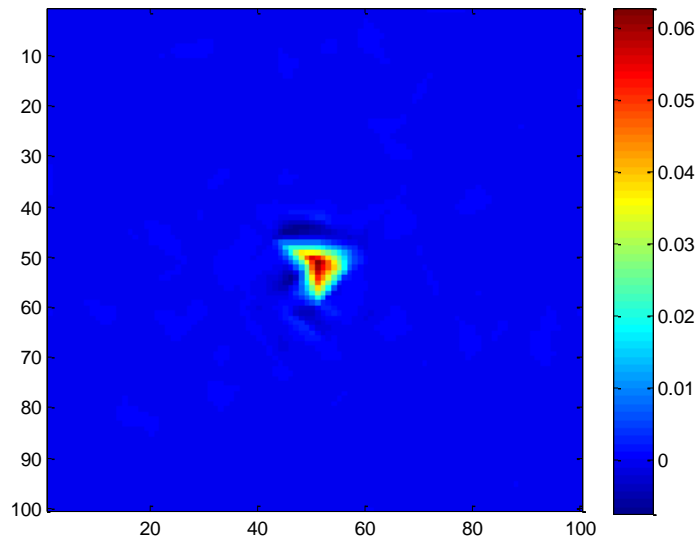


Fig. 3.22 Temperature distribution on the top surface of the breast model in active mode (5 mA/cm^2 at 800 MHz). The malignant tissue (42.8 mm^3) is at 1.5 cm depth from the surface. Color bar indicates the temperature difference ($^{\circ}\text{C}$).

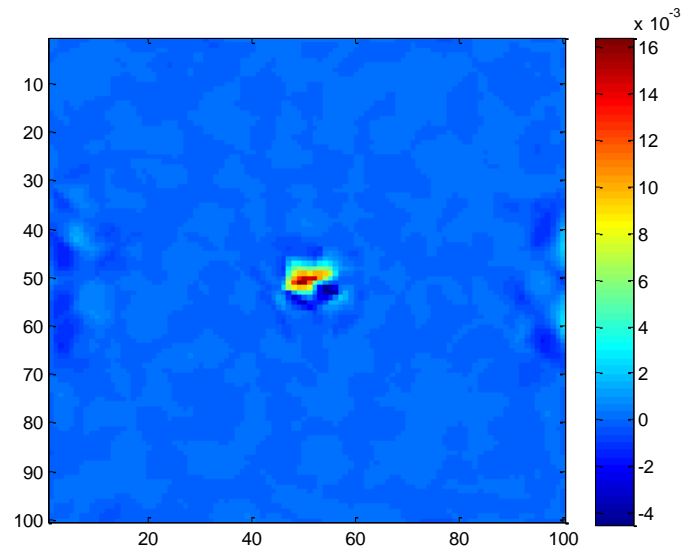


Fig. 3.23 Temperature Distribution on the top surface of the breast model in active mode (5 mA/cm^2 at 800 MHz). ($1.5 \times 1.5 \times 1.5 \text{ mm} = 3.4 \text{ mm}^3$) tumor is detected from 9 mm depth). Color bar indicates the temperature difference ($^{\circ}\text{C}$).

Since tumor growth acceleration starts at 2 or 3 mm, critical breast cancer tumor size for breast cancer screening is 2 mm [144]. Therefore, in the simulation study, tumor size is specifically selected as 1.5 and 3.5 mm and the corresponding tumor dimensions are 3.4 mm^3 and 42.8 mm^3 . Fig. 3.24 shows the temperature distribution on the breast surface when the 3.4 mm^3 tumor is placed at 9 mm depth.

3.4.8 Temperature Increases of Poly Cancerous Tissues on the Breast Surface

In this part of the study, the effects of poly tumors are investigated. Poly tumors (3.4 mm^3 at 9 mm depth) like single tumor can also be detected in active mode.

Fig. 3.25 shows the temperature difference image (relative to uniform body) on the top surface of the breast model when two 3.4 mm^3 tumors are placed at 9 mm depth. The distance between the tumors is 2 cm. In the passive mode, almost $10 \text{ }^\circ\text{mC}$ temperature contrast occurs and this cannot be sensed with the state of the art thermal imagers. On the other hand, in active mode (5 mA/cm^2 at 100 kHz), the tumors produce almost $20 \text{ }^\circ\text{mC}$ temperature contrasts on the breast surface (Fig. 3.26). This result is also verified analytically in the second chapter. Current within medical safety limits causes almost 25000 W/m^3 external heat generation. The metabolic heat generation value for cancerous tissue is 29000 W/m^3 . Therefore, current application generates an external heat source which is almost equal to the metabolic heat source and this doubles the temperature increase due to breast carcinoma. However, at this operation frequency, there are noticeable electrode artifacts. An increase in frequency (800 MHz) produces a better image, i.e., contrast is preserved while artifacts are removed. Multi-frequency study gives an opportunity to obtain more than one images for the same breast tissue and can provide more detailed information about the breast tissue.

As a final simulation, four identical malignant tissues (3.4 mm^3) are placed at 9 mm depth. Each of these malignant tissues is located at the corner of a square which has a side length of 2 cm. In active mode (800 MHz), tumors can be clearly seen in the difference image (Fig. 3.27).

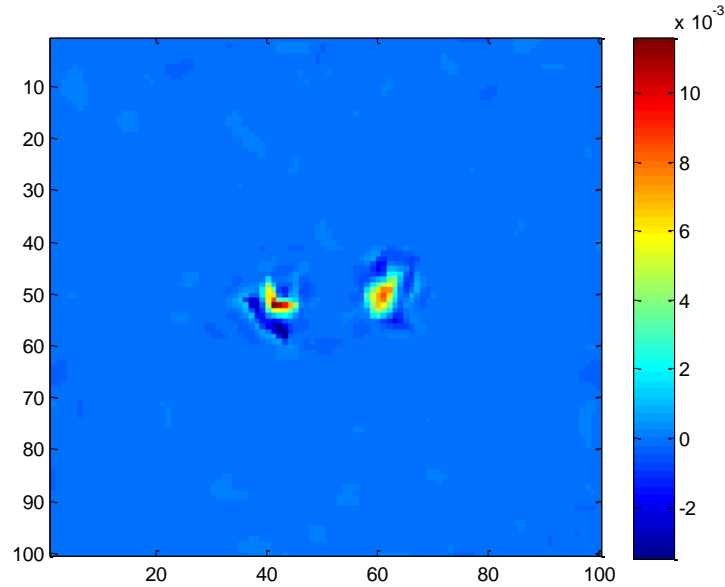


Fig. 3.24 Difference image of the Tumor Tissues (3.4 mm^3) and healthy breast tissue on the breast surface in passive mode (Temperature increases occur just due to the metabolic heat generation and blood perfusion of the tissue). Color bar indicates the temperature difference ($^{\circ}\text{C}$).

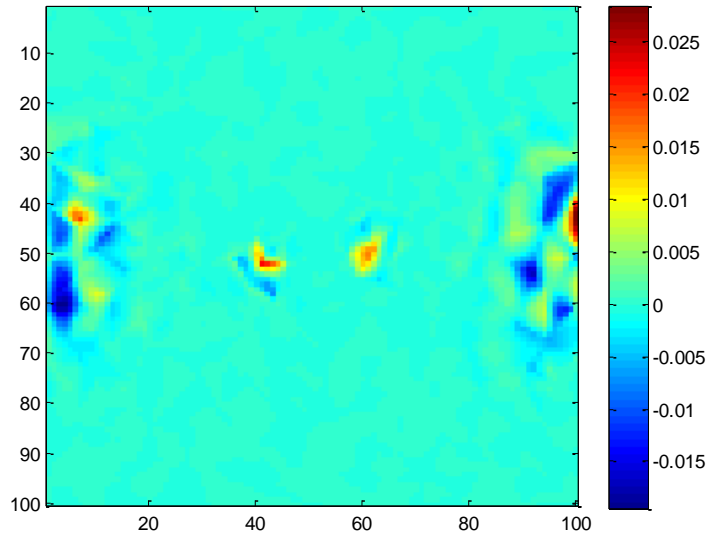


Fig. 3.25 Difference image on the top surface of the breast model in active mode (5 mA/cm² at 100 kHz). Dual 3.4 mm³ tumors are detected from 9 mm depth. Color bar indicates the temperature difference (°C).

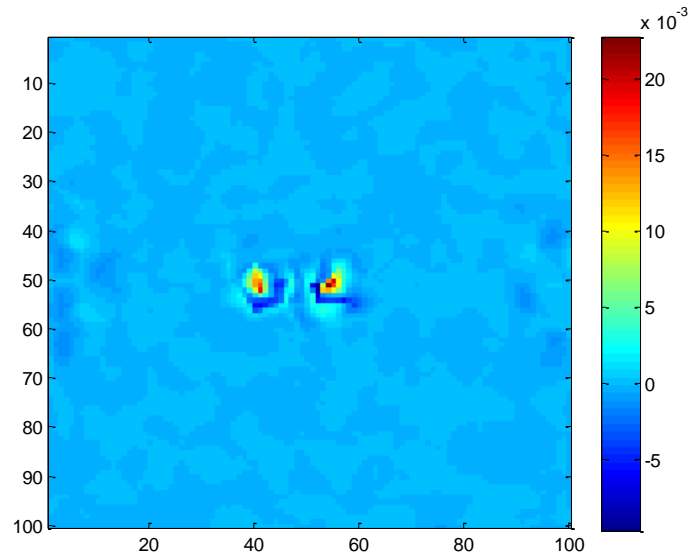


Fig. 3.26 Difference image on the top surface of the breast model in active mode (5 mA/cm² at 800 MHz). Dual 3.4 mm³ tumors are detected from 9 mm depth. Color bar indicates the temperature difference (°C).

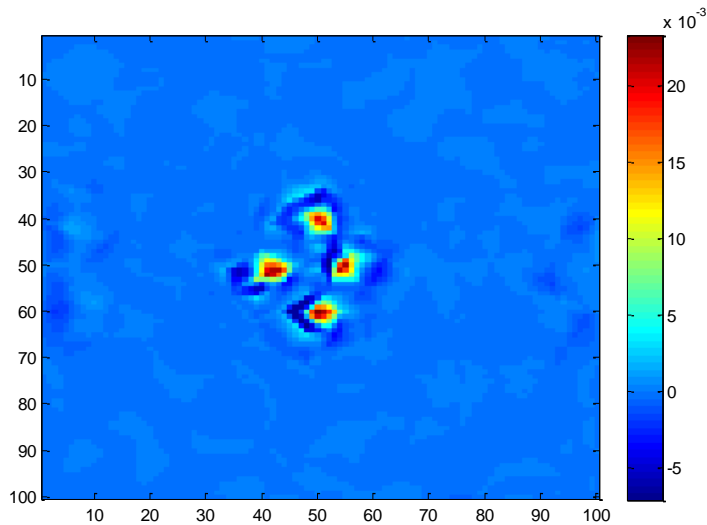


Fig. 3.27 Difference image of the Tumor Tissues and healthy breast tissue on the breast surface when there is a 5 mA current stimulation at 800 MHz (4 identical tumors which have 3.4 mm^3 dimensions are detected from 9 mm depth). Color bar indicates the temperature difference ($^{\circ}\text{C}$).

3.5 Summary and Discussions

To implement the feasibility of electro-thermal imaging and observe the effects of electrical current application on temperature contrasts, firstly, a model of the female breast tissue which represents the realistic tissue properties (electrical and thermal properties) should be developed. In the literature, a female breast is simulated with a half sphere which has a 14.4 cm diameter [141]. The volume of our cubic model (10x10x10 cm) is designed to be closer to the realistic breast model (785 cm^3).

The imaging performance of the thermal camera is based on the thermal sensitivity of the device. It mainly depends on the noise equivalent temperature difference (NETD),

focal length ratio, integration time, dynamic range and number of pixel (pixel area). NETD is the ability of the measurement system to separate small signals in noise. The f number of the lens (focal length/lens diameter ratio) impacts the thermal sensitivity by the square of the f number value (an $f/2.0$ optic corresponds to 4x reduction in thermal sensitivity). Shorter integration time (at the same NETD) causes less blurring in the image. It is especially important when imaging mobile and low energy objects. Pixel resolution is also another critical parameter affecting the sensitivity of the camera and correspondingly image quality. The parameters that affect the thermal sensitivity can show differences according to the infrared cameras and experimental conditions. Since, the best current state of the art thermal imagers have approximately 17 mK NETD values, $\Delta T=20$ mK temperature difference is taken as a contrast threshold for the tumor detection. The other parameters of the measurement system are assumed as ideal (not decreasing the thermal sensitivity) in determining the contrast threshold.

In this chapter, feasibility study of the electro-thermal imaging with two- and three-dimensional realistic model of a healthy (a cube of 10x10x10 cm) and a cancerous tissue is implemented with numerical simulations. Comsol Multiphysics Modeling and Matlab Programs are used in the solution of the electromagnetic and thermal problems.

Since, the object of the study is to improve the contrast of the thermal imaging; an additional heat source is created by applying currents within medical safety limits. Firstly, temperature distributions are imaged for 2-D model in passive and active mode of operations. In active mode, temperature contrast is increased 117 °mC which corresponds to 26.5 % improvement in the performance compared to the passive mode of operation (cancerous tissue is located at the center). The increase of the temperature contrast becomes 384 °mC (85 % improvement in the performance) when the malignant tissue is located 1 cm away from the left side electrode. Higher

current density causes higher temperature increase in the tumor tissue. Next, to be able to mimic more realistic case, simulations are implemented with the realistic 3-D model. Since the growth of breast malignancy begins at 2 to 3 mm, the critical tumor size in breast cancer detection is in between 2 and 3 mm [144]. Therefore, in simulations, the sizes of cancerous tissue are particularly chosen as 1.5 (a dimension of 3.4 mm^3) and 3.5 mm (a dimension of 42.8 mm^3). To observe the change in temperature that the cancerous tissue creates (at the tumor region), the temperature of the malignant tissue at various depths is calculated in active mode of operation. The tumor generates more than $20 \text{ }^\circ\text{mC}$ temperature increase due to the resistive heating at 8 cm depth. This value increases when the tumor tissue gets closer to the top surface (electrodes are located at the right and left side boundaries and 1 mm away from the top surface). Contrast differences in between passive and active modes also show the similar behavior. Consequently, whenever breast malignancy located closer to the surface, more temperature increases and contrasts occur on the skin surface and can be detected more easily.

Since the infrared camera can measure thermal radiations only from the surface of objects, the effects of different tumor locations should be investigated on the top surface temperature distribution. Measurable temperature difference with an infrared camera is assumed as $20 \text{ }^\circ\text{mC}$ for this simulation step. Since 3.4 mm^3 malignant tissue at 1 cm depth does not create temperature increase more than $20 \text{ }^\circ\text{mC}$ on the breast surface, simulations are implemented in millimeter scale by changing the tumor depth in between 1 mm and 10 mm (1 cm). In passive mode, tumor can only be sensed at 3 mm depth. On the other hand, malignant tissue can be detected at 9 mm depth in active mode of operation by the current state of the art thermal cameras.

Although current application increases the temperature contrast at the tumor location, it also leads to electrode artifacts nearby the electrodes due to higher resistive heating (higher electrical current density). Two different approaches can be applied to remove

these undesired artifacts. First one is dividing each active mode temperature distribution with a reference uniform body active mode image. Both images have approximately same artifacts. Therefore, these artifacts are almost removed in the resultant image. Second approach is taking the differences of those active mode temperature distributions. Also in this way, electrode artifacts are eliminated in a large extent.

In the simulation study, the parameters that affect the temperature contrast due to the tumor tissue are investigated. These are amplitude, duration, and frequency of the applied current, and dimension and location (depth) of the malignancy. Although temperature contrast increases by raising the strength of the excitation current, medical safety limits restrict the stimulation current for clinical applications. Therefore, current density can be raised in the range of safety limits. Optimal current excitation duration is determined with the transient analysis study. The temporal behavior of the temperature distributions are obtained for both two- and three-dimensional models in the active mode. The optimal duration for the current excitation is found as almost 500 sec which is consistent with the result of analytical study. Another critical parameter that affects the temperature contrast is the tumor dimension. When the dimension of tumor enlarges, injected current density to the breast carcinoma (higher resistive heating in the tumor) increases, and hence, higher temperature contrasts occur.

Electrical conductivity and permittivity of the body tissue alter with the frequency of the electrical current. Therefore, different temperature distributions of the breast tissue can be obtained for the same object by changing the operation frequency of the excitation current. In multi-frequency study, active mode images are acquired for the homogeneous and inhomogeneous (including malignant tissue) breast tissue. Difference operation is applied between those active mode images and temperature distributions are calculated for each operation frequency (10 kHz-800 MHz). The aim

of this multi-frequency study is getting different temperature distributions for the same object and providing more detailed information to make a diagnosis. Higher temperature contrasts are obtained at increasing operation frequencies, and the best temperature contrast for the tumor tissue is obtained at 800 MHz. Nevertheless, further study is required for the multi-frequency study.

In the last part of the simulation study, the temperature contrasts due to multi-tumors are observed. In active mode of operation, tumors at different dimensions and located eccentrically can be detected without losing the image resolution. Each of the tumor tissue can be clearly seen in the difference images even if they are located close to each other. 3.4 mm³ tumors at 9 mm depth created more than 20 °mC temperature contrast on the top surface. Larger tumor among the multi-tumors creates more temperature contrast on the breast surface compared to the smaller tumors.

CHAPTER 4

EXPERIMENTAL STUDY

The aim of this chapter is to show, experimentally, the contribution of active mode on the temperature contrast of medical infrared cameras. To conduct the experiments, mainly three components are required: 1) breast tissue phantoms, 2) a current drive circuit, and 3) an infrared camera. For this purpose, an AC current source is designed and implemented that operates for operation frequencies less than 50 kHz. Biological agar phantoms are developed which has electrically and thermally similar characteristics with the female breast tissue. For imaging purposes, two different thermal infrared cameras are used, namely, an uncooled microbolometer and a cooled Quantum Well Infrared Photodetector (QWIP) long wave infrared cameras. In this chapter, first the implemented current generator is introduced. Thereafter, the properties of the biological agar phantoms developed for the experimental studies are provided. Finally, the results of the experimental studies performed using two different infrared cameras are presented.

4.1 Current Generator

Current conveyors with current injection electrodes are the main parts of an electrical impedance imaging system [13]. The most crucial point in the current injection process is the accuracy in current generation and measurement of the injected current.

A bipolar (floating source) circuit which involves current conveyors can give greater than 12 mA output current (10 kHz-1MHz) without saturation for the adopted body impedance range [13]. However, the injected current should be precisely known to calculate the body impedance exactly. The non-ideal characteristics of the current injection electrodes, the finite output impedance of a floating source, undesired coupling to signal ground and skin-electrode impedance are other error sources that limit this precision.

In some systems, current sense controlled voltage sources (CSVs) are used since this eliminates the requirement for the high impedance current sources. In such systems, the current flow through the system can be precisely sensed [13]. For the same purpose, Schneider proposed the use of a current conveyor as a CSV [13].

There are two current conveyors commercially available, namely, AD844 (Analog Devices, Monolithic Op Amp) and the Burr Brown OPA660 (operational transconductance amplifier) [13]. AD844 can be used as CSV; however, it has some drawbacks. For a ± 12 mA output, the input voltage swing must be between ± 3.6 V to ± 7.2 V for load impedances between 300 and 600 Ω . When AD844 and OPA660 are used as a CSV, the injected current is affected from the body impedance. On the other hand, if voltage-controlled current sources (VCCS) are employed, the current injected to the load is constant regardless of the body impedance.

Literature survey shows that OPA660 provides the highest output current with lower power consumption [13]. Although many circuit setups were simulated using each of devices, circuit optimization was only implemented for OPA660. For a bipolar configuration OPA660 has an output current of ± 13 mA for a load range of 300-600 Ω at its maximum supply voltage of ± 6 V. On the other hand, for higher impedances (up to 1500 Ω), an output current ± 7 mA can be achieved [13].

Consequently, OPA452T (equivalence of OPA660) is preferred in our current generator circuit design.

4.1.1 Operation of the Current Driver Circuit

Current generators are usually used to inject current into the object to be imaged because their high output impedance makes them less sensitive to load impedance. The reason of using VCCS as a current driver is that they are less sensitive to the errors due to the unknown electrode contact impedances provided these impedances are low with respect to the current driver's output impedance and voltmeter's input impedance [26].

In this study, a voltage-to-current-converter (V/I) is used to supply constant current to a load independent of the load specifications (Fig. 4.1). The voltage at the input of the V/I converter is adjusted using an arbitrary waveform signal generator. Three OPA452 T (power operational amplifier (opamp)) are used in the V/I converter. Z_L and I_L are the load impedance and load current, respectively. Our goal is to have constant I_L for a given V_{in} independent of Z_L . The load current I_L is also the current passing through the variable resistors, R_{pot1} and R_{pot2} . If the voltage across R_{pot} ($R_{pot1} + R_{pot2}$) can be kept constant, I_L will also be constant. However, any changes at the load voltage is reflected to the output of the second operational amplifier (as labeled in Fig. 4.1) with the feedback loop formed using opamp (3) and opamp (1) keeping the voltage difference across R_{pot} constant. . Note that, if the equivalent resistance of the load exceeds a level, opamp (2) enters into saturation and the circuit does not act as a current source anymore. Therefore, R_{pot} must be adjusted considering this limitation.

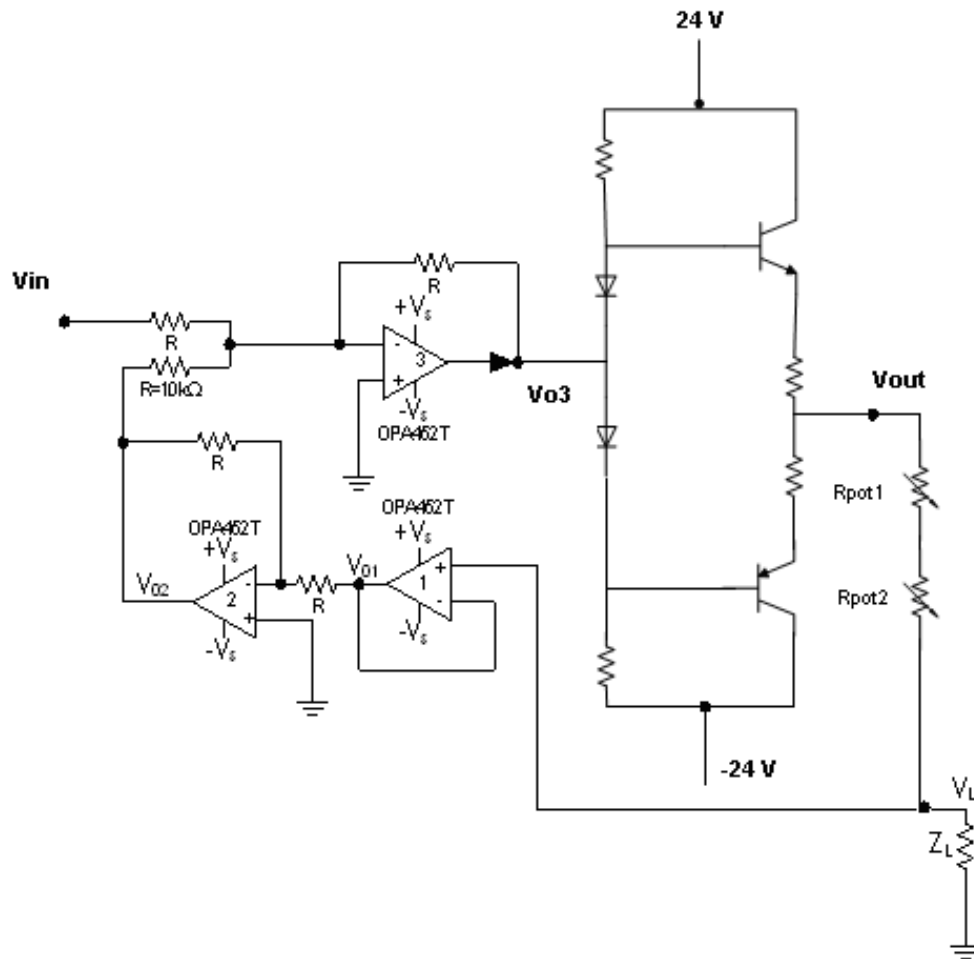


Fig. 4.1 Voltage to Current Converter (V/I) Circuit. AB Class amplifier stage is used to amplify current and remove crossover distortion. $R=10\text{ k}\Omega$, $R_1=680\ \Omega$, $R_2=10\ \Omega$, $R_{\text{pot1}}=2\text{ k}\Omega$, $R_{\text{pot2}}=500\ \Omega$.

Second stage of the circuit is used to amplify the current. Amplifier circuit is designed to deliver higher output current. Biasing diodes are chosen to match the characteristics of the matched transistors used for biasing. This low diode-biasing-voltage causes both transistors to slightly conduct even when no input signal is present. A nonzero input signal waveform will cause the transistors to operate in their

active region thereby eliminating any crossover distortion. Since operating current values are high, power transistors (TIP 41C) are used in the circuit. AB Class amplifier stage is used to carry a less quiescent current and removing crossover distortion.

The maximum power supply ranges of OPA452 opamps are ± 10 V to ± 40 V, so they can provide 10 mA continuously. In the experimental studies, 5 to 10 mA currents are applied to the phantom for 6 to 10 minutes.

4.1.2 Frequency Characteristics of the Output Resistance

Output resistance of the circuit is calculated experimentally at different frequency values and frequency response of the circuit is obtained between 50 Hz and 50 kHz.

Output resistance characteristic of the circuit is defined by connecting a high value resistance ($R_{ins} = 1 \text{ M}\Omega$) in parallel to the output of the circuit (Fig. 4.2). The voltage value is recorded for each frequency and output resistance values are calculated at several frequency values in between 50 Hz to 50 kHz. The circuit does not work properly after 50 kHz due to operational amplifier's limitations (OPA 452 operates stable up to 50 kHz according to its data sheet). The mathematical basis of this approach is described below:

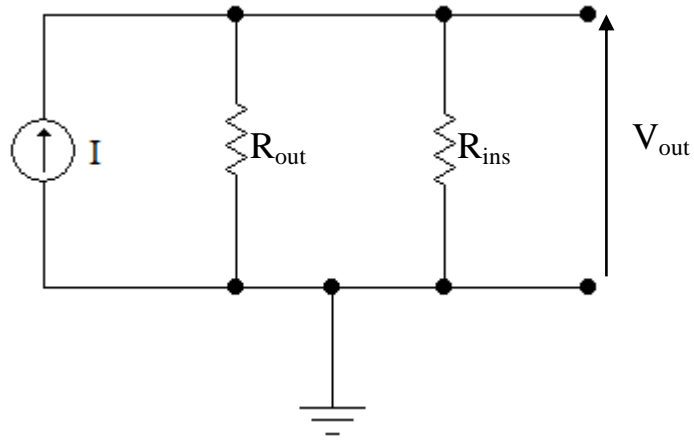


Fig. 4.2 Circuit for calculating the output resistance of the VCCS. High value resistors (R_{ins}) are connected in parallel to the output of the circuit and voltage (V_{out}) values are recorded for each frequency.

$$I \times R_{out} = V_1 \quad (4.1)$$

$$I \times (R_{out} // R_{ins}) = V_2 \quad (4.2)$$

Since output current is independent from the load resistance (within its limits), the applied current is assumed constant (i.e., equal to I) in both equations (4.1 and 4.2). When these equations are divided by each other, we obtain

$$\frac{R_{ins} + R_{out}}{R_{ins}} = \frac{V_1}{V_2} \quad (4.3)$$

Consequently, R_{out} is obtained as:

$$R_{out} = R_{ins} \left(\frac{V_1}{V_2} - 1 \right) \quad (4.4)$$

This procedure is repeated at each frequency value and frequency characteristic of the output resistance is presented in Table 4.1

Table 4.1
Output Resistance Values at Different Frequencies

Frequency (Hz)	Output Resistance Value (kΩ)
500	856,8
1000	766,8
5000	662,3
10000	549,6
15000	465
20000	390,1
25000	324,6
30000	270,1
35000	205,9
40000	160,2
45000	151,7
50000	144,4

The load resistance due to the breast tissue phantom corresponds to almost 2 k Ω . Since output resistance of the current source circuit is almost 75 times more than the load resistance (at 50 kHz), current generator can inject constant current into the breast phantom without being exposed to the loading effect in the frequency range of 500 Hz and 50 kHz.

4.2 Experimental Setup

In experiments, two different thermal infrared cameras are used. These are long-wave band uncooled micro bolometer and long-wave band cooled Quantum Well Infrared Photodetector (QWIP) infrared cameras. The first one is a commercial camera (FLIR) used for diagnostic purposes in the Biophysics Department Laboratories of 9 Eylül University, İzmir. The second camera is in the Electrical and Electronics Engineering Department, Quantum Devices & Nanophotonics Research Lab of METU. The detector of the QWIP infrared camera was developed by C. Beşikçi and his research group [145], [146]. The properties of both cameras are given in detail in Table 4.2. In the research plan of this thesis study, after completing the theoretical and numerical parts of Electro-thermal imaging, the second camera at METU was planned to be used in the experimental phase. Since the camera was not available on time, a commercial camera is sought for the initial experimental studies. Consequently, a short visit is made to the Biophysics Department Laboratories of 9 Eylül University to perform the preliminary experimental studies.

Fig. 4.3 shows the experimental setup performed using the uncooled micro bolometer detector camera in the Biophysics Department Laboratories and Fig. 4.4 is the experimental setup with the cooled QWIP detector camera in the Electrical and Electronics Engineering Department, Quantum Devices & Nanophotonics Research Lab of METU.

Experiments are carried out in a temperature controlled room (approximately at 23 °C). Current, within medical safety limits, is applied to the phantom with the voltage controlled current generator described in the preceding section. The phantom which simulates the female breast is modelled using agar, TX-150, TX-151, distilled water

and saline (NaCl) to adjust the conductivity of the healthy breast and cancerous tissue [121]. The focal distance between the camera and phantom is adjusted as 1 m.

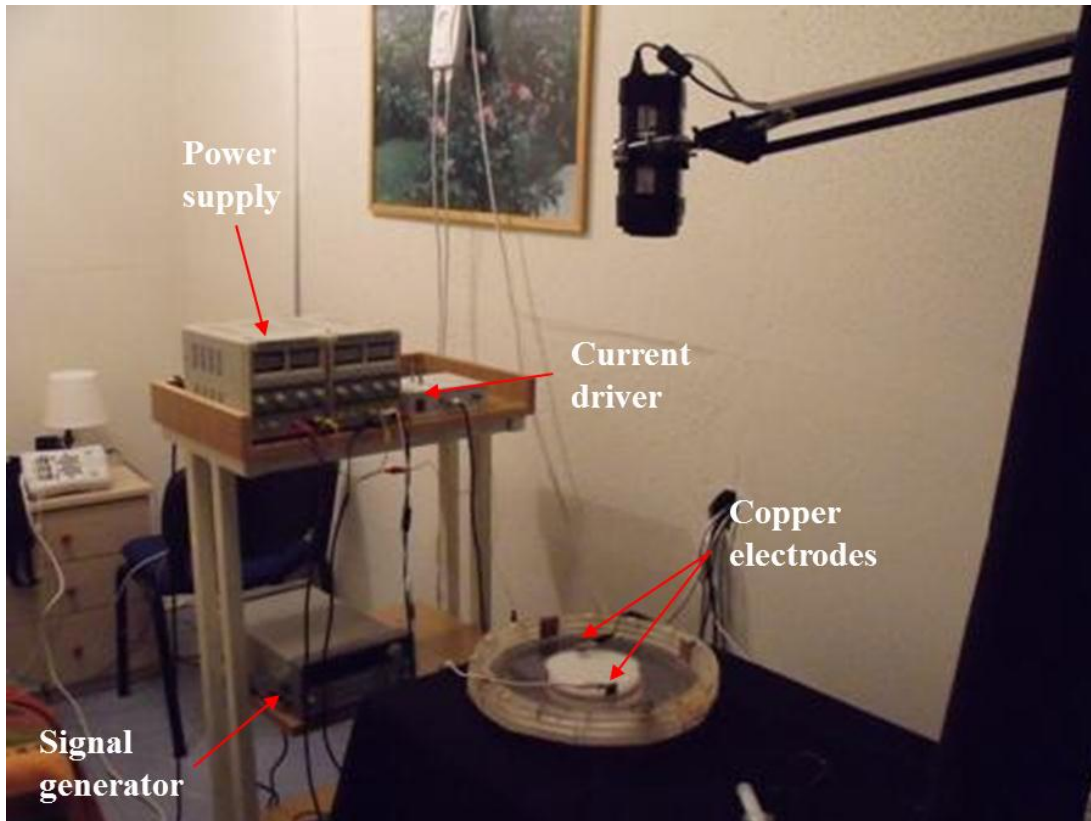


Fig. 4.3 Experimental setup established at 9 Eylül University, Faculty of Medicine, Biophysics Department, İzmir.

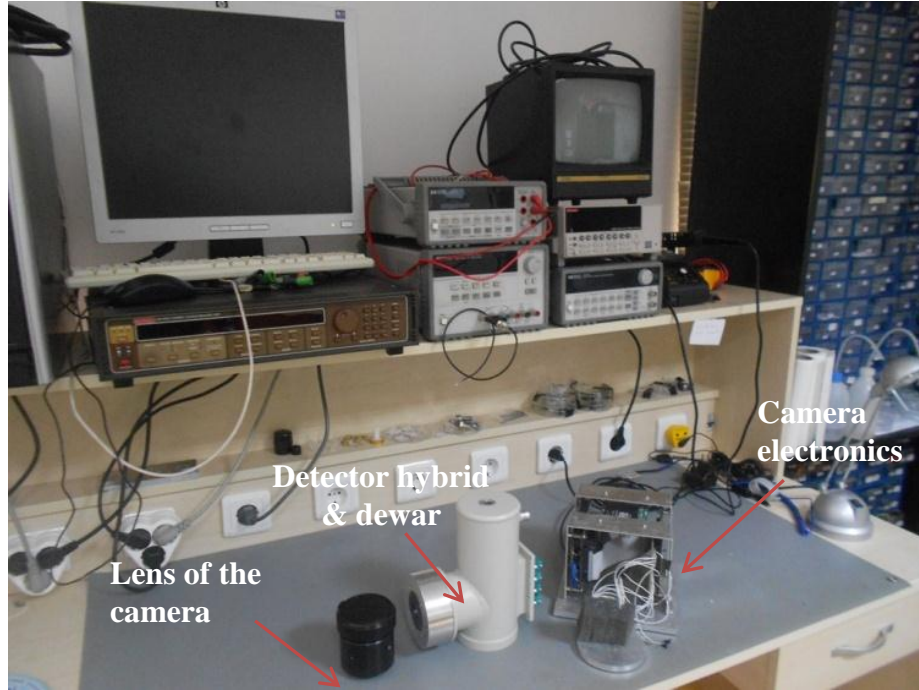


Fig. 4.4 Experimental setup at METU, Electric-Electronics Department, Quantum Devices & Nanophotonics Research Lab.

Table 4.2

Characteristics of the Infrared Cameras used in experiments

	Camera 1	Camera 2
Detector type	Microbolometer	QWIP
Resolution (pixels)	320x240	640x512
Dynamic range (bit)	14	14
Spectral range (μm)	7.5-13	8-9.7
NETD (at 30°C)	50 mK	~ 20-30 mK
Detector cooling	Uncooled	Cooled
Integration time (msec)	12	~ 1
Used frame rate (Hz)	9	25
Max frame rate (Hz)	50 at full frame	400 at full frame
Focus distance (cm)	100	100

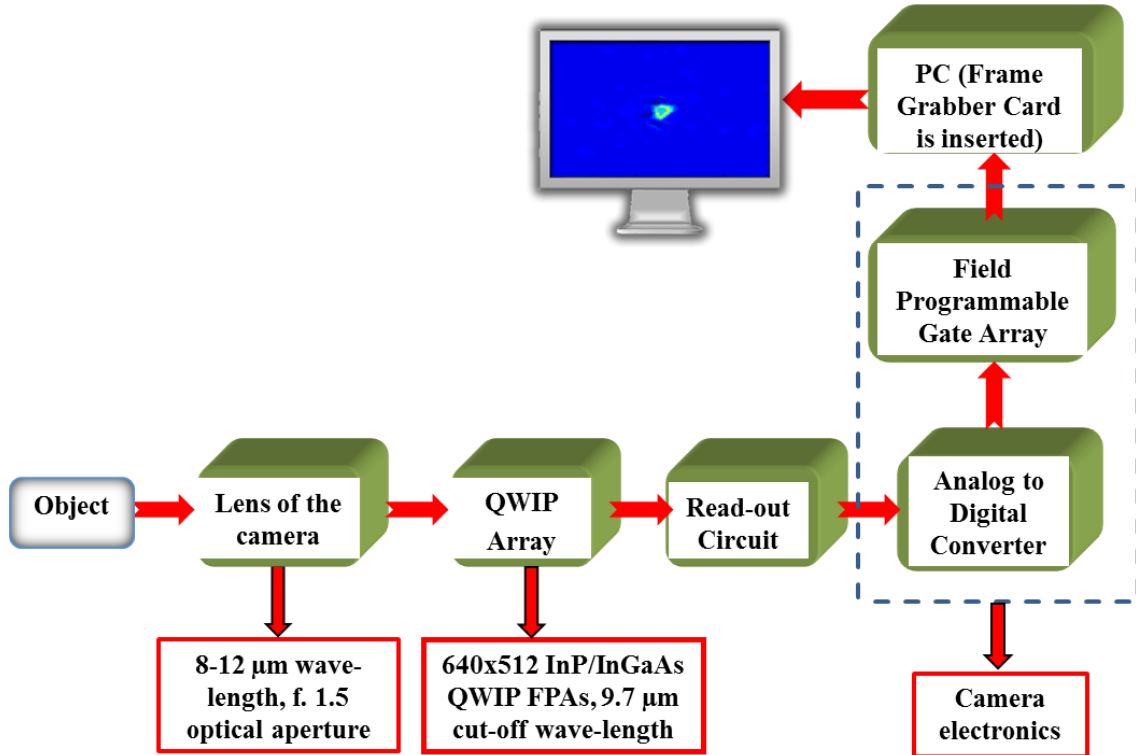


Fig. 4.5 Block diagram of Quantum Well Infrared Photon (QWIP) Detector Infrared Camera developed at METU, Electric-Electronics Department, Quantum Devices & Nanophotonics Research Lab.

Pixel data which is coming from the QWIP array is read out by the readout integrated circuit (ROIC) and sent to the camera electronics. Analog pixel signals are converted into the digital signals in the camera electronics and thermal image is generated.

4.2.1 Model Preparation

One of the best materials that mimic the electrical dielectric property of the woman breast tissue is the agar phantom. It resembles the electrical impedance characteristics of the human tissue in the frequency range of 1 kHz to 10 MHz [33]. For this purpose, an agar phantom is designed with two-compartments (Fig. 4.6). The background of the phantom simulates the healthy tissue. On the other hand, inner tissue which is inserted into the background phantom imitates the malignant tissue. Adjusting the saline ratio of the phantom, electrical conductivity of the model can be altered. So, it is possible to produce different types of tissues such as healthy and malignant breast tissues. Different types of two dimensional models are used in experiments.

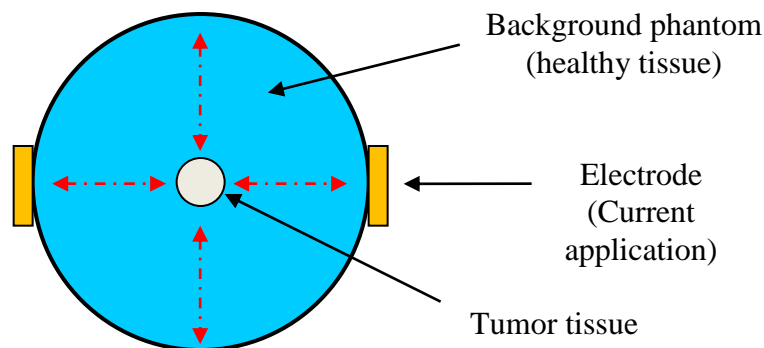


Fig. 4.6 Phantom geometry. Electrodes are inserted to the right and left side boundaries. Background phantom simulates the healthy breast tissue and inner tissue (its location can be moved) mimics the tumor tissue.

Agar powder, the basic component of the phantom, is used to prevent the decomposition of water. The electrical conductivity is adjusted by changing the

sodium chloride (NaCl) ratio of the solution. The following expression shows the relationship between the amount of ingredients and the resulting electrical conductivity of the phantom [62]:

$$S=2 \rho \text{ (S/m)} \tag{4.5}$$

where S is the conductivity of the phantom and ρ shows the amount of NaCl which will be poured into the solution to be able to obtain the desired electrical conductivity. In this formulation, it is assumed that 1.5 gr agar is added into 100 ml distilled water.

To increase the viscosity and to ensure better mixing of the solution, jelling agent TX-150 and TX-151 are used [121]. TX-151 is a new product of TX-150. Since it is improved with preservatives, it has longer shelf life [122]. Figure 4.7 shows one of the agar phantoms used in the experimental studies.

Since a number of specifications must be satisfied simultaneously, preparation of experimental phantoms is a difficult process. For example, phantoms should be rigid enough to preserve their shape. They should not dry out or decompose quickly to keep their electrical properties constant. Some stable phantom compositions used in our experimental studies are presented in Table 4.3.



Fig. 4.7 Agar phantom sample picture. Copper electrodes are inserted to the boundary of the model and tumor tissue is located 1 cm away from the left side boundary.

Table 4.3
Phantom Ingredients and Corresponding Conductivity Values

Ingredients	Healthy Tissue 1	Healthy Tissue 2	Healthy Tissue 3	Cancerous Tissue
Distilled Water (ml)	100	100	100	100
Agar (gr)	1.5	1	3	1.5
TX-150 (gr)	---	1	---	---
TX-151(gr)	---	---	1	---
Sucrose (gr)	---	---	---	1.5
NaCl (gr)	0.1	0.05	0.05	0.2
Conductivity (S/m)	0.2	0.1	0.16	1



Fig. 4.8 Thermal-body phantoms used in experiments performed at Quantum Devices & Nanophotonics Research Lab. (Homogeneous and inhomogeneous phantoms including single or poly tumor tissues)

4.2.2 Experimental Process

In some previous *in vitro* studies, an agar phantom is heated, externally. Conway applied microwave to an agar phantom and a 7 °C rise in temperature was obtained within 30 minutes. Temperature increases are measured by inserting thermocouples inside the phantom and using a 16 electrode electrical impedance tomography system [114]. Solazzo *et al.* used an agar phantom in their experimental radiofrequency ablation study to investigate the relationship between the RF induced heating with the background electrical conductivity [123].

In this thesis, a pair of electrodes is attached on the surface of the agar phantoms and alternating/direct current is applied from these electrodes. The resulting changes in temperature are measured using a thermal infrared camera.

In the experimental studies, there are no metabolic heat sources and blood perfusion. Thus only the effects of electrical current application can be observed. Moreover, the physical (density and specific heat of tissue), electrical (electrical conductivity and permittivity of tissue) and thermal properties (thermal emissivity and conductivity of tissue) of the phantom cannot be adjusted exactly the same with real breast tissue parameters. Consequently, some differences in results (temperature increases and contrasts) must be expected compared to simulation results.

Different experiments are performed by changing the location and the dimension of the cancerous tissue. Experiments are also performed for multi tumours. Thermal images are taken for each case and temperature distributions of the phantoms are obtained in active and passive modes.

4.2.3 Calibration of the Infrared Cameras

Detectors of thermal infrared cameras mostly detect the temperature differences. To be able to obtain accurate temperatures and quantify the temperature differences, cameras must be calibrated. Otherwise, the same image on two different computer displays may have different temperature values due to different display settings. Therefore, before each experimental study, calibration of the camera should be completed, especially for medical diagnostic applications. Calibration parameters should be relevant with the dynamic range of the experimental study which, in this study, is concentrated on breast imaging. For breast imaging, the temperature differences of interest are mostly 100 °mC at about 37 °C [99]. Experimental studies are implemented in between 23 °C to 25 °C. Thus, dynamic range is pretty narrow. In

literature, accepted calibration parameters are 1) 100 °mC resolution at 24 °C or 37 °C (depending on the body to be imaged), 2) an accuracy of 300 °mC, and a 3) drift (stability) of 100 °mC per hour [99]. Non-uniformity calibration is also implemented to remove non-uniformities across the focal plane array. There are two methods for calibration, namely, internal and external calibrations. The camera that uses micro bolometer detectors is calibrated externally prior to each use. Two different blackbody sources are used as a temperature reference source in the calibration process. The first one is at room temperature and the other one is 13 °C higher than the room temperature. 13 °C temperature difference corresponds to 850 digital signal levels in the camera. Therefore, one digital level corresponds to approximately 15 °mC temperature difference. Experiments are carried out in a controlled manner, i.e., the room temperature is kept stable in between 23 °C to 25 °C during an experimental period.

4.3 Experimental Results

In-vitro experiments are carried out using two different long-wave band thermal infrared cameras (uncooled micro bolometer and cooled QWIP). Alternating and direct current are applied within medical safety limits and temperature distributions of the phantoms are recorded.

4.3.1 Homogeneous Phantom in Active Mode of Operation

In this study, 10 mA (10 kHz) current is applied for 600 msec. Fig. 4.9 denotes the 2-D phantom used in this part of the study. Two-dimensional healthy breast tissue is modeled with a circular homogeneous phantom which has 8 cm diameter. The electrical conductivity of the tissue is adjusted as 0.2 S/m. The temperature distribution of the agar phantom is imaged both in passive and active modes. Difference of the images is taken to observe the effects of the current application (see Fig. 4.10). In active mode, a temperature contrast of 0.092 °C is obtained on the phantom.



Fig. 4.9 Homogeneous agar phantom. Current is applied with copper electrodes located at right and left side of the phantom.

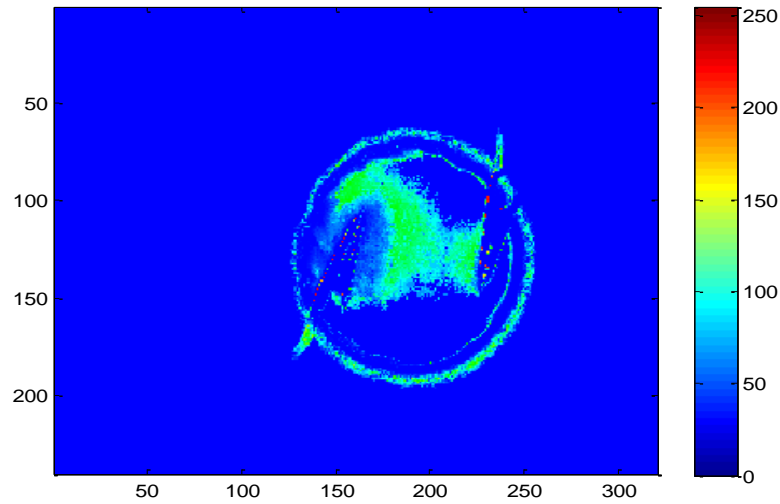


Fig. 4.10 Difference of images (taken in active and passive mode) (Using micro bolometer uncooled thermal infrared camera (spatial resolution is 320 x 240 pixels) at 9 Eylül University, Faculty of Medicine, Biophysics Department, İzmir). Color bar indicates the temperature difference ($^{\circ}\text{mC}$).

4.3.2 Inhomogeneous Phantom in Active Mode of Operation

In this part, 5 mA (10 kHz) current is applied for 600 msec. Healthy breast tissues is modeled with a circular phantom which has a 10 cm diameter. The malignant tissue is simulated as a smaller circular region which has a 1 cm diameter. Tumor is placed 1 cm away from the surface electrode (Fig. 4.11). Almost 40 $^{\circ}\text{mC}$ temperature contrast occurs due to the tumor tissue in the active mode. The difference of homogeneous and inhomogeneous phantom images is shown in Fig. 4.12. The ratio of these images is shown Fig. 4.13. A noticeable temperature contrast is obtained in latter figure. Since there is no metabolic heat generation, temperature contrast does not occur in passive mode. One can benefit greatly from electrical conductivity of the tissues being different from each other (cancerous tissue has higher electrical

conductivity compared to the healthy tissue). Due to this phenomenon, the tumor tissue can be detected using an infrared camera.

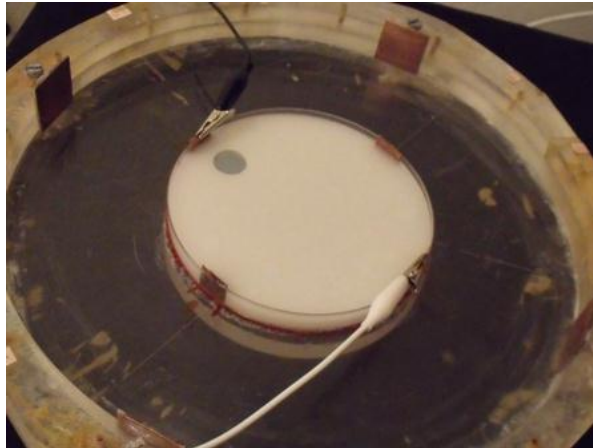


Fig. 4.11 Agar phantom including an inhomogeneity representing the tumor tissue. Electrodes are attached at the boundary of the phantom.

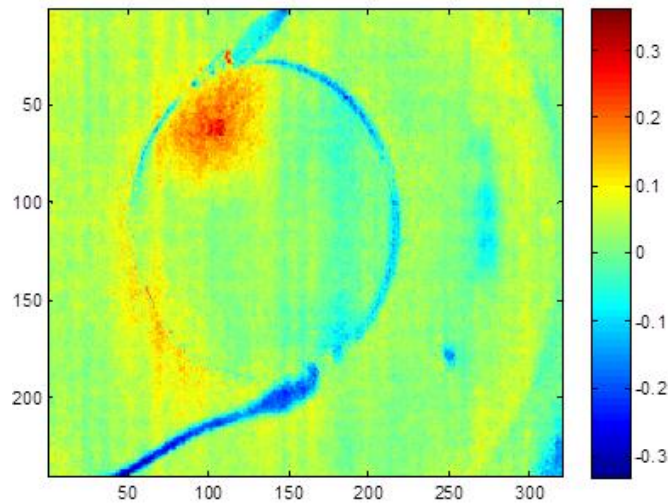


Fig. 4.12 Differences of healthy and tumor tissue images (Using micro bolometer uncooled thermal infrared camera (spatial resolution is 320 x 240 pixels) at 9 Eylül University, Faculty of Medicine, Biophysics Department, İzmir), Color bar indicates the temperature difference ($^{\circ}\text{C}$).

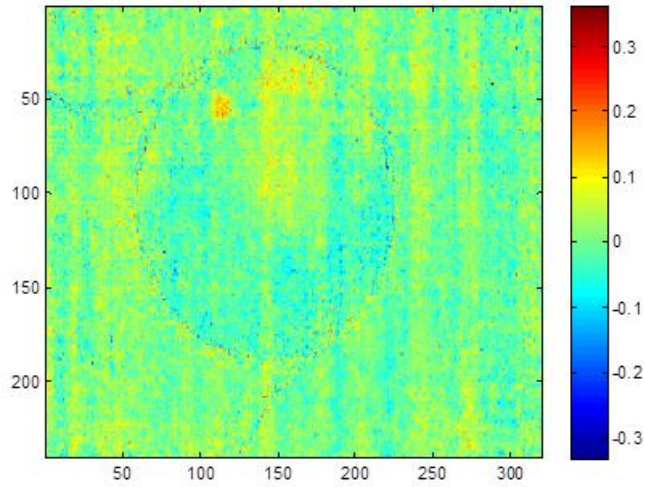


Fig. 4.13 Ratio of healthy and tumor tissue images (Using microbolometer uncooled thermal infrared camera (spatial resolution is 320 x 240 pixels) at 9 Eylül University, Faculty of Medicine, Biophysics Department, İzmir), Color bar indicates the temperature difference ($^{\circ}\text{C}$).

4.3.3 Inhomogeneous Phantom in Active Mode (DC)

Fig. 4.8 shows various thermal body phantoms used in experiments performed at Quantum Devices & Nanophotonics Research Lab in the Middle East Technical University, Ankara. Specifications of the camera are found in Table 4.2.

In this study, 10 mA direct current (DC) is applied for 600 msec. Healthy breast tissues are modeled with a two-dimensional phantom which has a diameter of 10 cm. The circular malignant tissue has a 1 cm diameter and it is placed in the healthy breast phantom 1 cm away from the surface electrode. Temperature distributions are recorded twice, i.e., in passive (see Fig. 4.14) and active (see Fig. 4.15) modes. Approximately, 0.055°C temperature contrast is obtained due to the tumor tissue in

active mode of operation. Tumor tissue can be easily diagnosed using the ratio of healthy and tumor images (see Fig. 4.16).

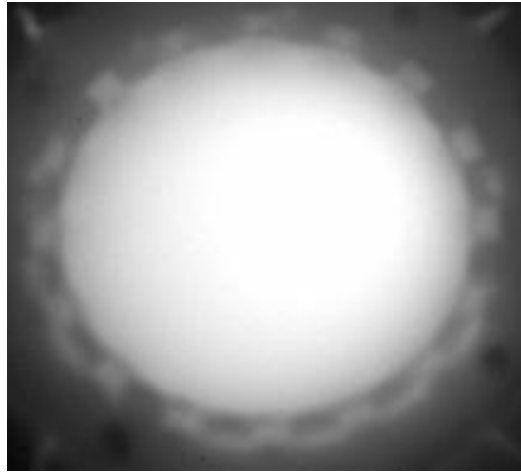


Fig. 4.14 Thermal image of the phantom in passive mode (Using QWIP cooled thermal infrared camera at METU, Electric-Electronics Department, Quantum Devices & Nanophotonics Research Lab.)

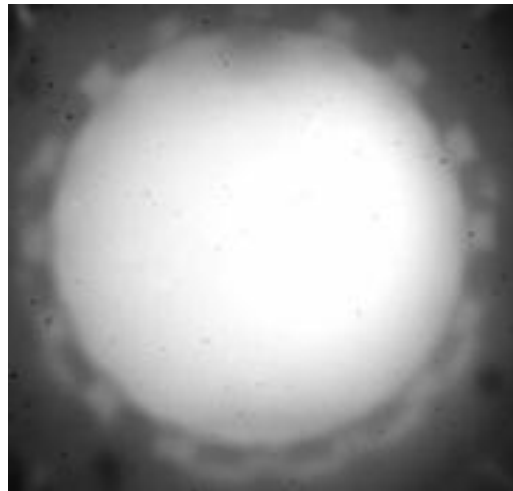


Fig. 4.15 Thermal image of the phantom in active mode (10 mA current (DC) stimulation for 600 sec), (Using QWIP cooled thermal infrared camera at METU, Electric-Electronics Department, Quantum Devices & Nanophotonics Research Lab).

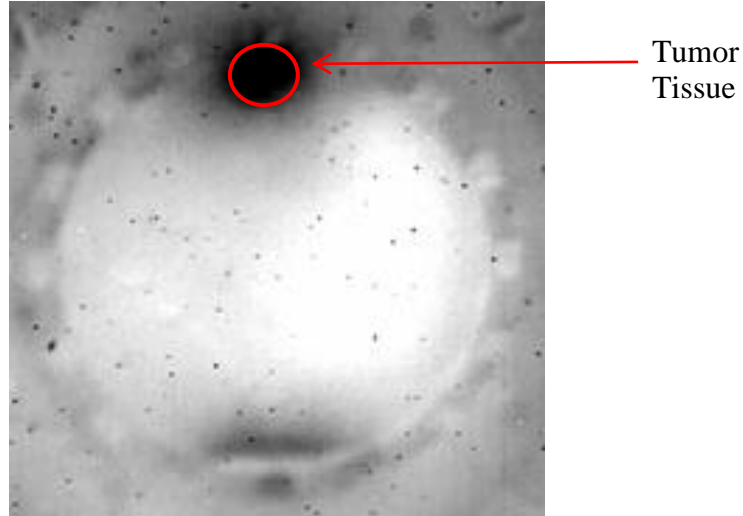


Fig. 4.16 Ratio of thermal images (taken in active and passive mode) (Using QWIP cooled thermal infrared camera at METU, Electric-Electronics Department, Quantum Devices & Nanophotonics Research Lab.)

4.3.4 Dual Malignant Tissues in Active Mode

In this study, 5 mA alternating current (10 kHz) is applied for 600 msec. Healthy breast tissue is modeled with a two dimensional circular phantom which has a 10 cm diameter and dual tumors of 1 cm diameter are placed in the healthy breast phantom. Tumors are located 2 cm away from the surface electrode.

Temperature distributions of the poly tumor tissue are obtained in passive and active modes. After the heating process (current injection), the contrast of the tumor signal (max. signal value at the tumor location) and the average of the background signal (healthy tissue) equals to 3.3 digital levels (1 digital signal level corresponds to 15.3 °mC). Consequently, almost 0.05 °C temperature contrast is obtained due to the current application.

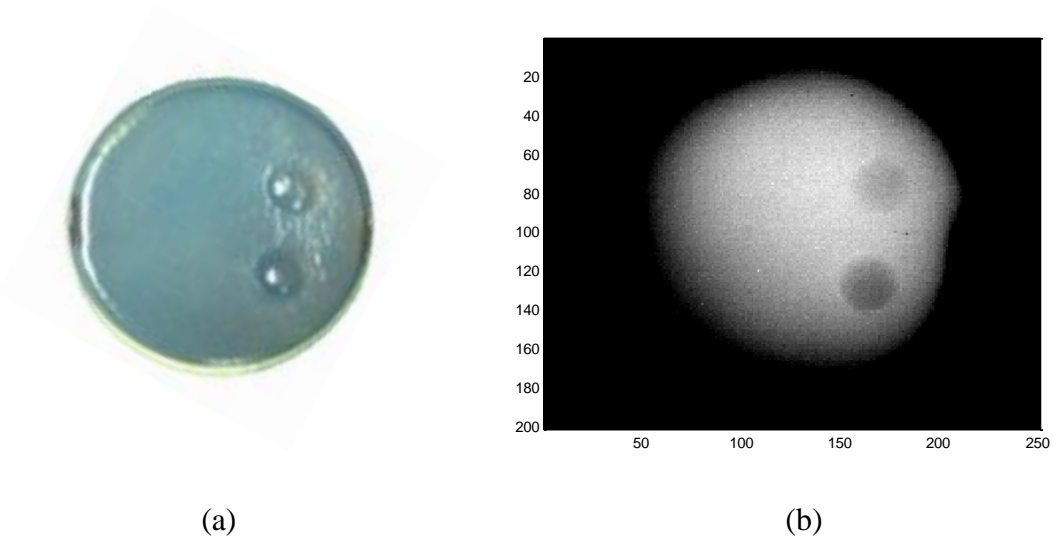


Fig. 4.17 (a) Agar phantom including the dual tumor tissue, (b) Ratio of thermal images (taken in active and passive mode) (Using QWIP cooled thermal infrared camera at METU, Electric-Electronics Department, Quantum Devices & Nanophotonics Research Lab)

Since, thermal emissivity and temperature of the healthy and tumor tissue are the same, cancerous tissue cannot be determined in the temperature distribution of the thermal-body phantom in passive mode of operation. However, by applying currents in medical safety limits, a temperature contrast is created in between the tumor and the healthy tissue. Fig. 4.17 shows the ratio of thermal images taken in active and passive modes. The dual tumor tissue can be detected due to the temperature contrast generated in active mode.

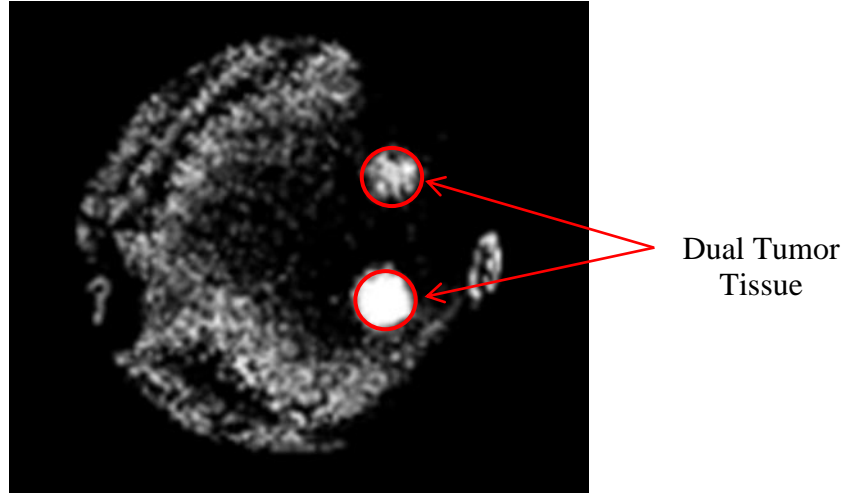


Fig. 4.18 Ratio of healthy and tumor tissue images in active mode of operation (Using QWIP cooled thermal infrared camera at METU, Electric-Electronics Department, Quantum Devices & Nanophotonics Research Lab)

The ratio of tumor and healthy tissue is shown on Fig. 4.18. By using the ratio of the homogeneous and inhomogeneous phantom images in active mode the current artifacts are removed. However, there are artifacts due to 1) deviations in the phantom materials, 2) registration errors, and 3) changes in the experimental conditions, etc.

Despite all these deficiencies, the temperature contrast is enhanced when the thermal images in active mode is scaled by the thermal image of the homogeneous phantom.

4.4 Summary and Discussions

In this experimental part of the study, it is objected to observe whether the temperature contrast created by the tumor tissue can be improved just due to the current application within medical safety limits.

In experiments, applied current is within the medical safety limits and expected temperature contrasts are around 100 °mC according to the simulation results. Since infrared cameras are used to image the temperature distributions, temperature contrasts should be in the range of thermal sensitivity of the cameras. The NETD of the uncooled microbolometer camera (used in experiments) is 50 mK and the cooled QWIP camera (used in experiments) is approximately 20-30 mK. Tissue phantom stayed immobile during the experiments (about 10 minutes) so integration times of the cameras did not reduce the thermal sensitivity. The pixel number of the uncooled microbolometer camera is 320×240 and the cooled QWIP camera is 640×512. The phantom used for the healthy (10 cm diameter) and the malignant tissue (1 cm diameter) are circular models. When the camera is focused on the phantom, the field of view (FOV) of the uncooled microbolometer camera is 10x10 cm (corresponding to a 0.031 cm × 0.041 cm pixel size). The same FOV is obtained by the QWIP camera using pixels of size 0.0156 cm × 0.0195 cm. Thus, the pixel sizes in both cameras are much smaller than the area of tumor tissue (1x1 cm) which are sufficient to follow the temperature contrasts of the malignant tissue.

The main components of the in vitro experimental study are thermal-body phantom, a current generator and a thermal camera. Voltage-controlled AC current source (VCCS) is designed to supply constant current into the breast phantom independent of the load specifications.

To perform realistic experiments, phantoms should simulate the dielectric and thermal properties of the female breast. In the literature, the best material used to model the biological tissue is the agar. Therefore, an agar phantom is used in the experiments to create a thermal-body phantom. It mimics the tissue's electrical characteristics in between 1 kHz to 10 MHz [33]. The emissivity of the designed phantom (0.95-0.98) resembles the tissue emissivity. The dimension of the circular phantom (a diameter of 10 cm) is also adjusted to be consistent with the simulation study (a square of 10×10 cm) and the realistic breast model (a half sphere with a 14 cm diameter). Body phantom is composed of two compartments which are healthy and cancerous tissue. Since cancerous tissue has a higher electrical conductivity compared to the malignant tissue, NaCl is used to adjust the electrical conductivity of the different tissues. There are also another ingredients used in the model preparation. Jellying agents TX-150 and TX-151 products are for increasing the viscosity and providing better mixing of the solution. Experimental agar phantoms are presented in Table 4.3.

Experimental imaging process has three steps: 1) observing the temperature contrast on the homogeneous phantom due to the current application, 2) measuring the temperature contrast of the inhomogeneous phantom due to AC and DC electrical stimulation, and 3) detecting the temperature contrast of a dual tumor configuration.

In the first part of the experiments, the difference image of the active and passive (no heating occurs) modes is obtained and temperature contrast due to current application is calculated (Fig. 4.10). Applied current causes 92 °mC temperature increase on the homogeneous body phantom.

Second part of the experiments can be divided into two subsections. First part of the study is carried out by applying an AC excitation at 10 kHz. Tumor tissue is detected

by taking the difference and ratio images of homogeneous and inhomogeneous phantom temperature distributions. Tumor tissue creates almost 40 °mC temperature contrast in AC mode of operation. Another important result is removing the electrode artifacts in large extent by taking the ratio of images. Next, ratio of thermal images taken in active and passive modes is obtained by applying a DC excitation. Direct current application leads to 55 °mC temperature contrast in the tumor tissue.

Last part of the experiments is implemented to observe the effects of a dual malignant tissue. Ratio of thermal images taken in active and passive modes, and ratio of homogeneous and inhomogeneous tissue images in active mode are obtained. The contrast of the dual malignant tissue and the average of the healthy tissue is calculated as almost 50 °mC in active mode of operation. Temperature contrasts are detected both in the ratio of thermal images taken in active and passive modes and ratio of the healthy and tumor tissue images. However, image resolution is better in the ratio of images taken in active and passive modes compared to the ratio of the healthy and tumor tissue images. Although current artifacts are disappeared by taking the ratio of images; deviations in the phantom, registration errors and changes in the experimental conditions may cause extra artifacts. Even if tumors are located close to each other, boundaries of the tumors are distinctive and image resolution of the thermal image is almost same with image of the single tumor. Temperature contrasts of each tumor tissue can be clearly sensed with the infrared camera (Fig. 4.18).

Since there are no heat sources (metabolic heat source) or blood perfusion affecting the thermal-body phantom, experimental studies show the bare effect of the current application on temperature contrast. Results show that applying currents in the medical safety limits enhances the temperature contrast in substantial amounts that can make the invisible tumors visible.

Since the current driver can operate in the frequency range of 10-50 kHz, experiments are implemented at single frequency (10 kHz). More than one temperature distribution for the same body can be obtained at different frequency operations and this provides more detailed information about the tissue. Therefore, experimental multi-frequency study is required as a future work.

CHAPTER 5

CONCLUSION

In this thesis study, a new imaging modality, named as *medical Electro-Thermal Imaging*, is proposed.

Firstly, the electromagnetic and thermal problems are defined. Governing partial differential equations for the electric field and temperature distribution inside the conductive body are identified. Feasibility of the proposed technique is assessed analytically. To be able to determine the optimal current excitation time, time constants of different tissues are calculated. Current application within medical safety limits yields an additional heat generation rate about 25000 W/m^3 (Note that, the metabolic heat generation value for cancerous tissue is 29000 W/m^3). Thus, electrical currents create an additional heat source which is almost equal to the metabolic heat source. Temperature rise due to the uniform current excitation in a tumor tissue is calculated as $659 \text{ }^\circ\text{mC}$ at steady state for a uniform tissue. Since the surface area of the female breast is very small, the total rate of heat transfer due to convection and radiation (about 9 W) can be assumed very low compared to the metabolic heat generation, heat source due to the blood perfusion, and the external heat sources due to the current application.

Two- and three-dimensional realistic breast models are developed (including the cancerous tissue) to investigate the feasibility with numerical simulations. Simulations are implemented by using Comsol Multiphysics Modeling and Matlab

Software Tools, and thermal images of an electrically stimulated female breast are obtained.

Temperature distributions are obtained both in passive and active modes for two- and three-dimensional models. In the 2-D model, the temperature contrast is improved by 117 °mC (26.5 % increases in the contrast) in active mode (when the tumor is located at the center). When the same size of tumor is moved to the boundary (tumor is placed 1 cm away from the left side electrode), the temperature contrast is increased 384 °mC (85 % increases in the contrast) with respect to the passive mode. In transient response study, optimal current excitation duration is calculated about 500 sec. In the 3-D breast model, to determine the depth dependency of the tumor tissue, temperature distributions are obtained in between 1 cm to 9 cm. In active mode, more than 20 °mC temperature contrasts are obtained to a depth of 8 cm. The closer the tumor tissue to the surface, the higher the temperature contrast is acquired by current application. To determine how deeply the cancerous tissue can be detected, the effects of different tumor locations on the top surface temperature distribution are investigated in active mode of operation. In passive mode, a 3.4 mm³ tumor (d=1.5 mm side length) can be detected at 3 mm depth. On the other hand, in active mode, a 3.4 mm³ tumor located at 9 mm depth and a 42.8 mm³ tumor located at 1.5 cm depth generate more than 20 °mC temperature contrast on the breast surface and can be sensed with the modern thermal imagers. Poly tumors (3.4 mm³), like single tumor, can also be detected at 9 mm depth in active mode of operation.

The parameters that affect the temperature increase generated by the malignant tissue are the tumor dimension, amplitude, duration and frequency of the stimulation current, and location (depth) of the tumor tissue. Increasing the strength of the applied current causes more temperature rise and contrast in the breast tissue. However, we are restricted with the medical safety limits. Tumor dimension is also another important parameter affecting the temperature contrast. As the size of the tumor

increases, higher temperature contrasts are obtained, and consequently, they can be diagnosed from deeper regions of the breast.

If the places of electrodes are changed with respect to the location of the tumor tissue (by moving the fingers (electrodes are inserted on fingers (see Fig. 1.4)), higher temperature contrasts may be achieved.

Altering the frequency of the stimulation current causes changes in electrical conductivity and permittivity values, and hence, different temperature contrasts and correspondingly different temperature distributions can be obtained for the same object. Multi-frequency study is implemented in between 10 kHz and 800 MHz in the thesis study. By combining various images taken at different frequencies, one can provide more detailed information to make a diagnosis, and increase sensitivity of tumors at deeper locations. An increase in frequency (800 MHz) produces a better image, i.e., contrast is preserved while artifacts are almost removed. Furthermore, electrode artifacts can be removed to take the difference or ratio of the images and tumor tissue becomes more apparent.

Various thermal breast phantoms (including tumor tissue) are developed to simulate the female breast tissue. In vitro experiments are implemented using two different thermal infrared cameras in a controlled manner. Humans at normal body temperature emit radiation mostly at long-wave band. Therefore, long wave band (uncooled micro bolometer and cooled QWIP) infrared cameras are used in the studies. Since experiments are implemented in-vitro, there is no metabolic heat generation and blood perfusion. Only the effects and results of the electrical stimulation are investigated. Experimental study is implemented with two-dimensional models. Thermal body phantoms including single and dual tumor tissues are imaged using infrared cameras. Temperature contrasts due to the tumor tissues are obtained. Cancerous tissue is determined using the ratio of healthy and tumor images. 1 cm

diameter single tumor tissue (located 1 cm away from the boundary) causes almost 55 °mC temperature contrast and dual tumor tissue (tumors are located vertically and 2.2 cm away from the right side electrode) creates almost 50 °mC temperature contrast on the thermal-breast phantom (background phantom has 10 cm diameter). Electrode artifacts are reduced by taking the difference and ratio of background (healthy) and tumor images. Ratio of healthy and tumor images show that temperature contrast is increased by the current application.

Although, experimental results are obtained as expected and in agreement with the simulation results, some reasonable numerical differences occurred in between experimental and simulation studies. In the experimental study, 55 °mC temperature contrast is obtained (when the tumor tissue is located 1 cm away from the surface electrode) due to the current application. On the other hand, in the simulation study, 384 °mC temperature contrast is obtained due to the tumor tissue. Higher temperature increases are obtained in simulation results. These differences can be explained with the following reasons. Living tissue characteristics such as metabolic heat source and blood perfusion are taken into account in simulations. They are all extra heat sources for tissues. Next, all parameters and factors are assumed as ideal in simulations, there is no experimental noise. However, there are many factors that can affect the experimental parameters and results. The property of an agar phantom (homogeneity, diffusion time), TX-150 and TX-151 and preservation of the phantom are very important factors. Agar phantom can lose its biological feature in short time periods and diffusion can occur in between healthy and tumor tissue, so electrical conductivity of tissues alters. Inhomogeneous agar phantom tends to be homogeneous within the time. Electrical and thermal properties of tissue can change in short time periods. Another important parameter is imaging conditions and infrared camera specifications and limitations. Since expected temperature contrasts are in the range of 100 °mC for our study, thermal sensitivity (noise equivalent temperature difference) of the infrared camera must be high (< 50 mK) and the calibration should

be stable and accurate enough to match the temperature sensitivity of the camera. Despite all, the analytical, experimental and simulation results are quite consistent with each other.

In conclusion, the current application increases the contrast resolution between the healthy and cancerous tissue (*depth-dependent imaging performance improves from 3 mm to 9 mm for 3.4 mm³ tumor*). These increases in temperature contrast and getting images at different frequencies enable the detection of tumor tissues which are hard to detect, especially when the patient is moving.

The future study may be starting with an experimental multi-frequency study. Experiments can be implemented at various frequencies, and the corresponding temperature distributions can be combined to provide more detailed information about the body. To improve the imaging performance, signal processing algorithms can also be applied. Another possible study is to use a dual band camera (mid-wave (3-5 μm) and long-wave bands (8-12 μm)) in active mode. The absolute temperatures can be measured and a reference temperature map for the healthy breast tissue can be generated. Furthermore, two different images may be obtained at different wave lengths for the same body and this causes more accurate temperature contrast values to minimize the artifacts. Experimental studies can be conducted using three-dimensional breast models.

This thesis study shows the potent of a new imaging modality to screen female breast. It deserves further research to investigate other possible clinical applications.

REFERENCES

- [1] N.G. Gençer, M. N. Tek, 1999, "Forward problem solution for electrical conductivity imaging via contactless measurements," *Phys. Med. Biol.*, 44, pp. 927-940.
- [2] J.C. Newell, 2002, "Special issue on electrical impedance imaging," *IEEE Transactions on Medical Imaging*, 21, pp. 6.
- [3] J. P. Morucci, B. Rigaud, 1996, "Bioelectrical impedance techniques in medicine," *Crit. Rev. Biomed.Eng.*, 24, pp. 655-77.
- [4] K. Boone, D. Barber, B. Brown, 1997, "Imaging resistivity with electricity: report of the European Concerted Action on Impedance Tomography," *J. Med. Eng. Technol.*, 21, pp. 201-32.
- [5] D. C. Barber, B. H. Brown, 1983, "Imaging spatial distribution of resistivity using applied tomography," *Electron. Lett.*, 19, pp. 933-5.
- [6] D. C. Barber, B. H. Brown, 1984, "Applied potential tomography", *J. Phys. E: Sci. Instrum.*, 17, pp. 723-33.
- [7] D. Isaacson, 1986, "Distinguish ability of conductivities by electric current tomography," *IEEE Trans. Med. Imaging*, 5, pp. 91-5.

- [8] Y. Z. Ider, N.G. Gencer, E. Atalar, H. Tosun, 1990, "Electrical Impedance tomography of translationally uniform cylindrical objects with general cross sectional boundaries", IEEE Trans. Med. Imaging, 37, pp. 624-31.
- [9] W. R. Pulvis, R. C. Tozer, D. K. Anderson, I. L. Freeston, 1993, "Induced current impedance imaging," IEEE Proc., 140A, pp. 135-41.
- [10] N. G. Gencer, M. Kuzuoglu, Y. Z. Ider, 1994, "Electrical impedance tomography using induced currents," IEEE Trans. Med. Imaging, 13, pp. 338-350.
- [11] N. G. Gencer, Y. Z. Ider, S. J. Williamson, 1996, "Electrical impedance tomography: induced current imaging with a multiple coil system," IEEE Trans. Biomed. Eng., 43, pp. 139-49.
- [12] I. L. Freeston, R. C. Tozer, 1995, "Impedance imaging using induced currents," Physiol. Meas. , 16 (supp 3 A), pp. A257-A266.
- [13] S. Armstrong, D. Jennings, 2004, "Current injection electrodes for electrical impedance tomography," Institute of Physics Pub., 25, pp. 797-802.
- [14] M. Anbar, 1998, "Clinical Thermal Imaging Today," School of Medicine and Biomedical Sciences, IEEE Engineering in Medicine and Biology, 0739-5175, pp. 25-33.
- [15] R. Joro, A. L. Laaperi, P. Dastidar, S. Soimakallio, 2008, "T. Kuukasjarvi, Imaging of breast cancer with mid- and long-wave infrared camera," Journal of Medical Engineering & Technology, 32, pp. 189-197.

- [16] H. Qi, N. A. Diakides, 2003, "Thermal Infrared Imaging in Early Breast Cancer Detection – A Survey of Recent Research," IEEE Embs 25th Annual International Conference, pp. 1109-1112.
- [17] M. Anbar, L. Milescu, A. Naumov, C. Brown, T. Button, C. Carty, K. Dulaimy, 2001, "Detection of cancerous breasts by dynamic area telethermometry," IEEE Engineering in Medicine and Biology Magazine, 20, pp. 80-91.
- [18] H. F. Carlak, N. G. Gençer, C. Beşikçi, 2010, "Thermal Images of Electrically Stimulated Breast: a simulation study," Medicon 2010 12th Mediterranean Conference.
- [19] R. M. Gulrajani, 1998, "Bioelectricity and Biomagnetism," John Wiley & Sons., pp. 189-193.
- [20] W. R. B. Lionheart, J. Kaipio, C. N. Mcleod, 2001, "Generalized optimal current patterns and electrical safety in EIT," Physiological Measurement, 22, pp. 85-90.
- [21] Comsol Multiphysics Modelling Guide, Version 3.4, Available: <http://www.comsol.com>, last visited on November 2010.
- [22] T. R. Gowrishankar, D. A. Stewart, G. T. Martin, J. C. Weaver, 2004, "Transport lattice models of heat transport in skin with spatially heterogeneous, temperature-dependent perfusion," Biomedical Engineering Online, 3:42, pp. 1-17.

- [23] Z. S. Deng, J. Liu, 2002, "Analytical Study on Bioheat Transfer Problems with Spatial or Transient Heating on Skin Surface or Inside Biological Bodies," Transactions of the ASME, 124, pp. 638-649.
- [24] F. J. Gonzalez, 2007, "Thermal Simulation of Breast Tumors," Instituto de Investigacion en Comunicacion Optica, Universidad Autonoma de San Luis Potosi, 53, pp. 323-326.
- [25] A. J. Fenn, 2007, "Breast Cancer Treatment by Focused Microwave Thermotherapy," pp. 35-40.
- [26] J. R. Bourne, 1996, "Critical Reviews in Biomedical Engineering," 24, pp. 223-255.
- [27] H. F. Carlak, N. G. Gençer, 2009, "Elektriksel Olarak Uyarılmış Göğüs Modelinin Termal Görüntüleme Simülasyonları," 14. Biyomedikal Mühendisliği Ulusal Toplantısı, İzmir.
- [28] H. F. Carlak, N. G. Gençer, C. Beşikçi, 2010, "Akım Uygulamalı Termal Görüntüleme Yöntemi için Üç Boyutlu Meme Modeli ile Benzetimler," 15. Biyomedikal Mühendisliği Ulusal Toplantısı, Antalya.
- [29] D. Yang, M. C. Converse, D. M. Mahvi, J. G. Webster, 2007, "Expanding the Bioheat Equation to Include Tissue Internal Water Evaporation During Heating," IEEE Transactions on Biomedical Engineering, 54, pp. 1382–1388.
- [30] S. Prasad N, D. Houserkova, J. Campbell, 2008, "Breast Imaging Using 3d Electrical Impedence Tomography," Biomed Pap Med Fac Univ Palacky Olomouc Czech Repub, 152, pp. 151–154.

- [31] Z. Deng, J. Liu, 2005, "Enhancement of Thermal Diagnostics on Tumors Underneath the Skin by Induced Evaporation," Proceedings of the 2005 IEEE Engineering in Medicine and Biology 27th Annual Conference.
- [32] T. J. C. Faes, H. A. van der Meij, J. C. de Munck and R. M. Heethaar, 1999, "The Electric Resistivity of Human Tissues (100 Hz–10 MHz): A Meta-Analysis of Review Studies," *Physiol. Meas.*, 20, pp. R1–R10.
- [33] G. Qiao, W. Wang, L. Wang, Y. He, B. Bramer and M. Al-Akaidi, 2007, "Investigation of biological phantom for 2D and 3D breast EIT images," *IFMBE Proceedings* 17, pp. 328–331.
- [34] M. Morrow, R. Schmidt, B. Cregger and C. Hasset, 1994, "Preoperative Evaluation of Abnormal Mammographic Findings to Avoid Unnecesssary Breast Biopsies," *Arch. Surg.*, 129, pp. 1091-1096.
- [35] M. E. Valentinuzzi, 1996, "Bioelectrical impedance techniques in medicine 1. Bioimpedance measurement-First section: General concepts," *Critical Reviews in Biomedical Engineering*, 24, 4-6, pp. 223-255.
- [36] R. H. Bayford, 2006, "Bioimpedance Tomography (Electrical Impedance Tomography)," *Annual Review of Biomedical Eng.*, 8, pp. 63–91.
- [37] D. C. Barber, B. H. Brown, 1983, "Imaging Spatial Distributions of Resistivity Using Applied Potential Tomography," *Electronics Letters*, 19, pp. 933–935.
- [38] D. C. Barber, B. H. Brown, 1984, "Applied Potential Tomography," *Journal of Physics E-Scientific Instruments*, 17, pp. 723–733.

- [39] L. Tarassenko, D. Murphy, M. K. Pidcock, P. Rolfe, 1985, "The Development of Imaging Techniques for Use in the Newborn at Risk of Intraventricular Haemorrhage," Proceedings of the International Conference on Electric and Magnetic Fields in Medicine and Biology.
- [40] W. Breckon, M. K. Pidcock, 1988, "Some Mathematical Aspects of Electrical Impedance Tomography," Mathematics and Computer Science in Medical Imaging, pp. 204-215.
- [41] D. Isaacson, 1986, "Distinguishabilities of Conductivities by Electric Current Computed Tomography," IEEE-TMI, 6, pp. 91-95.
- [42] W. Breckon, M. K. Pidcock, 1988, "Ill-Posedness and non-linearity in Electrical Impedance Tomography," Information Processing in Medical Imaging, pp. 235-244.
- [43] K. S. Paulson, W. R. Lionheart, M. K. Pidcock, 1988, "Pompus: an Optimised EIT Reconstruction Algorithm," Inverse Problems, 11, pp. 425-437.
- [44] E. Atalar, 1985, "An Iterative Backprojection Algorithm for Electrical Impedance Imaging Using Finite Element Method," Master's Thesis, Middle East Technical University, Ankara, TURKEY.
- [45] T. Murai, Y. Kawaga, 1987, "Electrical Impedance Computed Tomography Based on a Finite Element Method," IEEE Transactions on Biomedical Engineering, 32, Ankara, pp. 177-184.

- [46] N. G. Gençer, Y. Z. İder, M. Kuzuoğlu, 1992, "Sensitivity Analysis of the Backprojection Algorithm in Electrical Impedance Tomography," Proceedings of IEEE EMBS 14th Annual International Conference.
- [47] N. G. Gençer, Y. Z. İder, M. Kuzuoğlu, 1992, "Electrical Impedance Tomography Using Induced and Injected Currents," Proceedings of IEEE EMBS 14th Annual International Conference.
- [48] Q. S. Zhu, W. R. Lionheart, F. J. Lidgey, C. N. Mcleod, K. P. Paulson, M. K. Pidcock, 1993, "An Adaptive Current Tomography Using Voltage Sources," IEEE BME, 40, pp. 163-168.
- [49] A. Wexler, B. Fry, M. R. Neuman, 1985, "Impedance Computed Tomography Algorithm and System," Applied Optics, 24, pp. 3985-3992.
- [50] C. Mcleod, 2005, "EIT for Medical Applications at Oxford Brookes," IOP Publishing Ltd., 12.
- [51] K. S. Paulson, S. Jouravleva, C. N. Mcleod, 2000, "Dielectric Relaxation Time Spectroscopy," IEEE-BME, 47, pp. 1510-1517.
- [52] K. S. Paulson, M. K. Pidcock, C. N. Mcleod, 2004, "A Probe for Organ Impedance Measurement," IEEE-BME, 51, pp. 1838-1844.
- [53] E. J. Woo, S. Lee, C. W. Mun, 1994, "Impedance Tomography Using Internal Current Density Distribution Measured by Nuclear Magnetic Resonance," SPIE, 2299, pp. 377-385.

- [54] I. Frerichs, 2000, "Electric Impedance Tomography (EIT) in Applications Related to Lung and Ventilation: A Review of Experimental and Clinical Activities," *Physiol. Meas.*, 21, pp. R1-R21.
- [55] A. R. Hampshire, R. H. Smallwood, B. H. Brown, R. A. Primhak, 1995, "Multifrequency and Parametric EIT Images of Neonatal Lungs," *Physiol. Meas.*, 16, pp. A175-A189.
- [56] K. S. Cole, R. H. Cole, 1941, "Dispersion and Absorption in Dielectrics," *J. Chem. Phys.*, 9, pp. 341-351.
- [57] B. H. Brown, D.C. Barber, A. D. Leathard, W. Wang, L. Lu, R. H. Smallwood, A. J. Wilson, 1994, "High Frequency EIT Data Collection and Parametric Imaging," *Innov. Tech. Biol. Med.*, 15, pp. 1-8.
- [58] B. H. Brown, D.C. Barber, 1985, "Applied Potential Tomography: Possible Clinical Applications," *Clin. Physiol. Meas.*, 6, pp. 109-21.
- [59] P. Tarjan, R. McFee, 1968, "Electrodeless Measurements of the Active Resistivity of the Human Torso and Head by Magnetic Induction," *IEEE Transactions on Biomedical Engineering*, 15, pp. 266-278.
- [60] A. V. Korzhenevskii, V. A. Cherepenin, 1997, "Magnetic Induction Tomography: Experimental Realization," *Physiol. Meas.*, 21, pp. 469-474.
- [61] H. Griffiths, 2001, "Magnetic Induction Tomography," *Meas. Sci. Technol.*, 12, pp. 1126-1131.

- [62] B. Ülker, 2001, "Electrical Conductivity Imaging via Contactless Measurements: An Experimental Study," Master's Thesis, METU.
- [63] K. Özkan, N. Gencer, 2009, "Low-Frequency Magnetic Subsurface Imaging: Reconstructing Conductivity Images of Biological Tissues via Magnetic Measurements," IEEE Transactions on Medical Imaging, 28, pp. 564-570.
- [64] C. C. Boring, T. S. Squires, T. Tong, 1994, "Cancer Statistics," C A Cancer J Clin., 44, pp. 7-26.
- [65] Y. Zou, Z. Guo, 2003, "A Review of Electrical Impedance Techniques for Breast Cancer Detection," Medical Engineering & Physics, 25, pp. 79-90.
- [66] H. Fricke, S. Morse, 1926, "The Electrical Capacity of Tumors of the Breast," J Cancer Res, 10, pp. 340-76.
- [67] J. Josinet, A. Lobel, C. Michoudet, M. Schmitt, 1985, "Quantitative Technique for Bio-Electrical Spectroscopy," J Biomed Eng, 7, pp. 289-94.
- [68] J. Stelter, J. Wtorek, A. Nowakowski, A. Kopacz, T. Jastrzembski, 1998, "Complex Permittivity of Breast Tumor Tissue," Proceedings of 10th International Conference on Electrical Bio-Impedance, pp. 59-62.
- [69] A. J. Surowiec, S. S. Stuchly, J. B. Barr, A. Swarup, 1988, "Dielectric Properties of Breast Carcinoma and Surrounding Tissues," IEEE Trans Biomed Eng, 35, pp. 257-63.

- [70] S. S. Chaudhary, R. K. Mishra, A. Swarup, J. M. Thomas, 1984, "Dielectric Properties of Normal and Malignant Human Breast Tissues at Radiowave & Microwave Frequencies," *Indian J. Biochem Biophys*, 21, pp. 76-9.
- [71] J. Josinet, 1996, "Variability of Impedivity in Normal and Pathological Breast Tissue," *Med Biol Eng Comput*, 34, pp. 346-350.
- [72] B. Scholz, R. Anderson, 2000, "On Electrical Impedance Scanning-Principles and Simulations," *Electromedica*, 68, pp. 35-44.
- [73] A. M. Campbell, D. V. Land, 1992, "Dielectric Properties of Female Breast Tissue Measured in Vitro at 3.2 GHz. ," *Phys Med Biol*, 37, pp. 193-210.
- [74] J. G. Webster, D. V. Land, 1990, "Electrical Impedance Tomography," Bristol and New York: IOP Publishing, pp. 21-8.
- [75] T. Moritimo, Y. Kinouchi, T. Iritani, S. Kimura, Y. Konishi, N. Mitsuyama, 1990, "Measurement of the Electrical Bio-Impedance of Breast Tumors," *Eur Surg Res*, 22, pp. 86-92.
- [76] B. Singh, C. W. Smith, R. Hughes, 1979, "In vivo Dielectric Spectrometer," *Med Biol Eng Comput*, 17, pp. 45-60.
- [77] Y. Ohmine, T. Moritimo, Y. Kinouchi, T. Iritani, S. Kimura, M. Takeuchi, Y. Monden, 2000, "Non-invasive Measurement of the Electrical Bioimpedance of Breast Tumors," *Anticancer Res*, 20, pp. 1941-6.

- [78] K. Boone, D. Barber, B. Brown, 1997, "Imaging with Electricity: Report of the European Concerted Action on Impedance Tomography," *J Med Eng Technol*, 221, pp. 201-32.
- [79] A. Hartov, R. M. Mazzaresse, T. E. Kerner, K. S. Osterman, F. R. Reiss, 2000, "A Multichannel Continuously Selectable Multifrequency Electrical Impedance Spectroscopy Measurement System," *IEEE Trans Biomed Eng*, 47, pp. 49-58.
- [80] K. S. Osterman, T. E. Kerner, D. B. Williams, A. Hartov, S. P. Poplack, K. D. Paulsen, 2000, "Multifrequency Electrical Impedance Imaging: Preliminary in Vivo Experience in Breast," *Physiol Meas*, 21, pp. 99-109.
- [81] J. Wtorek, J. Stelter, D., A. Nowakowski, 1999, "Impedance Mammography 3D Phantom Studies," *Ann N Y Acad Sci*, 873, pp. 520-33.
- [82] V. A. Cherepenin, J. A. V. Korjenevsky, A. Nowakowski, 2000, "Electric Mammograph," WO Patent WO053090A1.
- [83] V. A. Cherepenin, A. Karpov, A. V. Korjenevsky, V. Kornienko, A. Mazaletskaya, D. Mazourov, 2001, "A 3D Electrical Impedance Tomography (EIT) System for Breast Cancer Detection," *Physiol Meas*, 22, pp. 9-18.
- [84] J. L. Mueller, D. Isaacson, J. C. Newell, 1999, "A Reconstruction Algorithm for Electrical Impedance Tomography Data Collected on Rectangular Electrode Array," *IEEE Trans Biomed Eng*, 46, pp. 1379-86.
- [85] M. Assenheimer, O. Laver-Moskovitz, D. Malonek, 2001, "The T-Scan Technology: Electrical Impedance as a Diagnostic Tool for Breast Cancer Detection," *Physiol Meas.*, 22, pp. 1-8.

- [86] US FDA Document, P970033,
Available: http://www.accessdata.fda.gov/cdrh_docs/pdf/p970033.pdf,
Last Visited on: 21.07.2011.
- [87] R. Halter, A. Hartov, K. Paulsen, 2004, "Design and Implementation of a High Frequency Electrical Impedance Tomography System," *Physiol Meas.*, 25, pp. 379-390.
- [88] N. G. Gençer, Y. Z. İder, 1994, "A Comparative Study of Several Exciting Magnetic Fields for Induced Current EIT," *Physiol Meas.*, 15, pp. A51-A7.
- [89] H. Griffiths, W. R. Stewart, W. Gough, 1999, "Magnetic Induction Tomography. A Measuring System for Biological Tissues," *Ann N Y Acad Sci*, 873, pp. 335-345.
- [90] H. Scharfetter, P. Riu, M. Populo, J. Rosell, 2002, "Sensitivity Maps for Low-Contrast Perturbation within Conducting Background in Magnetic Induction Tomography," *Physiol Meas*, 23, pp. 195-202.
- [91] R. Siegel, J. Howell, 2001, "Thermal Radiation Heat Transfer," London: Taylor & Francis Group., pp. xix-xxvi.
- [92] F. J. Sanchez, S. Calixto, C. Villasenor, 2009, "Novel approach to assess the emissivity of the human skin," *Journal of Biomedical Optics*, 14(2), pp. 024006.
- [93] Flir Systems, User's Manual, The Measurement Formula, pp. 129-132.

- [94] G. Gaussorgues, 1980, "Microwave Technology Series, Infrared Thermography," Chapman & Hall, pp. 11-30.
- [95] T. C. Sağlık Bakanlığı, Kanserle Savaş Dairesi Başkanlığı (Epidemiyoloji ve Kurumu Şube Müdürlüğü), 2004-2006 Yılları Türkiye Kanser İnsidansı.
- [96] Lawson, R.N., 1956, "Implications of Surface Temperatures in the Diagnosis of Breast Cancer," *Can. Med. Assoc. J.*, 75, pp. 309.
- [97] Lawson, R.N., 1957, "Thermography- A New Tool in the Investigation of Breast Lesions," *Can. Serv. Med.*, 13, pp. 517.
- [98] Lawson, R.N., 1958, "A New Infrared Imaging Device," *Can. Med. Assoc. J.*, 79, pp. 402.
- [99] N. A. Diakides, J. D. Bronzino, 2006, "Medical Infrared Imaging," CRC Press, pp. 9.1-9.18.
- [100] G. Cohen, J. Haberman, E. Brueschke, 1965, "Medical Thermography: A Summary of Current Status," *Radiol. Clin. North Am.*, 3, pp. 403.
- [101] R. Hoffman, 1967, "Thermography in the Detection of Breast Malignancy," *Am. J. Obstet. Gynecol.*, 98, pp. 681.
- [102] H. J. Isard, W. Becker, R. Shilo, 1972, "Breast Thermography after Four Years and 1000 Studies," *Am. J. Roentgenol.*, 115, pp. 811.

- [103] H. Spitalier, D. Giraud, R. Amalric, 1982, "Does Infrared Thermography Truly Have a Role in Present-Day Cancer Management?," *Biomedical Thermology*. Alan R. Liss, Inc., NY, pp. 269-278.
- [104] Y. R. Parisky, A. Sardy, 2003, "Efficacy of Computerized Infrared Imaging Analysis to Evaluate Mammographically Suspicious Lesions," *Am. J. Roentgenol*, 180, pp. 263.
- [105] I. Nyirjesy, Y. Ayme, 1986, "Clinical Evaluation, Mammography and Thermography in the Diagnosis of Breast Carcinoma," *Thermology*, 1, pp. 170.
- [106] L. Thomassin, D. Giraud, 1984, "Detection of Subclinical Breast Cancers by Infrared Thermography," *Proceedings of the Third International Congress of Thermology*, pp. 575-579.
- [107] R. Amalric, M. Gautherie, W. Hobbins, A. Stark, 1981, "The Future of Women with an Isolated Abnormal Infrared Thermogram," *La Nouvelle Presse Med*, 10, pp. 3153.
- [108] W. Hobbins, 1981, "Significance of an Isolated Abnormal Infrared Thermogram," *La Nouvelle Presse Med*, 10, pp. 3155.
- [109] C. Gros, M. Gautherie, 1980, "Thermography and Cancer Risk Prediction," *Cancer*, pp. 45-51.
- [110] M. Gautherie, 1982, "Improved System for the Objective Evaluation of Breast Thermograms," *Biomedical Thermology*, pp. 897-905.

- [111] S. M. Love, S. H. Barsky, 1996, "Breast Cancer: An Interactive Paradigm," *Breast J.*, 3, pp. 171.
- [112] A. W. Guy, 1971, "Analyses of Electromagnetic Fields Induced in Biological Tissues by Thermographic Studies on Equivalent Phantom Models," *IEEE Transactions on Microwave Theory and Techniques*, 19-2, pp. 205-214.
- [113] R. P. Zimmer, H. A. Ecker, V. J. Popovic, 1971, "Selective Electromagnetic Heating of Tumors in Animals in Deep Hypothermia," *IEEE Transactions on Microwave Theory and Techniques*, 19-2, pp. 238-245.
- [114] J. Conway, 1987, "Electrical Impedance Tomography for Thermal Monitoring of Hyperthermia Treatment: An Assessment Using in Vitro and in Vivo Measurements," *Clin. Phys. Physiol. Meas.*, 8, pp. 141-146.
- [115] J. Conway, M. Hawley, Y. Mangnall, H. Amasha, G. C. Van Rhoon, 1992, "Experimental Assessment of Electrical Impedance Imaging for Hyperthermia Monitoring," *Clin. Phys. Physiol. Meas.*, 13, pp. 185-189.
- [116] P. Bernardi, M. Cavagnaro, J. C. Lin, S. Pisa, 2004, "Distribution of SAR and Temperature Elevation Induced in a Phantom by a Microwave Cardiac Ablation Catheter," *IEEE Transactions on Microwave Theory and Techniques*, 52-8, pp. 1978-1986.
- [117] M. Mital, E. P. Scott, 2007, "Thermal Detection of Embedded Tumors Using Infrared Imaging," *Journal of Biomechanical Engineering*, 129, pp. 33-39.

- [118] L. Jiang, W. Zhan, M. H. Loew, 2011, "Modeling Static and Dynamic Thermography of the Human Breast under Elastic Deformation," *Phys. Med. Biol.*, 56, 187-202.
- [119] R. Joro, A. L. Laaperi, P. Dastidar, R. Jarvenpaa, T. Kuukasjarvi, 2009, "A Dynamic Infrared Imaging Based Diagnostic Process for Breast Cancer," *Acta Radiologica*, 50, pp. 860-869.
- [120] B. F. Jones, 1998, "A Reappraisal of the Use of Infrared Thermal Image Analysis in Medicine," *IEEE Transactions on Medical Imaging*, 17, pp. 1019-1027.
- [121] W. M. A. Ibrahim, 2008, "Short Review on the Used Recipes to Simulate the Bio-Tissue at Microwave Frequencies," *Biomed 2008, Proceedings 21*, pp. 234-237.
- [122] TX Products Catalogue, Oilcenter.
- [123] S.A. Solazzo, Z. Liu, S. M. Lobo, M. Ahmed, A. U. Hines-Peralta, et al, 2005, "Radiofrequency Ablation: Importance of Background Tissue Electrical Conductivity—An Agar Phantom and Computer Modeling Study," *Radiology* 2005, 236, pp. 495-502.
- [124] G. Hahn, I. Sipinkova, F. Baisch, G. Hellige, 1995, "Changes in the Thoracic Impedance Distribution under Different Ventilatory Conditions," *Physiol Meas.*, 16, pp. 161-173.

- [125] J. C. Newell, P. M. Edic, X. Ren, et al., 1996, "Assessment of Acute Pulmonary Edema in Dogs by Electrical Impedance Imaging," *IEEE Trans. Biomed. Eng.*, 35, pp. 828-833.
- [126] A. Adler, N. Shinozuka, Y. Berthiaume, R. Guardo and J. H. Bates, 1998, "Electrical Impedance Tomography can Monitor Dynamic Hyperinflation in Dogs," *J. Appl. Phys.*, 84, pp. 726-732.
- [127] I. Frerichs, G. Hahn, T. Schroder, G. Hellige, 1998, "Electrical Impedance Tomography in Monitoring Experimental Lung Injury," *Intensive Care Med.*, 24, pp. 829-836.
- [128] I. Frerichs, G. Hahn, T. Schroder, G. Hellige, 1999, "Thoracic Electrical Impedance Tomographic Measurements during Volume Controlled Ventilation – Effects of Tidal Volume and Positive End-Expiratory Pressure," *IEEE Trans. Med. Imaging*, 18, pp. 764-773.
- [129] J. H. Campbell, N. D. Harris, F. Zhang, B. H. Brown, A. H. Morrice, 1994, "Clinical Applications in the Monitoring of Changes in Intrathoracic Fluid Volumes," *Physiol. Meas.*, 15, pp. 217-222.
- [130] I. Frerichs, G. Hahn, T. W. Golisch, M. Kurpitz, et al. 1998, "Monitoring Perioperative Changes in Distribution of Pulmonary Ventilation Detected by Functional Electric Impedance Tomography," *Acta Anaesthesiol. Scand.*, 42, pp. 721-726.
- [131] P. W. A. Kunst, P. M. J. Vries, P. E. Postmus, J. Bakker, 1999, "Evaluation of Electric Impedance Tomography in the Measurement of PEEP- Induced Changes in Lung Volume," *Chest*, 115, pp. 1102-1106.

- [132] N. D. Harris, A. J. Suggett, D. C. Barber, B. H. Brown, 1987, "Applications of Potential Tomography (APT) in Respiratory Medicine," *Clin. Phys. Physiol. Meas.*, 8, pp. 155-165.
- [133] D. S. Holder, A. J. Temple, 1993, "Effectiveness of the Sheffield EIT System in Distinguishing Patients with Pulmonary Pathology from a Series of Normal Subjects," *Clin. and Phys. Applications of Electrical Impedance Tomography*, pp. 277-298.
- [134] A. D. Leathard, B. H. Brown, J. Campbell, F. Zhang, A. H. Morice, D. Tayler, 1994, "A Comparison of Ventilatory and Cardiac Related Changes in EIT Images of Normal Human Lungs and of Lungs with Pulmonary Emboli," *Physiol. Meas.*, 15, pp. 137-146.
- [135] B. M. Eyüboğlu, A. F. Öner, U. Baysal, C. Biber, et al., 1995, "Application of Electrical Impedance Tomography in Diagnosis of Emphysema-A Clinical Study," *Physiol. Meas.*, 16, pp. 191-211.
- [136] I. Frerichs, G. Hahn, G. Hellige, 1996, "Gravity Dependent Phenomena in Lung Ventilation Determined by Functional EIT," *Physiol. Meas.*, 17, pp. 149-157.
- [137] G. Hahn, I. Frerichs, M. Kleyer, G. Hellige, 1996, "Local Mechanics of Lung Tissue Determined by Functional EIT," *Physiol. Meas.*, 17, pp. 159-166.
- [138] P. W. A. Kunst, N. A. Vonk, O. S. Hoekstra, P. E. Postmus, P. M. J. Vries, 1998, "Ventilation and Perfusion Imaging by Electrical Impedance Tomography: A Comparison with Radionuclide Scanning," *Physiol. Meas.*, 19, pp. 481-490.

- [139] N. G. Gençer, M. N. Tek, 1999, "Electrical Conductivity Imaging via Contactless Measurements," IEEE Transactions on Medical Imaging," 18, pp. 617-627.
- [140] Y. A. Çengel, 1998, "Heat Transfer: a practical approach," WBC McGraw-Hill, Chapter 1, pp. 1-47.
- [141] N. M. Sudharsan, E. Y. K. Ng, 2000, "Parametric Optimization for Tumor Identification: Bioheat Equation Using ANOVA and the Taguchi Method," Journal of Engineering in Medicine, 214, pp. 505-512.
- [142] S. Ozen, 2007, "Low-Frequency Transient Electric and Magnetic Fields Coupling to Child Body," Radiation Protection Dosimetry, 128, pp. 62-67.
- [143] Roger W. Pryor, 2011, "Multiphysics Modeling using Comsol: a first principles approach," Jones and Bartlett Publishers, Bio-Heat Models, Chapter 10, pp. 769-794.
- [144] V. Vinh-Hung, R. Gordon, 2005, "Quantitative Target Sizes for Breast Tumor Detection Prior to Metastasis: A Prerequisite to Rational Design of 4D Scanners for Breast Screening," Technology in Cancer Research and Treatment, 4-1, pp. 11-21.
- [145] S. U. Eker, Y. Arslan, C. Beşikçi, 2011, "High Speed QWIP FPAs on InP Substrates," Infrared Physics & Technology, 54, pp. 209-214.
- [146] S.U. Eker, 2010, "Single and Dual Band Quantum Well Infrared Photodetector Focal Plane Arrays on InP Substrates," Ph.D.'s Thesis, METU.

APPENDIX A

THEORY OF ELECTROMAGNETIC AND HEAT PROBLEMS

Electromagnetic Problem

Applied currents generate electric field in the breast area. Electric field intensity is calculated with the Maxwell Equations. Starting from the fundamental electromagnetic field equations, analytical expressions for the electric field is developed.

Starting from Maxwell Equations:

$$\nabla \times \vec{E} = -\frac{\partial \vec{B}}{\partial t} \quad (\text{A.1})$$

$$\nabla \times \vec{H} = \vec{J} + \frac{\partial \vec{D}}{\partial t} \quad (\text{A.2})$$

Where, \vec{E} is the electric field,

\vec{B} is the magnetic flux density,

\vec{H} is the magnetic field,

\vec{j} is the current density,

\vec{D} is the electric displacement,

And partial derivative is with respect to time t.

From these equations, it can be shown that;

$$\nabla \cdot \vec{B} = 0 \quad (\text{A.3})$$

$$\nabla \cdot \vec{D} = q \quad (\text{A.4})$$

Where, q is the volume charge density.

By deriving the above equation (A.4), we made use of the principle of conservation of charge stipulated by the continuity equation

$$\nabla \cdot \vec{j} + \frac{\partial q}{\partial t} = 0 \quad (\text{A.5})$$

Material equations are used to supplement the above field equations.

$$\vec{D} = \epsilon \vec{E} = \epsilon_r \epsilon_0 \vec{E} \quad (\text{A.6})$$

$$\vec{B} = \epsilon \vec{H} = \mu_r \mu_0 \vec{H} \quad (\text{A.7})$$

$$\vec{J} = \sigma \vec{E} + \vec{J}_s \quad (\text{A.8})$$

Where, ϵ is the permittivity,

μ is the permeability,

σ is the conductivity of the medium.

The current density is the sum of the conduction current density and the impressed current density due to the sources.

Conductivities are finite in the biological medium and the following boundary conditions express the discontinuities.

$$n \times (\vec{E}_2 - \vec{E}_1) = 0 \quad (\text{A.9})$$

$$n \times (\vec{H}_2 - \vec{H}_1) = 0 \quad (\text{A.10})$$

Equation (A.9) and equation (A.10) means that tangential components are continuous.

$$(\vec{B}_2 - \vec{B}_1) \cdot \vec{n} = 0 \quad (\text{A.11})$$

Equation A.11 states that normal component is continuous.

$$(\vec{D}_2 - \vec{D}_1) \cdot \vec{n} = q_s \quad (\text{A.12})$$

$$(\vec{J}_2 - \vec{J}_1) \cdot \vec{n} = -\frac{\partial q_s}{\partial t} \quad (\text{A.13})$$

Equation (A.12) and equation (A.13) stipulate the discontinuity.

The E and H fields are generally computed with intermediate quantities known as the scalar and vector potentials.

Since $\nabla \cdot \vec{B} = 0$,

B can be written as:

$$\vec{B} = \nabla \times \vec{A} \quad (\text{A.14})$$

where, A is the magnetic vector potential.

Inserting equation (A.14) into the fundamental electric field equation (A.1), it can be easily shown that \vec{E} is;

$$\vec{E} = -\nabla \Phi - \frac{\partial \vec{A}}{\partial t} \quad (\text{A.15})$$

Where, Φ is the scalar potential. The solution of field problems can be reduced to determining the quantities of scalar and vector potentials.

A vector can only be defined when its curl and divergence are given. If only curl of the vector potential is given, a supplementary gauge condition should be provided [19].

Two different gauges can be used for homogeneous and inhomogeneous mediums.

Lorenz Gauge (for homogeneous medium)

$$\nabla \cdot \vec{A} + \mu\epsilon \frac{\partial \phi}{\partial t} + \mu\sigma\phi = 0 \quad (\text{A.16})$$

Coulomb Gauge (for inhomogeneous medium)

$$\nabla \cdot \vec{A} = 0 \quad (\text{A.17})$$

In our study, there is a cancerous tissue inside the healthy breast tissue. Hence, the medium is inhomogeneous. So, Lorenz gauge cannot simplify operations. Instead, the Coulomb gauge can be chosen to simplify the operations.

Using Coulomb condition, it is possible to obtain decoupled equations for the scalar and vector potentials.

$$\vec{B} = \mu\vec{H} = \nabla \times \vec{A} \quad (\text{A.18})$$

$$\vec{H} = \frac{1}{\mu} \nabla \times \vec{A} \quad (\text{A.19})$$

$$\nabla \times \vec{H} = \frac{1}{\mu} \nabla \times \nabla \times \vec{A} = \vec{J} + \frac{\partial \vec{E}}{\partial t} \quad (\text{A.20})$$

Taking the curl of the equation (A.18) and substituting equation (A.20) into equation (A.18), it can be obtained that;

$$\nabla \times \nabla \times \vec{A} = \mu \vec{J} + \mu \varepsilon \frac{\partial \vec{E}}{\partial t} \quad (\text{A.21})$$

A vector identity states that;

$$\nabla \times \nabla \times \vec{A} = \nabla(\nabla \cdot \vec{A}) - \nabla^2 \vec{A} \quad (\text{A.22})$$

Using the property of a vector identity, it can be shown that;

$$\nabla(\nabla \cdot \vec{A}) - \nabla^2 \vec{A} = \mu(J_s + \sigma \vec{E}) + \mu \varepsilon \frac{\partial \vec{E}}{\partial t} \quad (\text{A.23})$$

Applying the Coulomb gauge;

$$\nabla^2 \vec{A} + \mu \sigma \vec{E} + \mu \varepsilon \frac{\partial \vec{E}}{\partial t} = -\mu J_s \quad (\text{A.24})$$

$$\nabla^2 \vec{A} - \mu \sigma \nabla \phi - \mu \sigma \frac{\partial \vec{A}}{\partial t} - \mu \varepsilon \frac{\partial}{\partial t} \nabla \phi - \mu \varepsilon \frac{\partial^2 \vec{A}}{\partial t^2} = -\mu J_s \quad (\text{A.25})$$

$$\nabla^2 \vec{A} - \mu\sigma \frac{\partial \vec{A}}{\partial t} - \mu\varepsilon \frac{\partial^2 \vec{A}}{\partial t^2} - \mu\sigma \nabla\phi - \mu\varepsilon \frac{\partial}{\partial t} \nabla\phi = -\mu J_s \quad (\text{A.26})$$

Then, first coupled partial differential equation is obtained.

$$\nabla^2 \vec{A} - \mu\left(\sigma + \varepsilon \frac{\partial}{\partial t}\right) \frac{\partial \vec{A}}{\partial t} - \mu\left(\sigma + \varepsilon \frac{\partial}{\partial t}\right) \nabla\phi = -\mu J_s \quad (\text{A.27})$$

To derive the second partial differential equation, it can be started by the divergence of the displacement vector (equation (A.4)).

$$\nabla \cdot \vec{D} = q$$

$$\text{Since } \vec{D} = \varepsilon \vec{E},$$

$$\nabla \cdot (\varepsilon \vec{E}) = q \quad (\text{A.28})$$

$$\nabla \cdot \left(\varepsilon \frac{\partial \vec{E}}{\partial t} \right) = \frac{\partial q}{\partial t} = -\nabla \cdot \vec{J} = -\nabla \cdot (\vec{J}_s + \sigma \vec{E}) \quad (\text{A.29})$$

$$\nabla \cdot \left(\sigma + \varepsilon \frac{\partial}{\partial t} \right) \vec{E} = -\nabla \cdot \vec{J}_s \quad (\text{A.30})$$

$$\text{Since, } \vec{E} = -\nabla \phi - \frac{\partial \vec{A}}{\partial t}$$

Electric field can be inserted into the equation (A.30) and following partial differential equation is provided.

$$\nabla \cdot \left[(\sigma + \varepsilon \frac{\partial}{\partial t}) \nabla \phi \right] + \nabla \cdot \left(\sigma + \varepsilon \frac{\partial}{\partial t} \right) \frac{\partial \vec{A}}{\partial t} = \nabla \cdot \vec{J}_s \quad (\text{A.31})$$

Since there is no source exists in the medium, $\nabla \cdot \vec{J}_s$ term drops and following coupled partial differential equations are obtained for steady state conditions.

Coupled Partial Differential Equations

$$\begin{aligned} \nabla^2 \vec{A} - j\omega\mu(\sigma + j\omega\varepsilon)\vec{A} - \mu(\sigma + j\omega\varepsilon)\nabla\phi &= 0 \\ \nabla \cdot [(\sigma + j\omega\varepsilon)\nabla\phi] + \nabla(\sigma + j\omega\varepsilon) \cdot j\omega\vec{A} &= 0 \end{aligned} \quad (\text{A.32})$$

Using these coupled partial differential equations, electric potential and corresponding electric field can be calculated.

In our problem, there is a finite inhomogeneous medium and current is applied from the boundaries. Therefore, boundary conditions should also be taken into account.

The steady-state electric field $\vec{E} = -j\omega\vec{A} - \nabla\phi$ can be calculated using the coupled partial differential equations and boundary conditions,

$$\sigma \frac{\partial \phi}{\partial n} = \begin{cases} I & \text{on } A \\ -I & \text{on } B \\ 0 & \text{otherwise} \end{cases} \quad (\text{Fig 2.2}) \quad (\text{A.33})$$

Heat Problem

Spatial Heat Source

Due to the applied current from a boundary, electric field occurs and it is calculated with the Maxwell Equations. This electric field creates the spatial heat source in the breast medium.

In Joule heating, the temperature increases due to the resistive heating from the electric current. The electric potential V is the solution variable in the In Plane Electric Currents application mode. The generated resistive heat Q is proportional to the square of the magnitude of the electric current density J . Current density, in turn, is proportional to the electric field, which equals the negative of the gradient of the potential V :

$$Q \propto |J|^2 \quad (\text{A.34})$$

The coefficient of proportionality is the electric resistivity $\rho = 1/\sigma$, which is also the reciprocal of the temperature-dependent electric conductivity $\sigma = \sigma(T)$. Combining these facts gives the fully coupled relation [21].

$$Q = \frac{1}{\sigma} |J|^2 = \frac{1}{\sigma} |\sigma E|^2 = \sigma |\nabla V|^2 \quad (\text{A.35})$$

Where J is current density (A/m^2),

σ is electrical conductivity (S/m),

E is electrical field (V/m),

V is electrical potential (V).

Using Equation A.35, joule heating which is the external heat source is calculated.

Temperature Distribution

To obtain a temperature distribution of the tissue, Pennes proposes a method which describes the effects of the metabolic generation and the blood perfusion over the energy balance. The most common approximation method to figure out heat problems in biological tissues is Pennes Bio Heat Equation. This works explains the thermal interaction between tissues and perfused blood in detail.

$$\rho C \frac{\partial T}{\partial t} + \nabla \cdot (-k \nabla T) = Q_B + Q_{met} \quad (\text{A.36})$$

$$Q_B = \rho_B C_B W_B (T_B - T) \quad (\text{A.37})$$

Where ρ is density (kg/m^3),

C is specific heat (J/kgK),

T is temperature (K),

k is thermal conductivity (W/mK),

Q_{met} is metabolic heat generation (W/m³),

Q_B is heat source due to blood perfusion (W/m³),

ρ_B is blood mass density (kg/m³),

C_B is blood specific heat rate (J/kgK),

W_B is blood perfusion rate (1/s),

T_B is ambient blood temperature (K),

T is an unknown temperature value (K).

When there is no electrical stimulation and correspondingly no external source, existing state can be called as thermal equilibrium state. In the study, current is applied from the surfaces and this causes a new energy source and finishes this state. In this case, a new heat source is generated in the tissue and temperature values will reach a new equilibrium state in a certain period of time. Tissue temperatures increase by means of the current stimulation until having reached the steady state, and the contrast between malignant and healthy tissue increases. This increase yields us to be able to detect cancerous tissue, even if, it is located at deeper locations.

Due to the external source that we create, a new term should be inserted to the Pennes bio heat equation. A new form of the bio heat equation is figured out to obtain different images which have different temperature distributions and contrasts. We

decided to call this modified form of the equation “*Electrically Stimulated Pennes Bio Heat Equation.*”

$$\rho C \frac{\partial T}{\partial t} + \nabla \cdot (-k \nabla T) = Q_B + Q_{met} + Q_{ext} \quad (\text{A.38})$$

Where, Q_{ext} is spatial heat source due to electrical stimulation (W/m^3).

Heat transfer from the skin surface by both convection and radiation to the surrounding air and surfaces at specified temperatures should also be considered as a boundary condition. Some assumptions can be made to determine the total rate of heat transfer due to convection and radiation.

- Operating conditions can be assumed as steady.
- Patient who is imaged is completely surrounded by the interior surfaces of the room.
- Surfaces of the surrounding places are at the same temperature with the air.

The rate of convection heat transfer from the skin to the air in the room can be calculated by the following equation:

$$Q_{conv} = hA_s(T_s - T_\infty) \quad (\text{A.39})$$

h is the convection heat transfer coefficient ($\text{W/m}^2\text{K}$),

A_s is the surface area through which the convection heat transfer takes place (m^2),

T_s is the surface temperature (K),

T_{∞} is the temperature of the air (K).

There will be also heat loose by radiation from the skin to the surrounding wall surfaces of the room. The temperature of surfaces of the walls, floor and ceiling are assumed to be equal to the temperature of the room air and air does not intervene with radiation.

The net rate of radiation heat transfer from the skin to the surrounding walls, ceiling and floor in the room can be calculated by the following equation:

$$Q_{rad} = \varepsilon \sigma A_s (T_s^4 - T_{sur}^4) \quad (A.40)$$

ε is the emissivity of a skin (0.95),

σ is the Stefann - Boltzmann constant ($W/m^2 \cdot K^4$),

A_s is the surface area through which the convection heat transfer takes place,

T_s is the surface temperature,

T_{sur} is the temperature of the surface of the walls, ceiling and floor which are assumed to be equal to the air temperature.

All of the variables and values are known now. They are inserted to the Equation A.38 and unknown temperature value is calculated according to the other parameters. In our study, real electrical and thermal values are inserted to the equation and temperature distributions of the healthy and tumor tissue are obtained.

VITA

Hamza Feza CARLAK

Oğuzlar Mahallesi, 37. Sokak 5/2

Balgat

06531 Ankara / TÜRKİYE

Phone : +90 312 285 59 68

E-mail : fcarlak@metu.edu.tr

Personal Information

Date of Birth : April 9, 1979

Education

Ph.D.:

2004 – 2012

Dept. of Electrical & Electronics Engineering,
Middle East Technical University

Courses: Introduction to Medical Imaging, Fundamentals of Biomedical Engineering, Digital Signal Processing, Linear System Theory, Medical Imaging, Numerical Methods for Electromagnetics, Bioelectricity and Biomagnetism, Wave Propagation in Power Systems, Advanced High Voltage Techniques, Fundamentals of Radar Systems I, Economic Operation of Power Systems, Electricity Trading, Fundamentals of Radar Systems II, Statistical Learning and Simulation and Teaching in Higher Education

B.Sc. Degree : (2.9/4) 1996 – 2000

Dept. of Electrical Engineering,
Istanbul Technical University
with course load specialization in power electronics, power systems,
electrical machines and high voltage

Graduation Project: SF6 Gas Circuit Breaker and Comparison of Circuit
Breakers

High School :

Fevziye Mektepleri Vakfı Ayazağa Işık High School 1993 – 1996

Secondary :

Türk Eğitim Derneği Ankara College 1990 – 1993

Foreign Languages :

Advanced English, Basic Level German

PUBLICATIONS

International Conference Papers

- H. F. Carlak, N. G. Gençer, C. Beşikçi, 2010, “Thermal Images of Electrically Stimulated Breast: a simulation study,” International Medicon 2010 12th Mediterreanean Conference
- H. F. Carlak, N. G. Gençer, C. Beşikçi, 2011, “Medical Thermal Imaging of Electrically Stimulated Woman Breast: a simulation study, IEEE Engineering in Medicine and Biology Society Conference (EMBS 11)

National Conference Papers

- H. F. Carlak, N. G. Gençer, 2009, “Elektriksel Olarak Uyarılmış Göğüs Modelinin Termal Görüntüleme Simülasyonları,” 14. Biyomedikal Mühendisliği Ulusal Toplantısı, CD-ROM, İzmir
- H. F. Carlak, N. G. Gençer, C. Beşikçi, 2010, “Akım Uygulamalı Termal Görüntüleme Yöntemi için Üç Boyutlu Meme Modeli ile Benzetimler,” 15. Biyomedikal Mühendisliği Ulusal Toplantısı, CD-ROM, İzmir